Observation of Collective Behavior in High-Multiplicity Proton-Gold Collisions with

PHENIX at RHIC

By

Qiao Xu

Dissertation

Submitted to the Faculty of the

Graduate School of Vanderbilt University

in partial fulfillment of the requirements

for the degree of

DOCTOR OF PHILOSOPHY

in

Physics

March 31, 2018

Nashville, Tennessee

Approved:

Julia Velkovska, Ph.D.

Senta V Greene, Ph.D.

David J Ernst, Ph.D.

Will E Johns, Ph.D.

Keivan Stassun, Ph.D.

To my beloved parents,

Zuoping Xu, and Ailan Ge,

And all my dear friends.

ACKNOWLEDGMENTS

I would like to express my very great appreciation to my advisor, Dr. Julia Velkovska,for her patient guidance, enthusiastic encouragement and useful critiques of this research work. This thesis would not have been possible without her direction.

Advice given by my co-advisor Dr. Vicki Greene has been a great help, Vicki is super nice and expertized. She is always providing professional guidance and valuable support.

Assistance provided by Dr. Shengli Huang was greatly appreciated. He was instructing and helping me really quite a lot when I first came to Brookhaven Lab and turned from CMS to PHENIX. He gave me a lot of useful advice on the data analysis part and physics intuition about the heavy-ion collisions.

I wish to acknowledge the help provided by my colleagues at Vanderbilt University: Dr. Shengquan Tuo, Hong Ni, Weizhuang Peng, Sylvia Morrow, Dr. Sourav Tarafdar. Dr. Shengquan Tuo led me to the analysis part step-by-step, when I was first- and second-year graduate student. Hong Ni and I were in the same lab from undergraduate study and I learned a lot from him. Weizhuang Peng took main charge of the particle identification part of this thesis, while Sylvia is the chair of the paper about the measurement of triangular flow in small systems and she is very talented.

I am particularly grateful for the assistance given by my colleagues at Brookhaven National Lab, Dr. Stefan Bathe, Dr. Takao Sakaguchi, Dr. Axel Drees, Dr. Haiwang Yu, Chen Xu, they not only offered me advice on the research, but also guidance on my career.

Dr. Theo Koblesky provided me with very valuable analysis on the beam geometry and a careful cross-check of some results. Javier Orjuela-Koop produced nice theory plots and we co-chaired the paper about the measurement of elliptic flow in p+Au collisions.

I would like to offer my special thanks to my father Zuoping Xu and my mother Ailan Ge. They give me consistent caring and love. In the summer of 2017 they came to visit me in the U.S. We spent an unforgettable time together.

iii

TABLE OF CONTENTS

LIST OF FIGURES

xv

Chapter 1

INTRODUCTION

The fundamental structure of matter can be described using just a few basic building blocks or fundamental particles: quarks, gluons, leptons, etc., governed by four fundamental forces: the gravitational, electromagnetic, strong, and weak interactions. The theory that describes how these particles interact with each other and all, but the gravitational force, is called the Standard Model of particle physics. It has successfully explained a vast body of experimental results and precisely predicted a broad range of phenomena. The scheme of the Standard Model is shown in Fig. 1.1.

The strong interaction is characterized by the exchange of particles called gluons that act between quarks, antiquarks, and other gluons that all carry color charge. Color charge is analogous to the electromagnetic charge, but it has three types ($\pm$red, $\pm$green, $\pm$blue) rather than one, which results in a different type of force with completely different rules. These rules are detailed in the theory of quantum chromodynamics (QCD), which is the theory of quark-gluon interactions. The physical systems dominated by the strong force, like the heavy ion collision systems studied in this thesis, are described by QCD.

1.1   QCD Phase Diagram and Quark Gluon Plasma

Through many experimental confirmations, QCD is established as the correct theory that describes the strong interaction. The key phenomenon observed in strongly-interacting systems is the quark (color) confinement, i.e., color-charged particles cannot be isolated and directly observed in normal conditions. At large distances, the potential between two color charges grows linearly with distance causing confinement. However, at small distances, which correspond to very high momentum transfer between the color charges, the quarks

Standard Model of Elementary Particles

three generations of matter
(fermions)

	I	II	III		
mass charge spin	≈2.4 MeV/c² 2/3 1/2 **u** up	≈1.275 GeV/c² 2/3 1/2 **c** charm	≈172.44 GeV/c² 2/3 1/2 **t** top	0 0 1 **g** gluon	≈125.09 GeV/c² 0 0 **H** Higgs

QUARKS

≈4.8 MeV/c² -1/3 1/2 **d** down	≈95 MeV/c² -1/3 1/2 **s** strange	≈4.18 GeV/c² -1/3 1/2 **b** bottom	0 0 1 **γ** photon

SCALAR BOSONS

≈0.511 MeV/c² -1 1/2 **e** electron	≈105.67 MeV/c² -1 1/2 **μ** muon	≈1.7768 GeV/c² -1 1/2 **τ** tau	≈91.19 GeV/c² 0 1 **Z** Z boson

LEPTONS

<2.2 eV/c² 0 1/2 **ν_e** electron neutrino	<1.7 MeV/c² 0 1/2 **ν_μ** muon neutrino	<15.5 MeV/c² 0 1/2 **ν_τ** tau neutrino	≈80.39 GeV/c² ±1 1 **W** W boson

GAUGE BOSONS

Figure 1.1: The Standard Model of elementary particles [1].

and gluons would interact very weakly due to "asymptotic freedom" – a phenomenon in which the strong coupling constant decreases logarithmically with the transverse momentum, or the distance scale. This understanding was achieved by David J. Gross, H. David Politzer and Frank Wilczek, who were recognized by the 2004 Nobel Prize in Physics. At high temperature, similar to that which existed in the early Universe, the QCD potential is modified and a state of deconfined quarks and gluons can be formed. In an extensive review [9], Edward Shuryak was the first to examine the high-temperature phase in detail, and also proposed the term "quark-gluon plasma" (QGP) to describe the deconfined state in analogy with the plasma state in atomic physics. Lattice QCD predicts that the QCD phase transition between a hadron gas and QGP occurs above a critical temperature $T_c \approx 170$ MeV [10]. Using this value and the Stefan Boltzmann law, e.g. - ε/T^4 is proportional to the number of degrees of freedom, one can estimate the approximate critical energy density for the phase transition $\varepsilon_c \approx 1$ GeV/fm^3. This value depends on the number of quark flavors considered. The energy density in the QGP phase is about an order magnitude larger than that of normal nuclear matter. The transition temperature is about 100,000 times higher than the temperature in the center of the Sun, but it can be achieved in the laboratory in collisions of heavy ions moving with speeds close to the speed of light.

A schematic presentation of the QCD phase diagram is shown in Fig. 1.2.

1.2 Space-Time Evolution of QGP in Heavy Ion Collisions

In heavy-ion collisions at the Relativistic Heavy Ion Collider (RHIC), the center-of-mass energy per colliding nucleon reaches 200 GeV. At these energies, the nucleons participating in the collision may produce an initial energy density of about 5 GeV/fm^3 [11] and initial temperature in excess of 300 MeV. This energy density is sufficient to form the QGP state as it is well above the critical energy density predicted by lattice QCD.

Fig. 1.3 shows a schematic diagram of the space-time evolution of relativistic heavy-ion collisions, where the "space" corresponds to the extent of the longitudinal source size. We
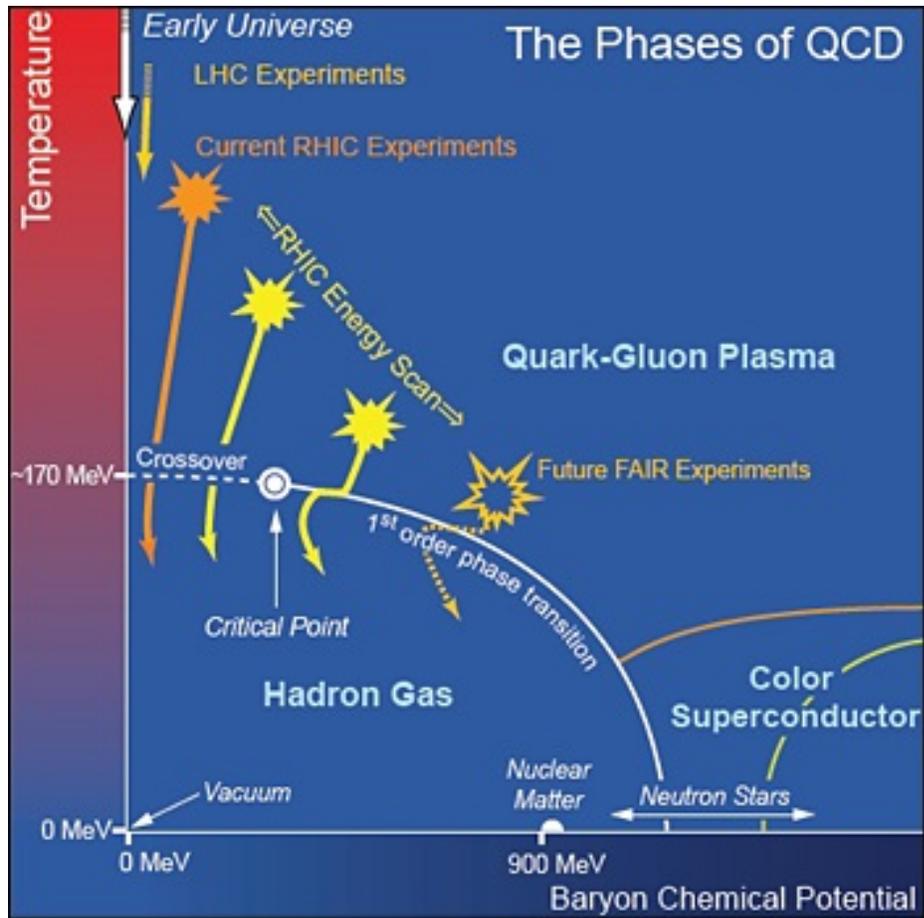
Figure 1.2: Phases of QCD matter [2]
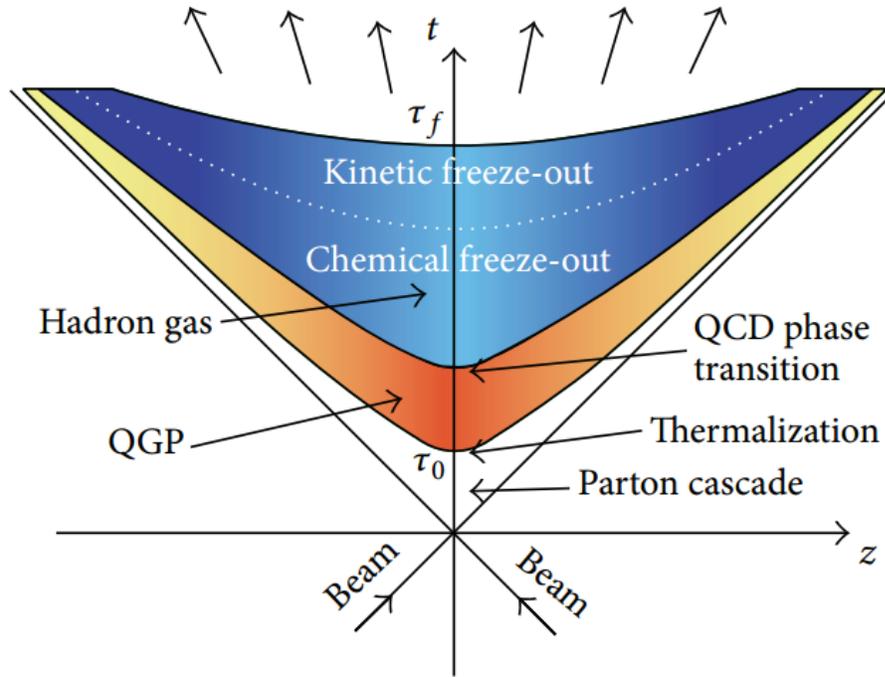
Figure 1.3: The space-time chart of QGP evolution

can distinguish four different stages:

- In the initial stage of collisions, labeled as "parton cascade" in Fig. 1.3, processes of parton-parton hard scatterings may predominantly occur in the overlap region of the two colliding nuclei, depositing a large amount of energy in the medium. The matter is not equilibrated, and perturbative QCD models can describe its dynamics by a cascade of weakly-coupled partons. The pre-equilibrium state lasts about 1 fm/c or less.

- QGP: After the short pre-equilibration time, the QGP phase would be formed in which the partons may reach a thermal equilibrium. The QGP rapidly expands, decreasing its temperature and energy density. This stage of the system evolution is usually described using hydrodynamics. The energy density in the QGP phase is about an order magnitude larger than that of normal nuclear matter.

- Hadron gas: Once the critical temperature is reached, $T_c \sim 170$ MeV, the QGP

hadronizes and turns into a hadronic gas. The hadron gas continues to expand and cool. At some point, the inelastic hadronic interactions cease and the hadron abundances are fixed. The temperature at this point in the evolution is referred to as the chemical freeze-out temperature. The chemical freeze-out may coincide with the phase transition temperature. This stage of the system evolution is typically described using microscopic hadronic cascade models, although it may also be described macroscopically using hydrodynamics.

- Freeze-out: Elastic hadron-hadron interactions continue until the mean free path becomes larger than the size of the system, at which point the hadron interactions cease. The corresponding temperature is called the kinetic freeze-out temperature T_f. After that, the hadrons decouple and freely stream out from the medium, and can be detected in our apparatus.

1.3 Signatures of QGP Formation

1.3.1 QGP in Large-Ion Collisions

Before RHIC turned on it was recognized that there may be no unique signal that will alone lead to the identification of QGP. Instead, a number of different signals that come out from the medium were proposed as QGP signatures such as jet quenching, strangeness enhancement, and J/Ψ suppression [12]. After many years of experimental investigations the collection of signals indicative of QGP has grown to include collective flow and quark-number scaling of the collective flow signals. In fact, the discovery of the near-perfect fluid behavior at RHIC [11, 13, 14, 15] is the main milestone of the relativistic heavy ion program. This dissertation focuses on the collective flow and quark number scaling in small-systems and seeks to understand the limits of this perfect-fluid behavior.

- In large-ion collisions, the produced particles move collectively or flow, and this flow may quantify the effective Equation of State (EoS) of the matter and reveal

the properties of the flowing medium. In central (head-on) Au+Au collisions at the RHIC, a strong radial flow is observed. In non-central collisions, both radial and elliptic flow are observed [16]. Since in non-central collisions the initial nucleus-nucleus overlap region has an elliptic shape, the initial pressure gradient is larger along the impact parameter and the matter moves preferentially in this direction. The experimental measurements of the particle spectra and azimuthal correlations have been described by viscous hydrodynamic calculations that use a QGP EoS based on the Lattice QCD calculations, and require a very small value of the specific viscosity (e.g., shear viscosity over entropy density η/s).

- An empirically discovered feature in the elliptic flow measurements at RHIC is the number of constituent quark (NCQ) scaling. The measurement of the flow strength as a function of the transverse momentum, p_T, for particles with different mass exhibits universal behavior, when scaled by the number of the constituent quarks in the hadron. This behavior is thought to be a manifestation of the partonic degrees of freedom in the system and an indication that the elliptic flow develops early in the system evolution prior to hadronization.

1.3.2 Collectivity in Small Systems ?

The discussion above refers to large collision systems, such as Au+Au or Pb+Pb. Small collision systems, such as p+A, d+Au, or p+p were thought to be too small to provide volume and number of particles sufficient for a QGP to form and equilibrate. These systems were, therefore, considered to be control experiments to measure background effects of cold nuclei, which may obscure the true signal of the QGP; p+p collisions were used as a baseline to assess the hadronic physics. However, recent results [17, 18, 19, 20, 21, 22, 4, 5] have shown that small collision systems may show collective effects similar to those that we typically associated with QGP formation. The physics mechanism creating these collective effects is under heated discussion and is the main topic of the analysis in this thesis. A

summary of the recent studies of collectivity in small systems is presented below:

1.3.2.1 The "Ridge" is Everywhere

"Ridge" is a term describing a pattern of the two-dimensional two-particle correlations functions in heavy-ion collisions. These correlation functions, C, are typically measured as a function of the azimuthal angle ϕ and pseudo-rapidity η differences $\Delta\phi$ and $\Delta\eta$, of the paired particles as shown in the top part of Fig. 1.4. The long-range rapidity correlations are rather strongly peaked near $\Delta\phi = 0$ (near-side), leading to the resemblance to a mountain ridge. The short-range peak structure in the near-side ($\Delta\eta \approx 0$) is a consequence of locally-correlated jets of particles originating from the hadronization of hard-scattered partons resulting in a bunch of particles emitted in a narrow cone. The long-range ridge in A+A collisions at RHIC and the LHC (Large Hadron Collider) was understood to be a consequence of the collective flow of the produced medium [23]. The ridge structure reflects the anisotropy of the interaction region – the almond-shaped region where the two nuclei overlap with each other for non-central collisions. This anisotropy entails a pressure gradient in the initial conditions: the pressure is larger along the minor axis of the ellipse, accordingly, more particles will be emitted in the direction of the largest gradient. This ultimately generates an anisotropy in the azimuthal distribution of the produced particles. This anisotropy is typically quantified by the strength of the Fourier component of the final-state particle azimuthal distributions, with the second harmonic (elliptic flow) denoted as v_2, and the third harmonic (triangular flow) - as v_3. These are the two strongest Fourier components that will be discussed extensively in this thesis.

It was considered that the ridge feature can only be observed in A+A collisions. However, at the LHC and later at RHIC [17, 18, 19, 20, 21, 22, 4, 5], the ridge was also found in smaller systems like p+Pb, d+Au and ^{3}He+Au, even in p+p collisions [24]. Fig. 1.4 shows the ridge observed in high-multiplicity p+Pb collisions at the LHC [19] and ^{3}He+Au [5] at RHIC, in contrast to the back-to-back correlation seen in the minimum bias p+p collisions,
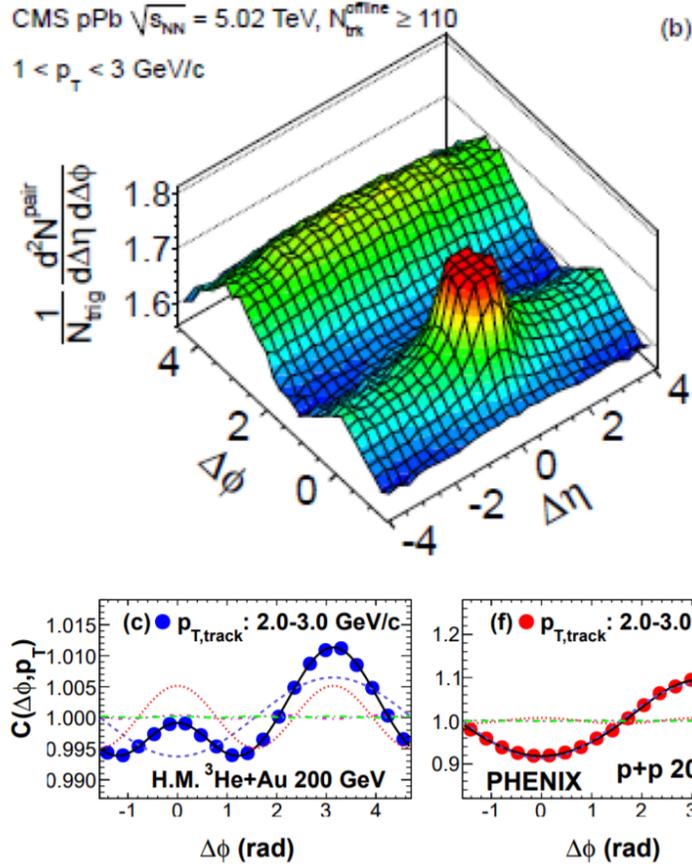
Figure 1.4: (Top) Long-range near-side ridge in p+Pb collisions at the LHC. (Bottom left) Long-range near-side ridge observed in ^{3}He+Au collisions at RHIC. (Bottom right) No ridge is seen in minimum bias p+p collisions.

where we think that no QGP is formed. The observation of the ridge in many different systems led people to consider that small systems are quite interesting to study, since they challenge our understanding of the conditions necessary to produce QGP and the limits of the collective behavior.

1.3.2.2 Multi-Particle Correlations in Small Systems at the LHC

To understand if the ridge is truly a consequence of collective flow in both large and small systems, it is important to establish that the collective behavior is seen in the system as a whole, and not just in the correlations of few particles. This is best done by measurements
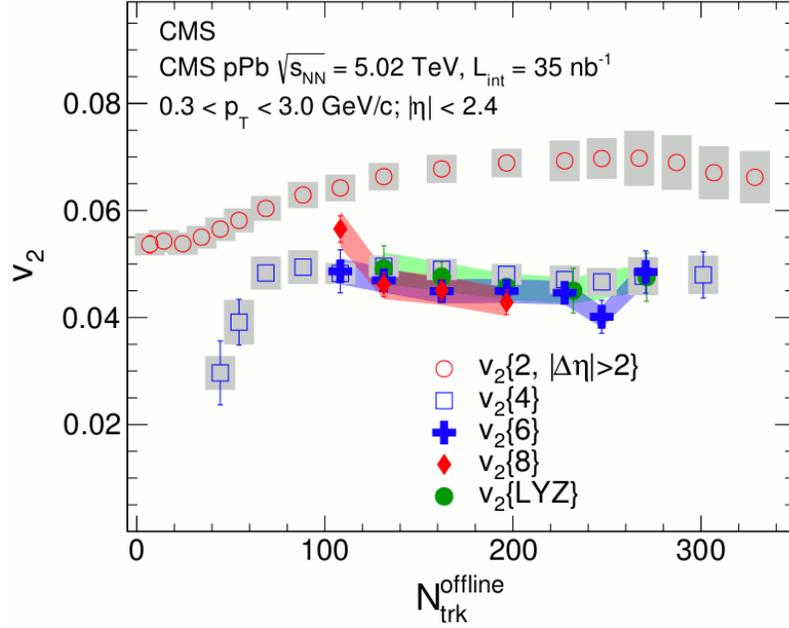
Figure 1.5: Multi-particle correlation in *p*+Pb and PbPb systems in LHC [3].

of multi-particle correlations. The CMS experiment at the LHC measured the strength of the elliptic flow using 2-, 4-, 6-, 8- , or all-particle correlations [3]. The result is shown in Fig. 1.5 as a function of the multiplicity of the collisions. We see that the 2-particle correlations show a stronger signal, but the correlations of 4-, 6-, 8- and all-particles are all significant and have the same magnitude. This result is a strong evidence of collectivity in the *p*+Pb system at 2.76 TeV [3].

1.3.2.3   Anisotropic Flow Measurements in High-Multiplicity *d*+Au and ³He+Au Collisions at RHIC

RHIC has published anisotropic flow results in high-multiplicity *d*+Au and ³He+Au collisions [4, 5]; indications of a strong collective behavior were found in both systems. More interestingly, a sizable triangular anisotropic flow appears in ³He+Au collisions. A hydrodynamics model, which involves the development of QGP, describes the data quite well. These findings greatly challenge the original idea that QGP cannot be formed in these smaller-volume systems. Fig. 1.6 shows the second order flow (v_2) as a function of

10

transverse momentum in high-multiplicity d+Au and ^{3}He+Au, as well as the measurement of the third-order flow v_3 in ^{3}He+Au collisions.

1.3.2.4   Azimuthal Correlations of Identified Particles in Small Systems at the LHC and RHIC

Until now, we discussed the measurements using inclusive charged particles (mostly hadrons), as they are easier to measure. Adding information about the particle type provides important additional insights to assess the origin of collectivity, the nature of the medium, and how it evolves in heavy-ion collisions. At RHIC and LHC, recent progress of the measurements of identified particle flow includes pions, (anti-)protons, and kaons, etc. Fig. 1.7 shows that the identified particle flow v_2 measured in d+Au collisions by the PHENIX experiment at RHIC [25], and in p+Pb collisions by the ALICE experiment at LHC [6] depends on the particle mass. The observed "mass-splitting" pattern, e.g., the heavier particles are pushed to higher transverse momentum, as expected if the particles are moving in a common velocity field, is very similar to the observations in larger systems and another strong piece of evidence of a hydrodynamic origin for collectivity in the smaller systems.

1.4   Motivation and Goals for This Thesis

The motivation of this thesis is to understand how final-state particle correlations develop in heavy-ion collisions, both large and small. Although all the observations seem to support the idea of QGP formation in small systems, there are other explanations proposed that do not involve final-state interaction or QGP at all. Instead, the final-state particle correlations arise because of initial-state momentum domains, or some other mechanisms that are not correlated with the initial system geometry. The geometry scan at RHIC provided an excellent handle to study the effect of the initial-state geometry, i.e. p+Au $->$ d+Au $->$ ^{3}He+Au collisions. Figure 1.8 illustrates the energy density distribution in the initial

11
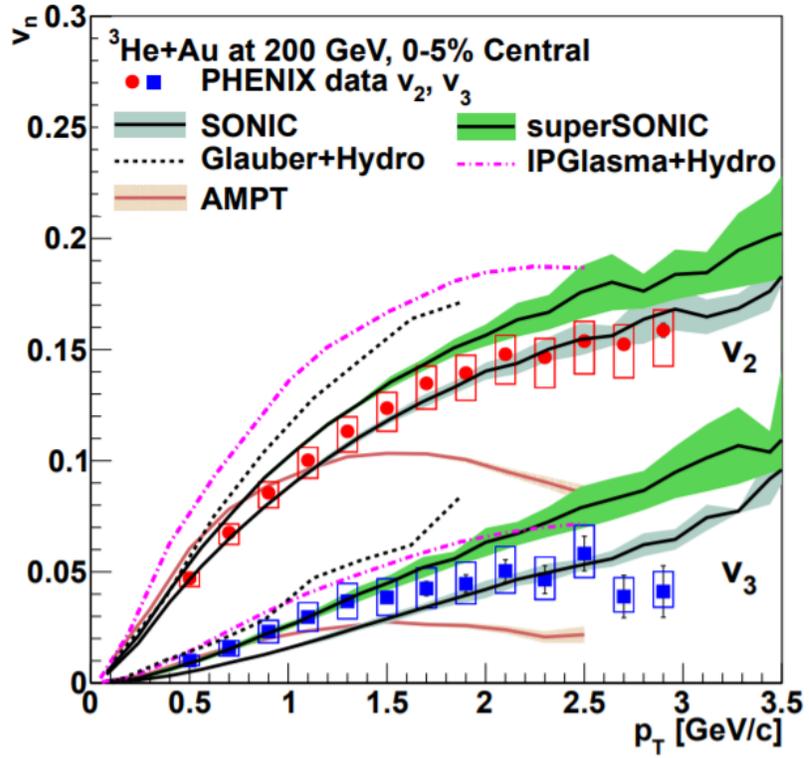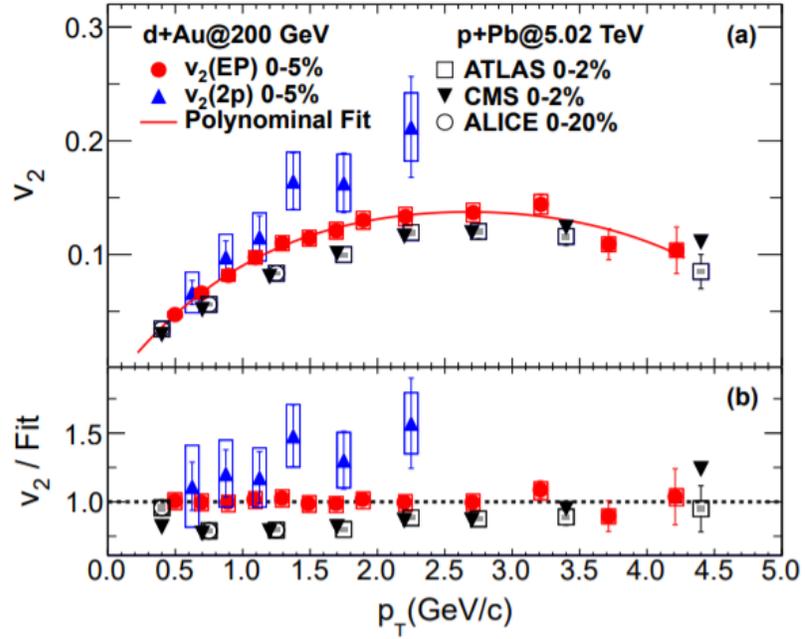
Figure 1.6: Second-order collective flow (v_2) as a function of transverse momentum in high-multiplicity d+Au and ^{3}He+Au collisions[4, 5], and third-order flow (v_3) in ^{3}He+Au collisions.
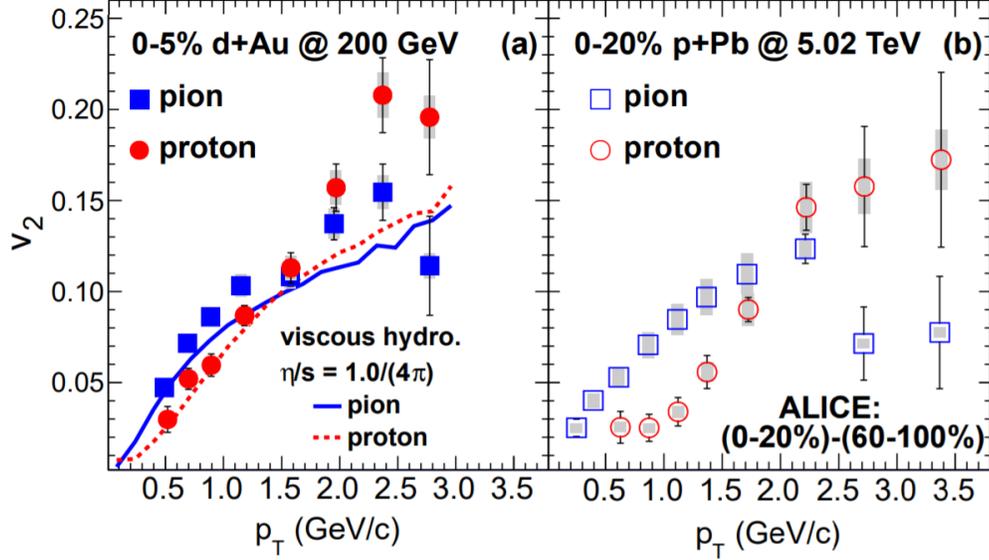
Figure 1.7: Identified $\pi^{\pm}$, (anti-)proton elliptic flow in d+Au at RHIC [4] and p+Pb at LHC [6].

condition of these three small systems and the resulting evolution within the hydrodynamics framework. The color scale indicates the local energy density profile and the arrows are proportional to the velocity of the fluid cell from which it originates. It appears that the initial one/two/three hot spots would lead to circular, elliptical and triangular anisotropy during the evolution. Although it is not clear if hydrodynamics would be valid in this regime, this model gives a definite prediction of what the final-state particle distributions would look like. Our geometry-controlled experiments performed at RHIC aim to find out what the role of the initial geometry is for developing collectivity and final-state momentum anisotropy [26].

Some explanations have QGP in the picture, while others do not; some place the origin of the collectivity entirely in the initial state prior to the collision (Color-Glass-Condensate model) and are not related to the initial geometry of the overlap zone, while others (like hydrodynamics or parton transport models) rely on final-state interactions for the translation of the initial geometry into final-state momentum anisotropy. In this thesis we formulate and test two hypotheses to discriminate the models.
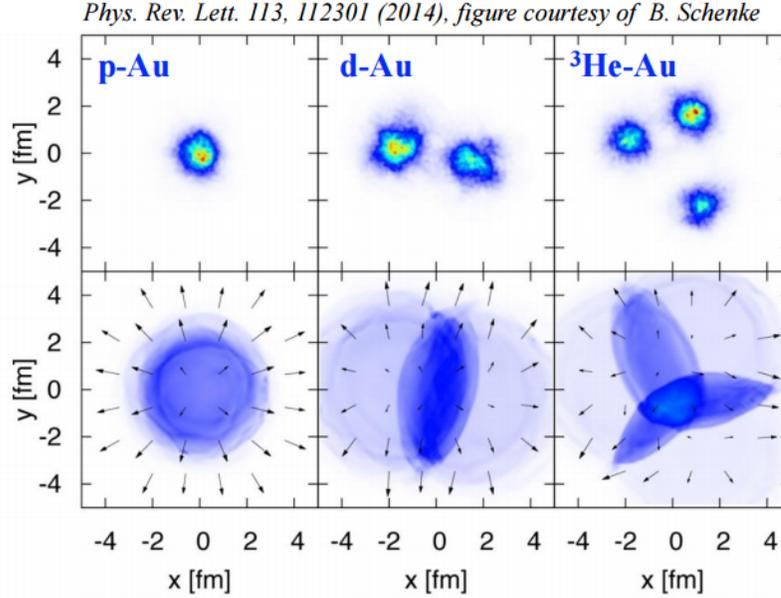
Figure 1.8: Calculations of the initial energy density (top) in p/d/^{3}He+Au collisions at RHIC, and (bottom) the resulting hydrodynamic evolution [7].

– Hypothesis 1: The collective flow of the particles is directly related to the initial geometry. To test this hypothesis, the projectile is changed from the previously measured deuteron and helium to proton, to see how the elliptic and triangular flow changes in the final state. We are able to perform this geometry engineering at the smallest scale owing to the versatility of RHIC.

– Hypothesis 2: The collective flow of identified particles has a mass effects, as expected in the hydrodynamics description in Section 2.2. To test this hypothesis, we measure the elliptic flow of identified protons (anti-protons) and pions, since they have different masses, and a different number of constituent quarks (three or two, respectively).

14

Chapter 2

COLLECTIVE BEHAVIOR IN HEAVY ION COLLISIONS AND THEORETICAL

MODELING

In this chapter, we discuss the physics models in heavy-ion collisions.

2.1   Initial State Models

The initial state model describes the position distribution of the energy density. It is the input to the hydrodynamic modeling of the system evolution. The most commonly used initial-state models are outlined below.

2.1.1   Glauber Model

The Glauber model was developed to address the problem of high-energy scattering with composite particles. It has been used extensively to model geometric quantities in relativistic heavy ion collisions (see [27] for a detailed review). The Monte Carlo (MC) Glauber formulation locates nucleons at specific spatial positions that can vary randomly from one collision to another. Some experimental data is needed to serve as model inputs. The two most important inputs are the nuclear charge densities and the energy dependence of the inelastic nucleon-nucleon cross section. Once these are known, the MC-Glauber calculation of geometric quantities is quite easy. To do that, first, the positions of each nucleon in a nucleus is determined according to the measured charge density distribution of the nucleus extracted from low-energy electron scattering experiments [27]. For spherical nuclei, such as Pb, the distribution is taken to be uniform in azimuthal and polar angles,

and described by a two-parameter Fermi function:

$$\rho(r) = \rho_0(1 + exp(\frac{r-R}{a}))^{-1}$$

Here, ρ_0 is the nucleon density in the center of the nucleus, R is the nuclear radius, and a is the so-called skin depth. The collision impact parameter (b) is determined from $dN/db \propto b$, and the centers of the nuclei are shifted to (-b/2, 0, 0) and (b/2, 0, 0). The nucleons move along a straight line along the beam axis initially. The nuclear reaction is then modeled by successive independent interactions between two nucleons from different nuclei. The interaction strength between two nucleons is parameterized by the nucleon-nucleon inelastic cross section (σ_{NN}). Two nucleons from different nuclei are supposed to collide if their relative transverse distance is less than $D = \sqrt{\sigma_{NN}/\pi}$. A nucleus-nucleus collision is accepted if at least one such nucleon-nucleon collision was obtained. An important initial condition quantity in simulating collectivity flow is the eccentricity ε of the event. MC-Glauber simply calculates the moments of the participant nucleon for each event. In each event one can evaluate the variances σ_x^2 and σ_y^2 along x and y axis, and the covariance

$$\sigma_{xy} = \langle xy \rangle - \langle x \rangle \langle y \rangle$$

of the participant distributions projected on the x and y axes. The variances are event-by-event variable, and $\langle \cdot \rangle$ is the average over events. Then the ε_2 is calculated through Eq. 2.1.

$$\varepsilon_2 = \frac{\sqrt{(\sigma_x^2 - \sigma_y^2)^2 + 4\sigma_{xy}^2}}{\sigma_x^2 - \sigma_y^2} \tag{2.1}$$

Table. 2.1 shows the geometric characterization of small system collisions at $\sqrt{s_{NN}} = 200$ GeV in the 0%-5% centrality class.

Table 2.1: Geometric characterization of small system collisions at $\sqrt{s_{NN}} = 200$ GeV in the 0%-5% centrality class, using Monte Carlo Glauber with nucleon coordinates smeared by a two-dimensional Gaussian of width $\sigma = 0.4$ fm.

	p+Au	d+Au	^{3}He+Au
Glauber $\langle \varepsilon_2 \rangle$	0.23 ± 0.01	0.54 ± 0.04	0.50 ± 0.02
Glauber $\langle \varepsilon_3 \rangle$	0.16 ± 0.01	0.19 ± 0.02	0.28 ± 0.02

2.1.2 Color Glass Condensate Model

The Color Glass Condensate (CGC) is a QCD-based effective theory developed in order to describe quantitatively the gluon saturation regime in a high-energy strongly-interacting system. In the CGC model, the system is analogous to actual glasses, with a classical Yang-Mills description of initial glasma fields [28]. A glass is a disordered system, which evolves very slowly relative to natural time scales: it is like a solid on short time scales and like a liquid on much longer time scales. Similarly, the partons of interest are disordered and evolve in longitudinal momentum in a manner analogous to a glass. Condensate means it contains a very high density of massless gluons. The gluon density saturates at a certain order, called a multiparticle Bose condensate state. The glasma model includes multiple types of quantum fluctuations, including fluctuations of color charges within the nucleons [29]. The combination of the initial glasma field and the Impact-Parameter dependent Saturation (IP-Sat) Model [30] is called the IP-Glasma model. This model can also explain the azimuthal anisotropy in large-ion collisions, if is combined with hydrodynamic evolution.

Unlike the Glauber model described earlier, CGC has a totally different mechanism of producing initial state fluctuations. The eccentricity from the CGC model is based on color fields and the initial energy distribution is smooth, while in the MC-Glauber model all the harmonics are developed by the position fluctuations of single nucleons. The position of the nucleons are different from one nucleus-nucleus collision to another, so the initial energy distributions are discrete. As a result they end up with different eccentricity, especially for

System	p+Au	^{3}He+Au	d+Au
ε_2	0.10$\pm$0.02	0.59$\pm$ 0.01	0.55$\pm$0.01

Table 2.2: The ε_2 calculated by IP-Glasma model, all from 0-5% top events. The nucleons have a perfect round shape.

the third order harmonics.

From IP-Glasma calculation, the ε_2 from round proton assumption are listed in Table. 2.2. However, there is another variant of the IP-Glasma model where they treat the proton as having constituent quarks. This only matters in the p+Au case. The eccentricity obtained in p+Au in this case is $< \varepsilon_2 >= 0.46 \pm 0.01$.

2.2 Hydrodynamics Model

Because it is extremely hot and short lived, QGP cannot be observed and measured directly. However, we can detect its existence and determine its properties taking advantage of the collective nature of the medium. To model the space-time evolution of QGP, several viscous hydrodynamics models are proposed (see Ref.[31] for a recent review). The fluid elements then hadronize and interact with each other (hadron cascade and re-scattering) to reach the final state.

2.2.1 Collective Behavior

The observation of collectivity in matter can be a powerful indicator of fundamental properties of that matter. Collectivity means many discrete structures are interacting together to form a whole otherwise known as highly correlated behavior. In high energy heavy ion physics, a common interpretation of this behavior, although not the only interpretation, is of a locally equilibrated medium with bulk properties instead of a group of individually weakly interacting constituent particles. In this case, the medium is a QGP and the bulk properties are that of a hydrodynamically described fluid: viscosity, density,
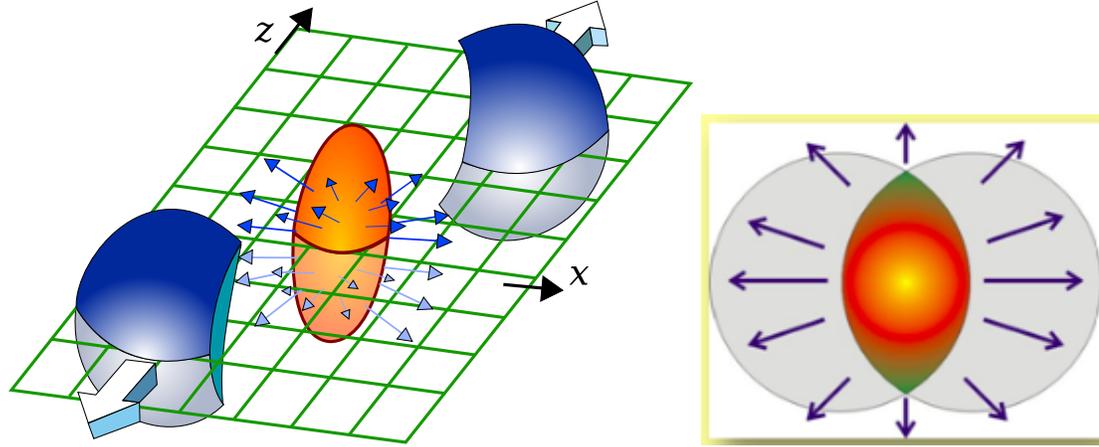
Figure 2.1: (Left) A cartoon showing the reaction plane orientation in a nucleus-nucleus collision. (Right) The initial anisotropy transferred to final momentum anisotropy

temperature, etc [32].

2.2.2 Observables for Collectivity

Consider the collision of two heavy nuclei as depicted in Fig. 2.1.

The overlap region between the two nuclei forms an almond shaped region oriented to the plane of the initial collision geometry. After the collision, the two nuclei remnants (the blue shapes) no longer participate and the yellow overlap region forms the QGP medium and starts to expand. This energy density distribution gives rise to a larger pressure gradient in the shorter direction. The larger the pressure gradient, the more momentum the particles will gain once the medium finishes evolving. This variation in the momentum of the final-state particles produces effects in the azimuthal (relative to the collision axis) distribution of particles. Therefore, by measuring the azimuthal anisotropy of the final-state particles, long-range angular correlations can be observed. The initial-state collision geometry being transformed into final-state momentum anisotropy indicates collective behavior of the matter produced in the collisions.

In order to quantify the azimuthal anisotropy, the final state particle distribution is de-

composed into a Fourier series:

$$\frac{dN}{d\phi} = N_0(1 + \sum_{n=1}^{\infty} 2v_n \cos n(\phi - \Psi_n))$$

where N is number of final state particles in a certain azimuthal ϕ angle, N_0 is a normalization constant and Ψ_n denotes the orientation of the event plane. The event plane is determined using the final-state particles and is an approximation of the reaction plane, which is spanned by the impact parameter (b) and the z-axis of the collisions. The Fourier coefficients v_n defined from the formula are proportional to the degree of anisotropy for each harmonic order n. In addition to measuring the v_n for various systems, a relativistic hydrodynamic calculation can be compared to the data. The very good agreement with hydrodynamic calculations curves suggests a medium which flows.

In practice, not all azimuthal correlations in the data are of collective origin. Additional 'non-flow' correlations arise from resonance decays, jet fragmentation, and Bose-Einstein correlations [33]. They can be suppressed by appropriate kinematic cuts or by using multi-particle correlations known as higher-order cumulants: $v_n\{4\}$ and $v_n\{6\}$ denote the anisotropic flow coefficients obtained from the fourth and sixth order cumulants, respectively.

2.2.3 Hydrodynamics

Hydrodynamics is an effective macroscopic description of a system that is in approximate local thermal equilibrium. It can be derived from the underlying microscopic (kinetic) description through an expansion in gradients of the local thermodynamic variables. If the transverse size of the nucleus is large compared to the interaction length scales involved, hydrodynamics is the appropriate theoretical framework to calculate the response of the medium to the geometry.

The hydrodynamics model relies on only one assumption: the system remains close to

local thermodynamic equilibrium throughout its evolution. This hypothesis is quite strong, yet simple and powerful. All the information of the system is contained in its thermodynamic and transport properties, i.e., its equation of state and transport coefficients. Calculations based on ideal hydrodynamics do a fair to reasonable job in reproducing the observed elliptic flow [34]. Nevertheless, the hydrodynamic interpretation requires that the relevant mean free paths and relaxation times be small compared to the nuclear sizes and expansion rates. Recently, application of viscous hydrodynamics to high-energy heavy-ion collisions has evoked widespread interest ever since a surprisingly small value of η/s was estimated from the analysis of the elliptic flow data [35]. It is also notable that due to quantum effects, there is a strong coupling limit of the shear viscosity to entropy density ratio $\eta/s = \frac{1}{4\pi}$.

2.2.4 SONIC and SUPERSONIC Model

SONIC is short for Super hybrid mOdel simulatioN for relativistic heavy-Ion Collisions [36]. It is a hybrid model for heavy ion collisions, combining viscous hydrodynamics and late-stage hadronic rescatterings. SUPERSONIC is an event-by-event generalization of the SONIC model, including pre-equilibrium flow. The comparison of SONIC and SUPERSONIC could provide an experimental handle on pre-equilibrium QCD dynamics [37].

2.2.5 iEBE-VISHNU Model

iEBE-VISHNU is another viscous hydrodynamics plus hadronic cascade, full (3+1)D, which means it simulates the behaviors of 3D geometry and 1D time evolution of the quark gluon plasma. After the system hadronizes, the hydrodynamic fluid is converted to particles that undergo hadronic rescattering, which is implemented using iURQMD 3.4 [38, 39]. While most of the flow is developed at the early stages of the collisions, hadronic rescattering plays a modest but important role in the system development and particle species dependence of v_2 [40].

2.3   Event Generators

Let us introduce some event generators (interaction models). These models do not rely on hydrodynamics assumptions and the partons interact with different kinetics models.

2.3.1   HIJING

It is expected that hard or semihard parton scatterings with transverse momentum of a few GeV are expected to dominate high energy heavy ion collisions. HIJING (Heavy Ion Jet INteraction Generator) Monte Carlo model was developed with special emphasis on the role of minijets (copious production of semihard partons) in $p + p$, p+A, and A+A reactions at collider energies [41]. The model includes multiple mini-jet productions, nuclear shadowing of the parton distribution functions, and a mechanism of jet interactions in dense matter called jet quenching. Glauber geometry for multiple collisions is used to calculate the interactions in p+A and A+A collisions. There is no collective flow in the HIJING model, but local correlations like mini-jets exist. We use it to study the underlying non-flow correlations in p+Au collisions.

2.3.2   AMPT Model

AMPT is short for "A Multi-Phase Transport Model" [42]. It uses the Heavy Ion Jet Interaction Generator (HIJING) for generating the initial conditions based on the Glauber model, Zhang's Parton Cascade (ZPC) for modeling partonic scatterings, the Lund string fragmentation model or a quark coalescence model for hadronization, and A Relativistic Transport (ART) model for treating hadronic scatterings [43, 44]. The combination of these models is used to provide a coherent description of the dynamics of relativistic heavy ion collisions.

Chapter 3

RHIC AND THE PHENIX EXPERIMENT

3.1 The Relativistic Heavy Ion Collider

The RHIC accelerator is located at Brookhaven National Laboratory (BNL). It was designed to study nuclear matter via relativistic collisions of light and heavy ions, and protons. As depicted in Fig. 3.1, the beams are generated and accelerated in one of the Tandem Van de Graaff accelerators, then proceed to the Booster synchrotron, and the Alternating Gradient Synchrotron (AGS) before entering the two rings of RHIC (called "blue" and "yellow"). The beams then cross and collide at four interaction points, where the RHIC detectors are installed. RHIC has a circumference of 3833.8 m, consisting of a total of 1,740 superconducting magnets, two separate rings and can collide practically any two separate species. At a magnetic field of 3.458 T, the beam energy is 100 GeV/n for fully stripped gold ions, and 250 GeV for (polarized) protons [45].

Four detectors: PHENIX, STAR, BRAHMS, and PHOBOS started operation in year 2000. PHOBOS and BRAHMS completed their experimental program in 2005. PHENIX collected data until 2016 and is now decommissioned to make room for a new state-of-the-art detector called sPHENIX.

Since the beginning of operations in year 2000, RHIC has collided many different species and at different center-of-mass energies. Figure 3.2 summarizes the colliding beams and the average store luminosity for Run1 through Run17 of RHIC, where a Run period is typically several months in the early part of each year. This thesis uses data from p+Au collisions at $\sqrt{s_{NN}} = 200$ GeV from Run15 of RHIC.
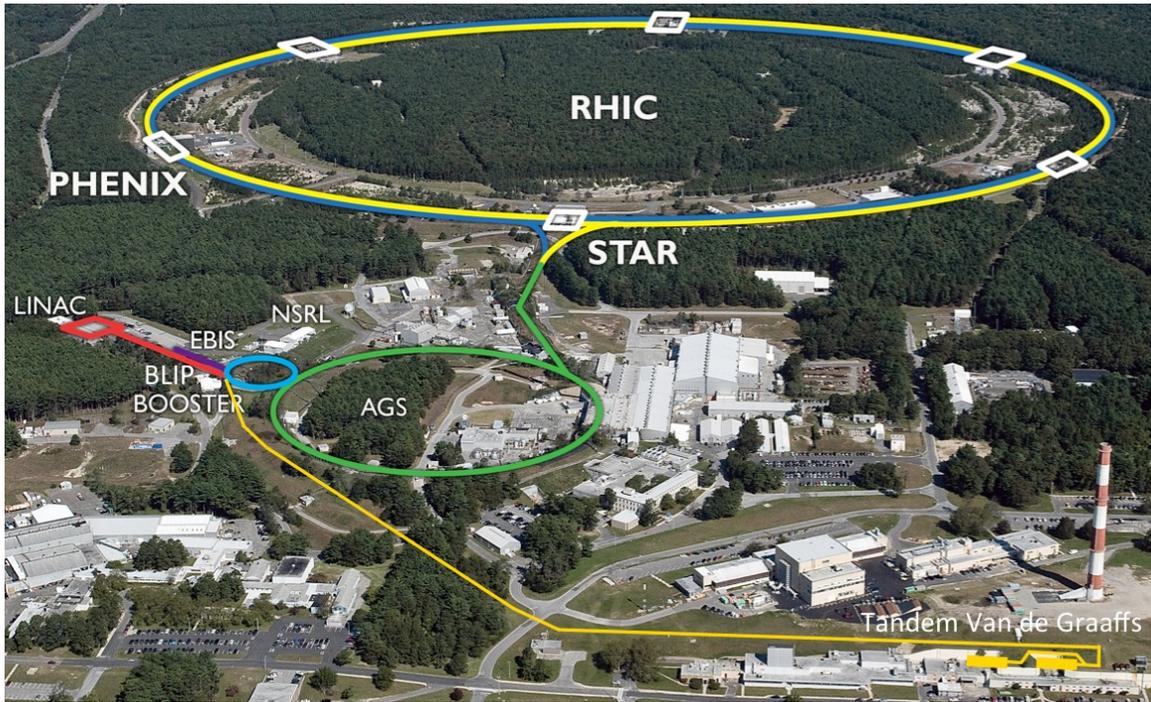
Figure 3.1: RHIC accelerator complex.
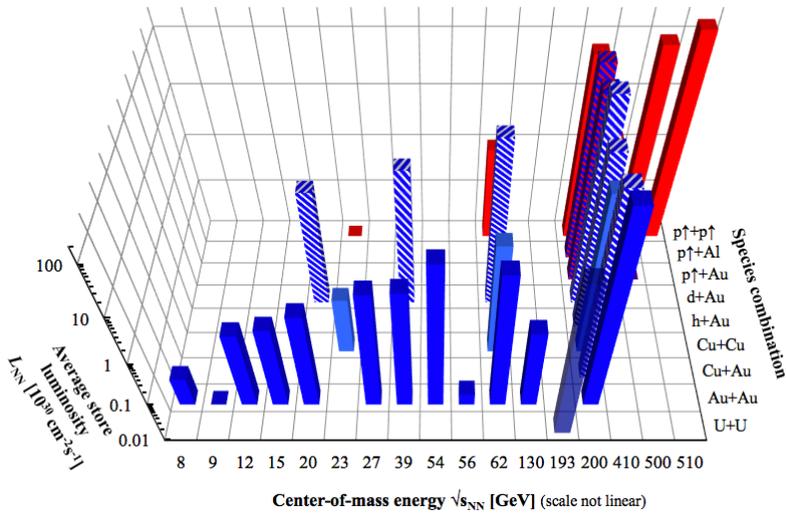
Figure 3.2: Summary of RHIC collision species, center-of-mass energy per nucleon and the average store luminosity [8]

3.2   PHENIX

PHENIX, the Pioneering High Energy Nuclear Interaction eXperiment, is an experiment at the Relativistic Heavy Ion Collider that took data for 16 years (2000–2016). The PHENIX collaboration was formed in 1991. Members of the collaboration designed, built, and operated the PHENIX detector. They are still actively analyzing the collected data and publishing the physics results. PHENIX was built with the primary goal to discover and study a new state of matter called the Quark-Gluon Plasma. The QGP discovery was announced in 2005 [11], while the studies of the QGP properties still continue. This chapter briefly introduces various parts of the detectors systems that were used in the analysis presented in this thesis, including central tracking, particle identification, and forward detectors [46].
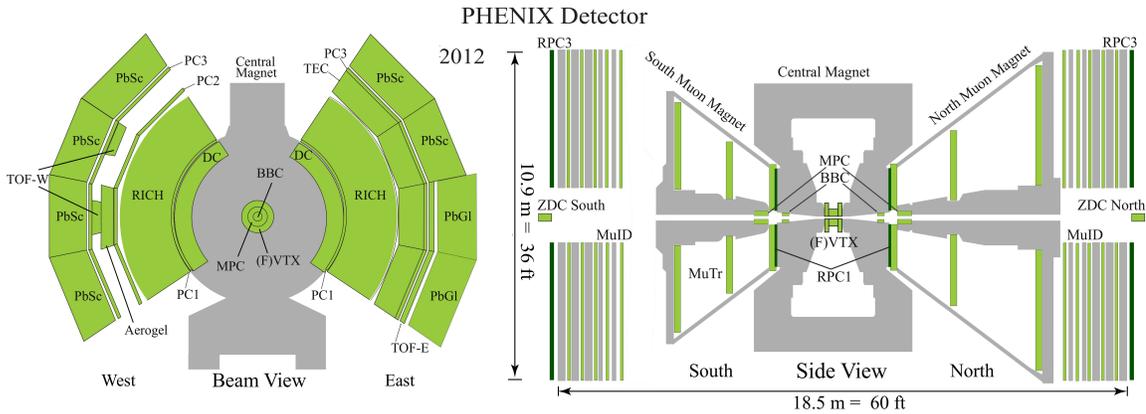
Figure 3.3: PHENIX detector configuration

3.2.1   Magnet Systems

PHENIX has three major magnet sub-systems. The Central Magnet, Muon Magnet North and Muon Magnet South [47]. The Central Magnet is an axial field magnet energized by two pairs of concentric coils, which can be run separately, together, or in opposition. The Central Magnet is 9 meters tall and weighs nearly 500 tons. It covers a pseudorapidity interval of $\pm$ 0.35 units. The $\int B.dl = 0.78$ Tesla-meters at 90 degrees. Muon Magnet
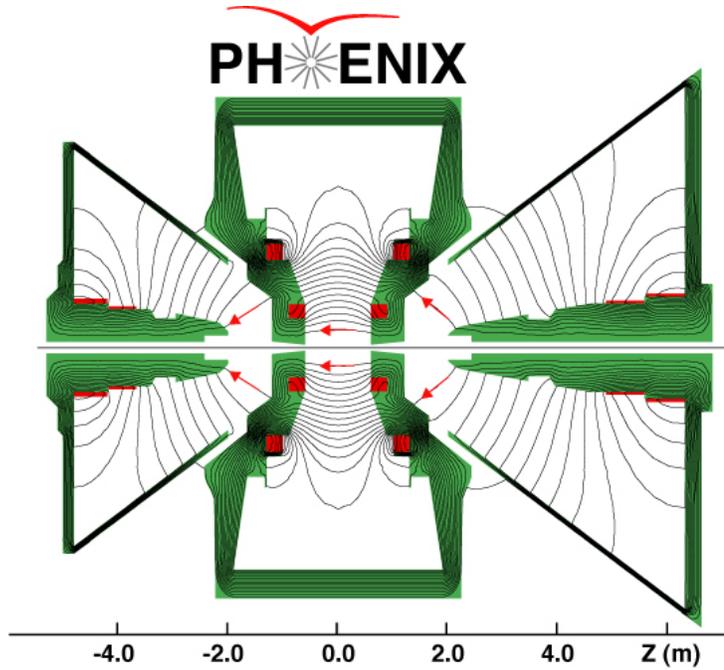
Magnetic field lines for the two Central Magnet coils in combined (++) mode

Figure 3.4: PHENIX magnet system

South uses two solenoidal coils to produce a radial magnetic field. The $\int B.dl$ along a line at 15 degrees from the beam axis is 0.75 Tesla-meters.

3.3 Tracking and Particle Identification Systems

3.3.1 Drift Chamber

The multi-layer focusing Drift Chamber (DC) is a part of the both arms (East and West) of the PHENIX central-arm spectrometer. It is placed between 2.02 m and 2.46 m in radial distance from the interaction point and occupies 180 cm in the z direction and two 90 degree sectors in the azimuthal angle ϕ. DC is able to provide high resolution transverse momentum, p_T, measurements [48] for charged particles produced in the collisions.

3.3.2   Pad Chambers

Pad Chambers (PCs) measure the position of charged particles with at the radial distances of 2.49 m, 4.19 m, and 4.89 m with high precision. PCs have three layer, numbered PC1 to PC3. They provide tracking in the area outside of the magnetic field of the central magnet and are extremely important in rejecting mis-reconstructed tracks and background particles that do not originate in the collision [48].

3.3.3   Time of Flight

PHENIX is designed to detect and identify individual particles such as pions, protons, kaons, and deuterons. The primary particle identification technique for these types of particles is called the time-of-flight method [49].

The time-of-flight measures the velocity of the particles by measuring the time the particle travels from the collision point to the detector, then combines with the length of the path, and the momentum measured from drift chamber to determine the mass the specific particle.

PHENIX has two separate time-of-flight detectors, TOF-East, and TOF-West. They cover different azimuthal range as shown in Fig.3.3. TOF-E is consists of a number of "Slats" (plastic scintillator). There are total of 960 slats, and each slat is read-out from both ends using photo-multiplier tubes (PMTs). The TOF-W uses Multi-Gap Resistive Plate (MRPC) technology, it is comprised of 128 MRPC that are readout by 512 coper strips [50]. A more detailed discussion of TOF-W can be found in [50, 51].

An example of particle identification using the time-of-flight technique in the TOF-East detector is shown in Fig. 3.5. In the histogram, there is one entry for each particle recorded. It shows the particle's charge divided by momentum (q/p) as a function of the time-of-flight as measured by the PHENIX experiment at RHIC. The flight distance is about 5 meters. Bands corresponding to each charged particle type (protons, antiprotons, kaons, pions,
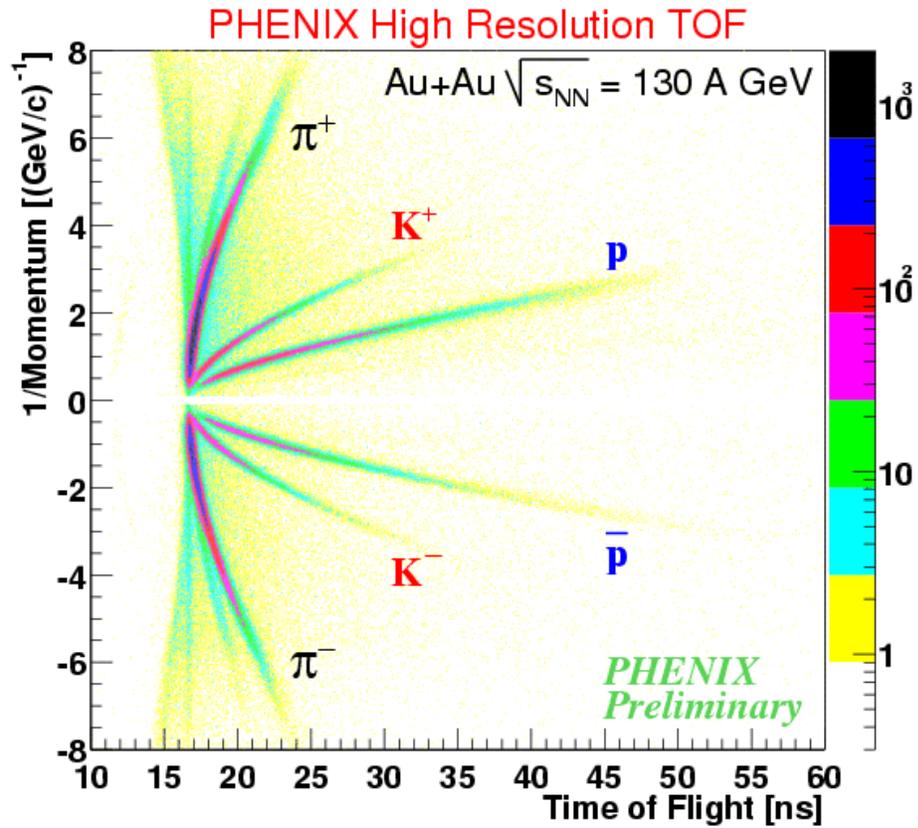
Figure 3.5: Time-of-flight particle identification plot from the PHENIX experiment.

muons) are clearly visible. The positively charged particles are on the top half of the figure while the negatively charged particles are on the bottom half. Labeled are bands of pions (π), kaons (K), and protons (p).

3.4   Forward Detectors

3.4.1   Beam-Beam Counter

The Beam-Beam Counters (BBCs) have 64 elements each in the North and South arm, (forward and backward rapidity, respectively). Each element consists of quartz Cherenkov radiator and meshed dynode PMT. The PHENIX Beam-Beam Counters serve several purposes: 1)Minimum Bias Trigger, 2)Centrality Determination, 3)Time Zero start timing for

the time-of-flight measurement, 4)Collision Vertex determination, which is used as the initial point of charged particle tracking.

3.4.2 Forward Vertex Tracker

The Forward Vertex Tracker(FVTX) can track precisely charged particles at forward and backward pseudorapidity. The FVTX is composed of two annular end caps, each with four stations of silicon mini-strip sensors, covering a pseudorapidity range of $1.2 < |\eta| < 2.2$ that closely matches the two existing PHENIX muon arms. Each station consists of 48 individual silicon sensors, each of which contains two columns of mini-strips with 75 μm pitch in the radial direction, and lengths in the ϕ direction varying from 3.4 mm at the inner radius to 11.5 mm at the outer radius [52]. In this analysis the FVTX is used to determine the orientation of the event planes (or symmetry planes) in the collisions based on the event-by-event azimuthal distribution of the charged particles detected in the FVTX.

Chapter 4

ANALYSIS DETAILS

In this chapter, we discuss the analysis details. We use data from p+Au collisions at a nucleon-nucleon center-of-mass energy of $\sqrt{s} = 200 GeV$ collected by the PHENIX detector during Run 15 at RHIC, which took place in 2015.

4.1   Event Selection

4.1.1   Trigger Selection

To efficiently store events which we are interested, PHENIX has an on-line trigger system when taking data. The Minimum Bias trigger (MB trigger) is used to ensure an event happening is due to an inelastic collision and with minimum possible detector bias. It is defined as a coincidence in the same event between the BBC detectors in the Au-going and proton-going directions, requiring at least one photomultiplier tube (PMT) firing in each direction; in this way about 84±4% of the total inelastic p+Au cross section is captured. The High Multiplicity trigger (HM trigger) is based on the MB trigger, but imposes the additional requirement of more than 35 photomultiplier tubes firing in the BBC-S. Events that satisfy this trigger condition correspond roughly to the 5% most central event class, the definition of event class could be seen in section 4.1.3. The adoption of HM trigger allows us to increase our central event sample size by a factor of 25, as seen in left hand side of Fig. 4.1. The BBC south charge distribution categorizes the centrality percentile class as shown in right top of Fig. 4.1. Right bottom side of Fig. 4.1 illustrates that the trigger efficiency is around 100% for central events. Number of events taken and used:

p+Au minbias: 838.5M

p+Au centrality trigger: 1423.3M
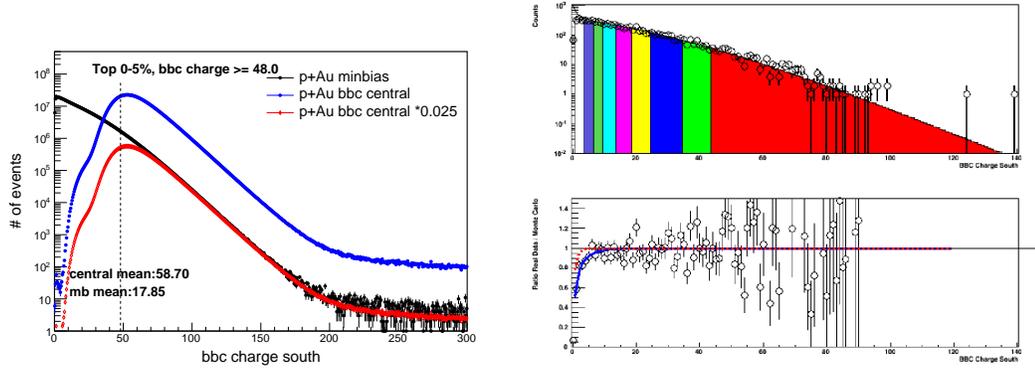
Figure 4.1: BBC charge in Au going direction in centrality-triggered samples compared with minimum bias triggered samples. Left panel: BBC charge distribution recorded in real data in the different trigger paths. Right panel: Centrality percentiles in the BBCS charge distribution, and trigger efficiency for a Negative Binomial Distribution (NBD) model.

4.1.2 Run-by-Run Quality Plots and Selection

The data are recorded in segments called "run". Some runs are not well-calibrated or not well-performed. For each run, we can plot the number of detected charged particles, often referred to as "tracks", and total charge in the BBCS, which is proportional to the multiplicity of the produced particles, and reject runs which are off the average by three standard deviations σ. The run-by-run profile histograms, on which these selections are based, are shown in Fig.4.2.
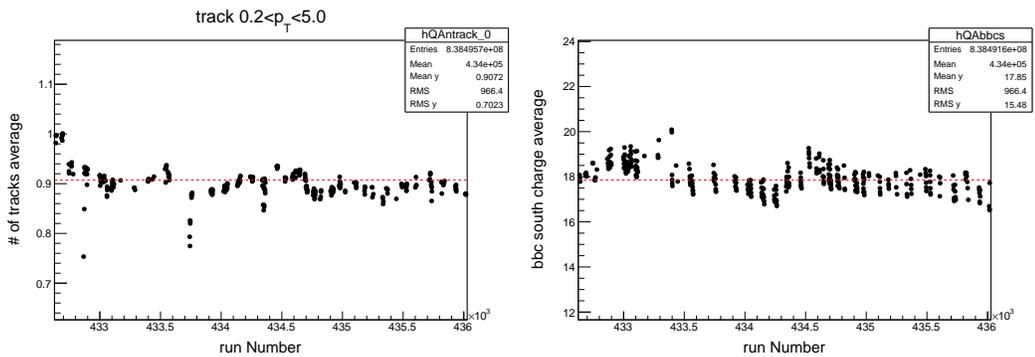
Figure 4.2: Run-by-Run quality assurance plot in p+Au collisions based on the average number of total tracks in each run (Left), and using the average bbc-south charge in each run (Right).

4.1.3 Centrality Classes Selection

Heavy ions are extended objects, and the system created in a head-on collision is different from that in a peripheral collision. We, therefore, categorize nuclear collisions by their centrality, parametrized by the impact parameter b which is, however, not a direct observable. Experimentally, the collision centrality can be inferred from the number of produced hadrons, if one assumes that this multiplicity is a monotonic function of b. Knowing which fraction of the total hadronic cross section is observed in the experiment, one can divide the measured distribution of produced particles in centrally classes corresponding to the percentile of total hadronic cross section [53]. The event centrality is determined from the charge sum deposited in BBCs (Beam-Beam Counter south). The BBC charge sum monotonically decreases as the collision centrality decreases. In the right hand side of Fig. 4.1, the distribution is divided into centrality classes by the solid lines from a fixed point [54].

Anisotropic flow is not measured in a single event but in a centrality class. Therefore, event-by-event fluctuations due to impact parameter fluctuations within a centrality class will add to the initial-state fluctuations (and are further discussed in the following subsection) to determine the spectrum of final-state flow (v_n and Ψ_n) fluctuations.

4.1.4 Pile-Up Event Rejection

Multiple collisions per bunch crossing (i.e., event pile-up) are observed to occur at an average rate of 8% in the 0%-5% central p+Au collisions. To reject those pile-up events, typically one can attempt to find and reject the events with more than one reconstructed primary vertex. In the PHENIX current standard p+Au reconstruction procedure, only one vertex is stored for each event (mainly due to CPU time constraint), so this method is not directly applicable and requires modification of the vertex reconstruction. Alternatively, using the hit time information recorded by each PMT of the beam-beam counter, we can distinguish if one event is likely or unlikely to be a pile-up event.

The BBC is capable of recording the time that it takes for a particle to travel from the vertex to the detector. In one particular high-multiplicity event, if this event is a normal event, the time distribution it records should be peaked around some mean value, the width of the distribution should be relatively small. While in a multiple-collision event, there is a very small chance that the different collisions that occur within the same bunch crossing share a similar time within the resolution of the BBC detector. Therefore, the time distribution it records should have more than one peak. Fig. 4.3 shows two example events each showing the non pile-up situation and pile-up situation. To qualify a cut to eliminate the
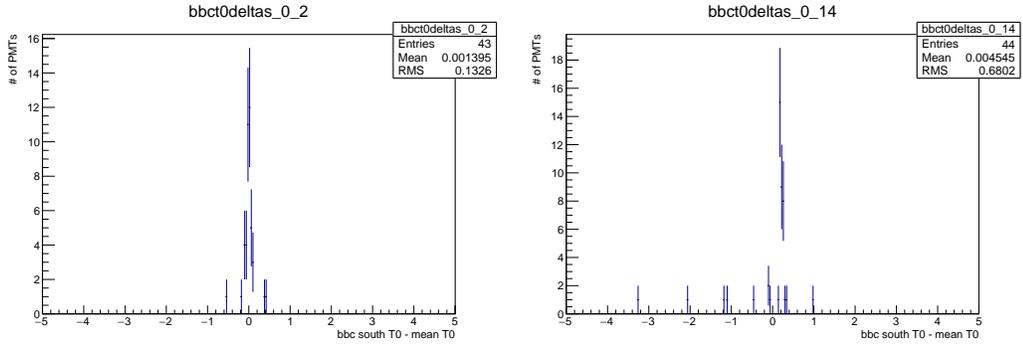
Figure 4.3: Distribution of hit time in BBC south of two example events from real data. Left: a typical non pile-up event. Right: a typical pile-up event.

pile-up events, we propose a pile-up cut based on this time distribution, defined fraction f as: $f = \frac{\#of\,PMTs\;which\;is\;within\;the\;mean\;time\pm0.5(ns)}{Total\#of\;PMTs\;fired}$

We use f > 0.9 as the cut value. If f is large, which means that the times measured by the BBC PMTs are clustered together, this is likely to be a normal event.

To verify this method is valid or not, we use a data-driven approach. We first mix two random minimum bias events to form a single event which is a simulation of a real pile-up event. Then we test how our cut behaves on the normal minimum bias event and the mixed event. The result shows that the cut proposed: f > 0.9 removes 8.5% of total minimum bias p+Au events and 100% of mixed events. The estimation is that 8% events in 0-5% p+Au events are pile-up events, so the purity (means the percentage of non-pile-up events) is 92% before the cut, and almost 100% after the cut.

4.2   Track Selection

4.2.1   PC3 Track Matching

Some central arm tracks are mis-reconstructed by the DC or do not come from the collision itself. To reduce these "fake" tracks, we match the ϕ angle and z-direction of the DC tracks projected to the plane of the third layer PC and the hit position in PC3. The width of these residual distributions are determined in the minimum bias sample and then applied in all trigger samples. We define $d\phi = \phi_{track\ projection\ on\ PC3} - \phi_{hits\ on\ PC3}$ and $dz = z_{track\ projection\ on\ PC3} - z_{hits\ on\ PC3}$ and fit these distributions to determine their standard deviations.

We did the track matching in different transverse momentum bins and separately for particles detected in the East arm or West arm, as well as for positive and negative particles. The dϕ and dz distributions are fitted with a double-Gaussian function. Then, the parameters are smoothed as a function of p_T. Fig. 4.4 shows in $1.0 < p_T < 1.1$ (GeV/c) the matching fit to the dϕ distribution in both West arm, East arm , and positively and negatively charged particles. Fig. 4.5 shows in $1.0 < p_T < 1.1$ (GeV/c) the matching fit to the dz distribution in both West arm, East arm, and positively and negatively charged particles.

Then we fit the signal Gaussian mean and sigma by polynomial functions. See Fig. 4.6 and Fig. 4.7.

Once the mean and sigma are calculated by the smooth fitting, we only keep the particles/tracks within a 2σ range of the mean.

4.2.2   Time-of-Flight Track Matching

As with PC3 matching, we also need to do matching for TOF detectors to get rid of the mis-reconstructed tracks. We also separate the data into 6 vertex bins. The double Gaussian results of TOF matching for the second vertex bin are shown in Figure 4.8, 4.9. And the smooth results of mean and sigma are shown in Fig. 4.10,4.11, 4.12 and 4.13. Tracks
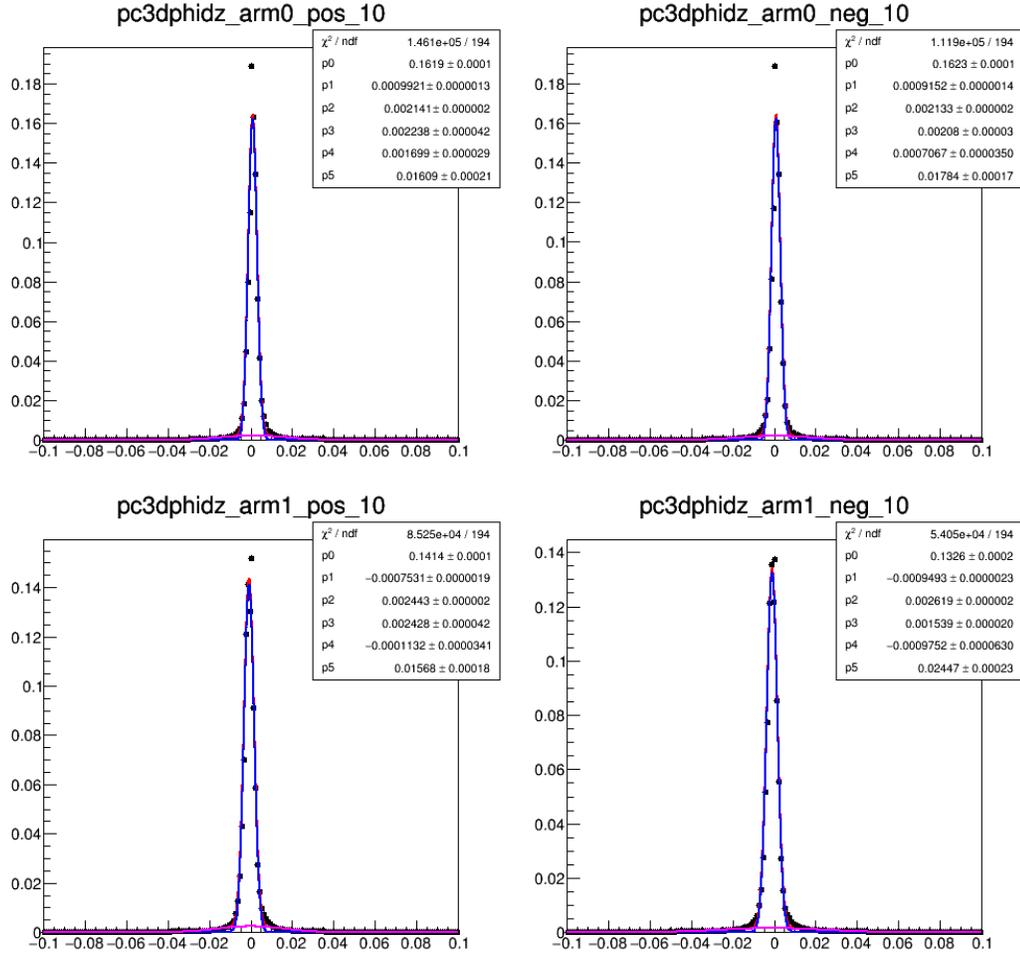
Figure 4.4: PC3 matching dϕ fit in range $1.0 < p_T < 1.1$ (GeV/c) as an example. The red line is the fit for the double Gaussian function, the blue line is the signal Gaussian function according to the fit, and the pink line is the background Gaussian function.
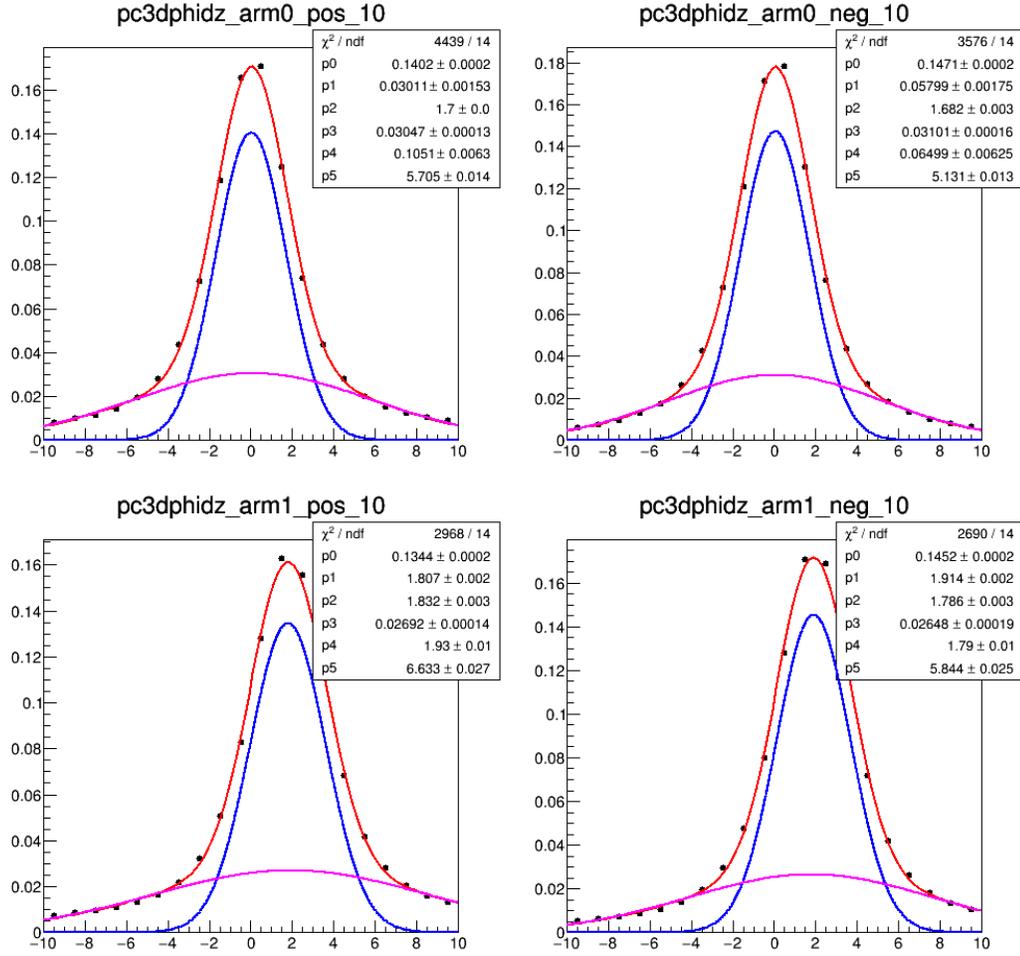
Figure 4.5: PC3 matching dz fit in range $1.0 < p_T < 1.1$ (GeV/c) as an example. The red line is the fit for the double Gaussian function, the blue line is the signal Gaussian function according to the fit, and the pink line is the background Gaussian function.
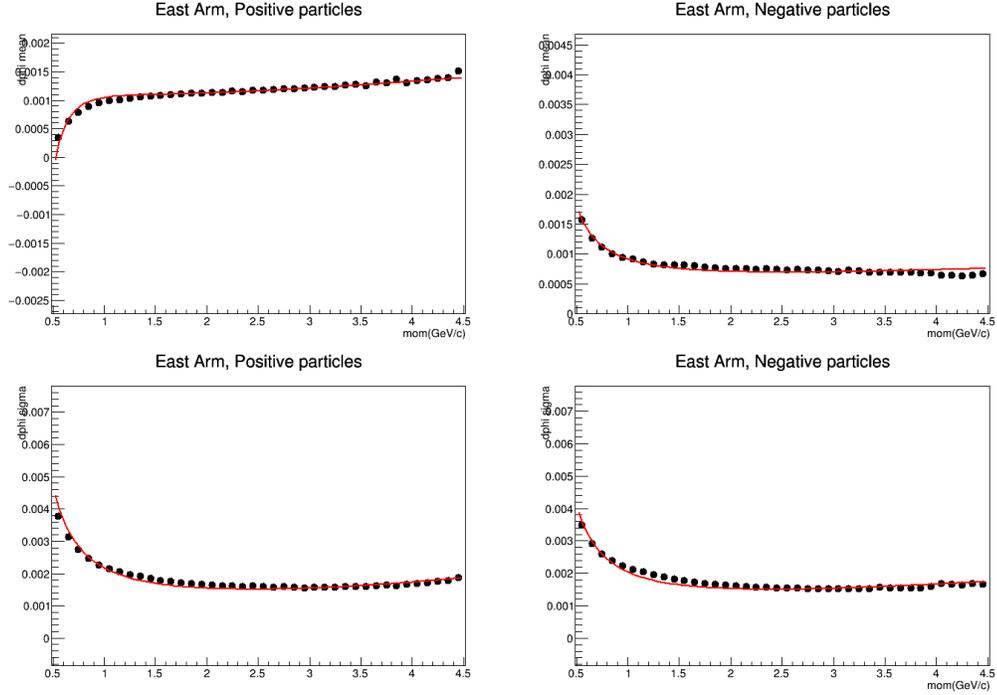
Figure 4.6: The PC3 dϕ matching distribution in the East arm as a function of p_T and the smoothing functions for the Gaussian mean and σ.
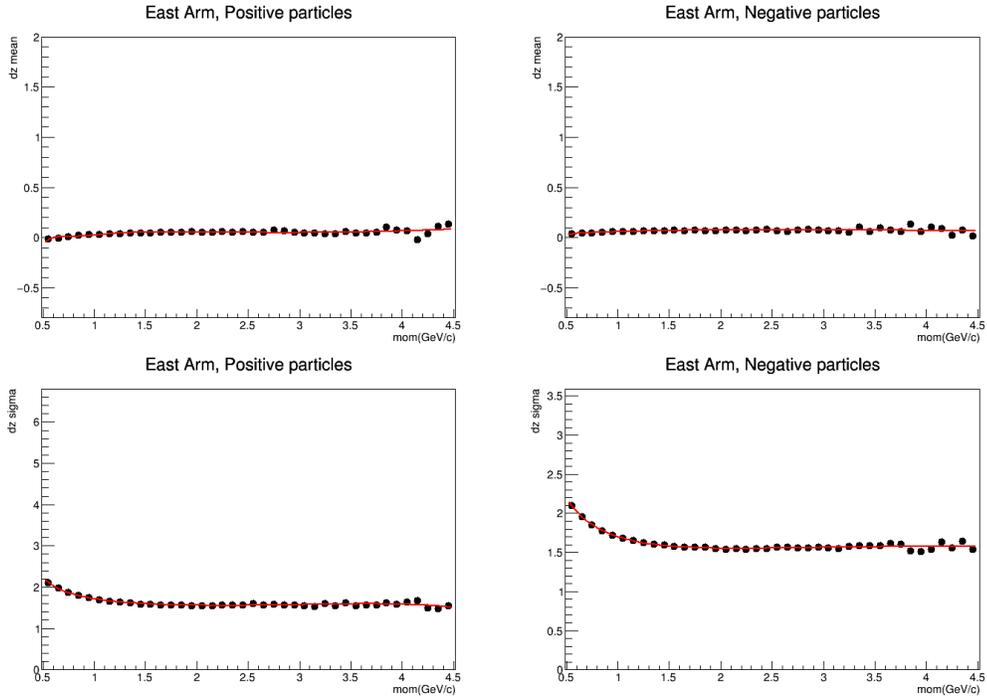
Figure 4.7: The PC3 dz matching distribution in the East arm as a function of p_T and the smoothing functions for the Gaussian mean and σ.

out of 2 σ are cut off for analysis. We only use this selection when we analyze identified particles with the TOF detector.
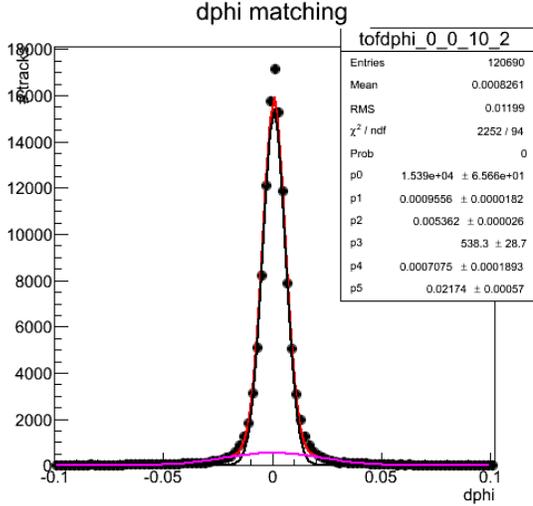
Figure 4.8: TOF matching dϕ fit in the range $1.0 < p_T < 1.1$ (GeV/c) as a example. The red line is the fit for the double Gaussian function, the blue line is the signal Gaussian function according to the fit and the pink line is the background Gaussian function.
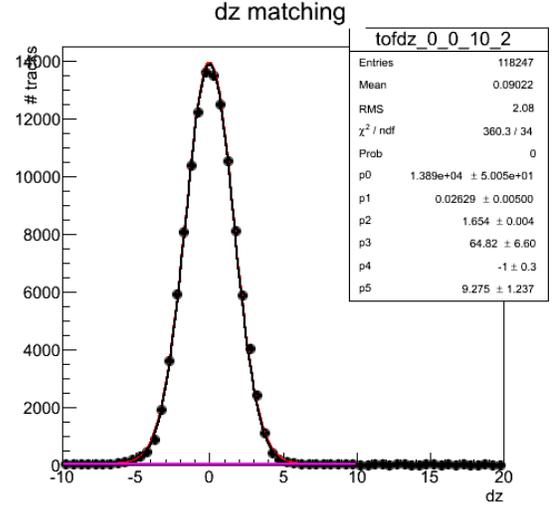
Figure 4.9: TOF matching dz fit in the range $1.0 < p_T < 1.1$ (GeV/c) as a example. The red line is the fit for the double Gaussian function, the blue line is the signal Gaussian function according to the fit and the pink line is the background Gaussian function.

4.3 Detector Calibration

4.3.1 Event Plane Calibration

In the ideal case, the event plane is totally randomly formed in each event and the distribution of the event plane angle is expected to be a flat function. In the real-world, the distribution sometimes has a shape because of the acceptance and non-uniformity of the detector, thus we need to do corrections based on the raw distribution of the event plane angle Ψ distribution.

Here we flattened the event plane Ψ angle on a run-by-run basis. In each run we make sure that the Ψ distribution is flat by fitting with a constant and observe the goodness of fit. The distribution of the second order event plane after recalibration for the $\Psi_{2,CNT}$,

dphimean_east_pos_-5 to 0

Fit function: $a + \dfrac{c}{x} + \dfrac{d}{\sqrt{x}}$

dphisigma_east_pos_-5 to 0

Fit function: $a + \dfrac{g}{\sqrt{x}} + \dfrac{h}{x^2}$
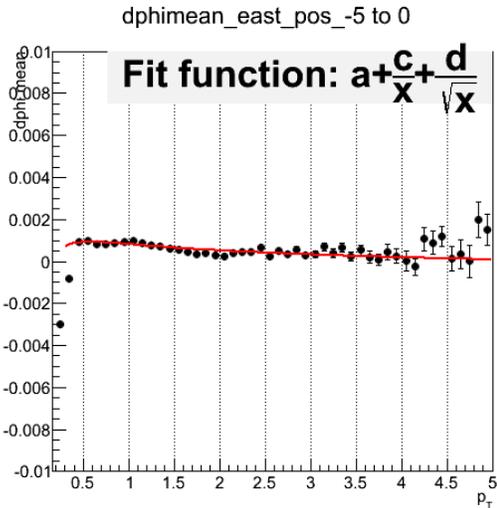
Figure 4.10: TOF matching $d\phi$ vs p_T in the East arm and the smoothing function for the mean value of the Gaussian fit of the $d\phi$ distribution.
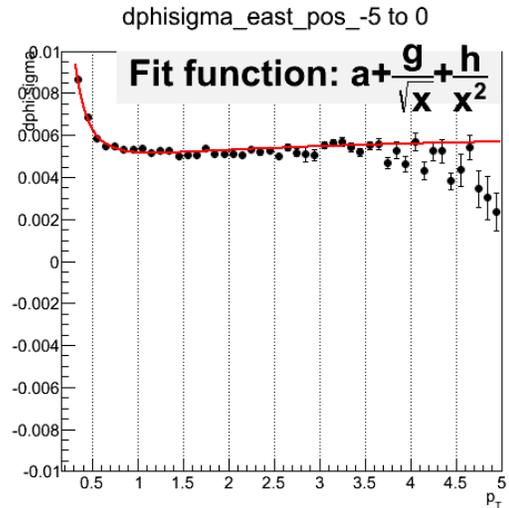
Figure 4.11: TOF matching $d\phi$ vs p_T in the East arm and the smoothing function for the standard deviation σ of the Gaussian fit of the $d\phi$ distribution.

dzmean_east_pos_-5 to 0

Fit function: $a + \dfrac{c}{x} + \dfrac{d}{\sqrt{x}}$

dzsigma_east_pos_-5 to 0

Fit function: $a + \dfrac{g}{\sqrt{x}} + \dfrac{h}{x^2}$
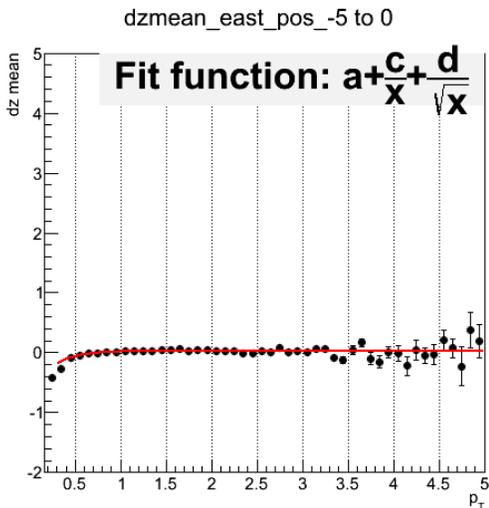
Figure 4.12: TOF matching dz vs p_T in the East arm and the smoothing function for the mean value of the Gaussian fit of the dz distribution.
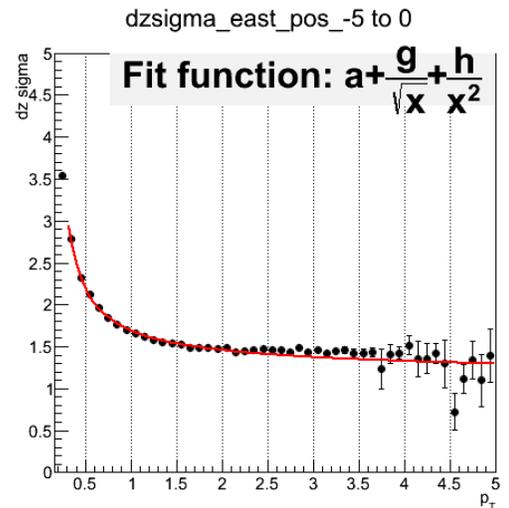
Figure 4.13: TOF matching dz vs p_T in the East arm and the smoothing function for the standard deviation σ of the Gaussian fit of the dz distribution.

$\Psi_{2,BBC_{south}}$ and $\Psi_{2,FVTX_s}$ are shown in Fig. 4.14. Similarly, the distributions of the third order event plane before and after recalibration are shown in Fig. 4.16. The goodness of fit for BBCs and FVTXs are plotted in Fig. 4.15 and 4.17 vs. run number. If χ^2/degrees of freedom is less than 3, then we judge that the event plane has been flattened well for this run.
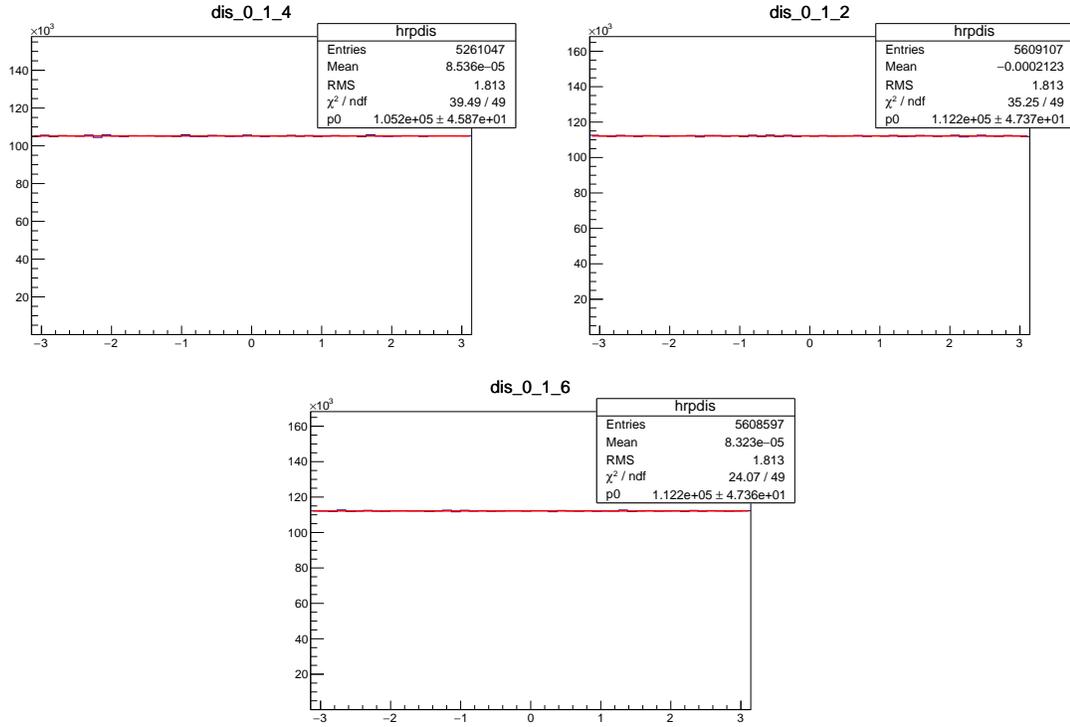
Figure 4.14: The second order event plane distributions for the three subsystems such as CNT, BBCs, FVTX0s in 0-5% central trigger p+Au collisions for the Run 432873.

4.3.2 Beam Geometry and Corresponding Corrections

There was an east-west difference observed in the measurement of v_2 when using mid-rapidity particles in the west arm (-1 < ϕ < 1) and in the east arm (2 < ϕ < 4). The ultimate explanation for this effect comes from beam geometry and residual detector mis-alignments.

First of all, the collision vertex is significantly offset from the z-axis to which all of the
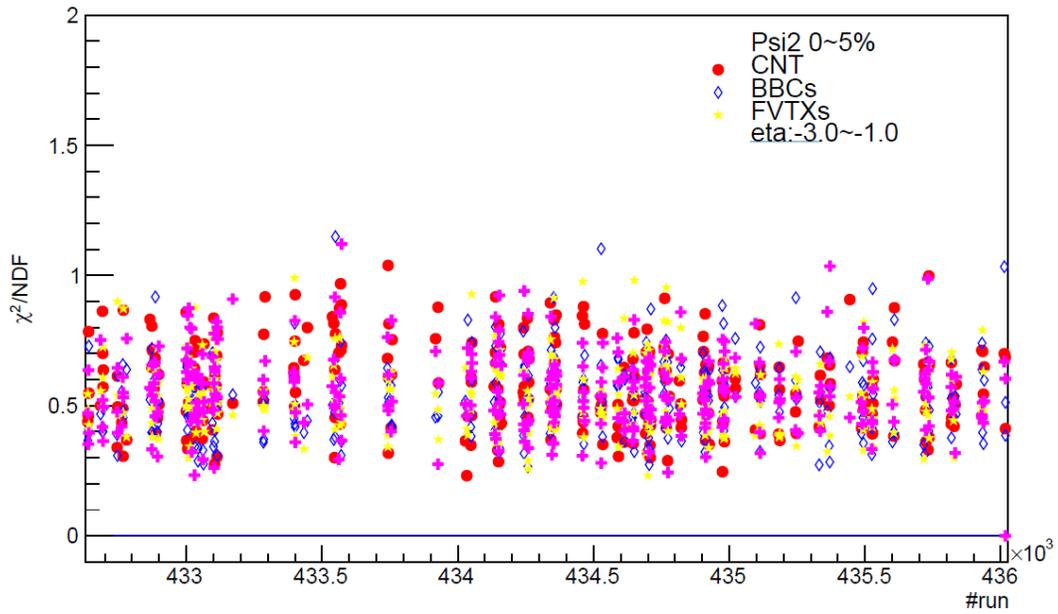
Figure 4.15: The χ^2/ndf from constant fitting of each run for the Ψ_2 of the BBCs, FVTXs, and CNT event plane vs run number.

PHENIX detectors are aligned. The other beam geometry effect, and the more significant of the two effects, comes from the fact that the beams are colliding at an angle of 3.6 mrad in the x-z plane. The reason a non-ideal beam geometry creates an east west v_2 measurement difference is because of the assumption that the event plane angle is azimuthally isotropic during the event plane flattening calibration. In the translated and rotated frame where the beams align with the z-axis the event plane distribution would be uniform, but in the lab frame the event plane distribution in ϕ would have regions of enhancement and reduction.

To correct for the collision vertex offset effect, PHENIX detector elements must have their position calculated with respect to the collision vertex rather than the origin. To correct for the beam rotation effect, PHENIX detector elements must be rotated into the beam frame where the beam is aligned with the z-axis. However, the detector elements being in the right place in the beam frame will not completely correct the event plane bias.

To correct for this issue, we apply a weight factor on hits in ϕ regions. The weight
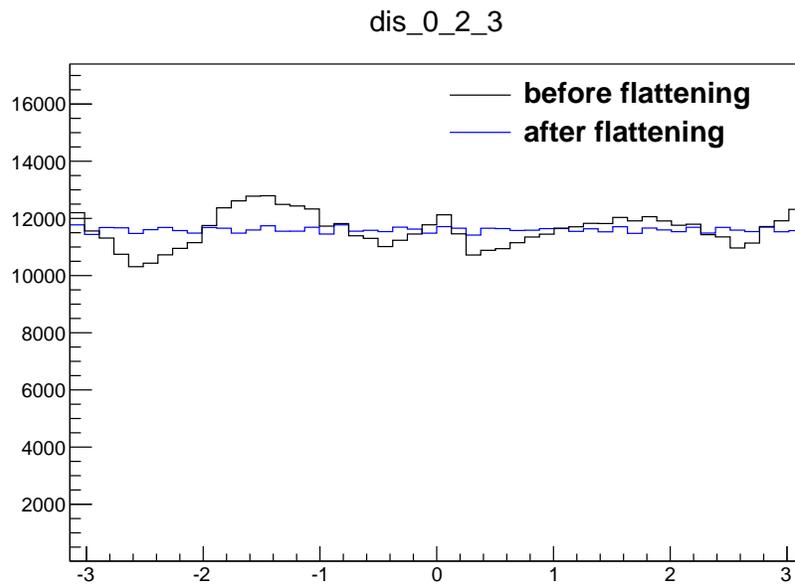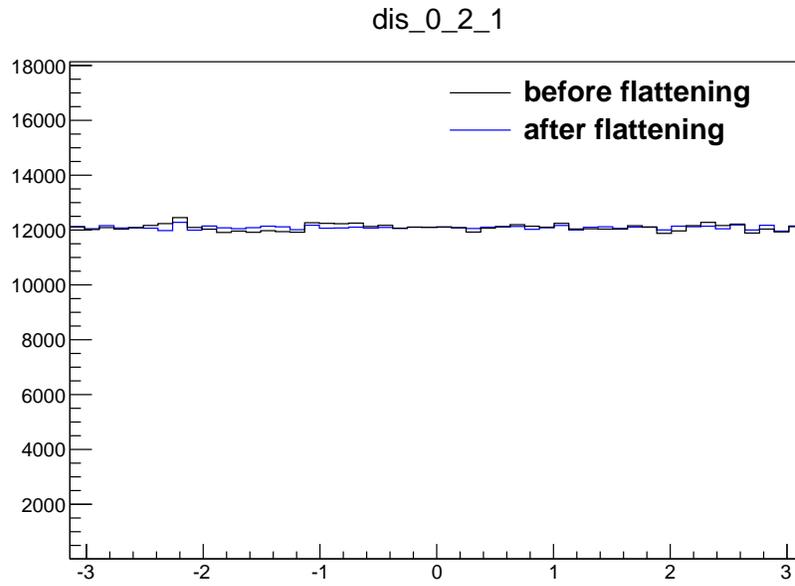
Figure 4.16: The Ψ_3 distribution before and after event-plane flattening procedure, upper panel is BBC south event plane, and lower panel is FVTX south event plane.
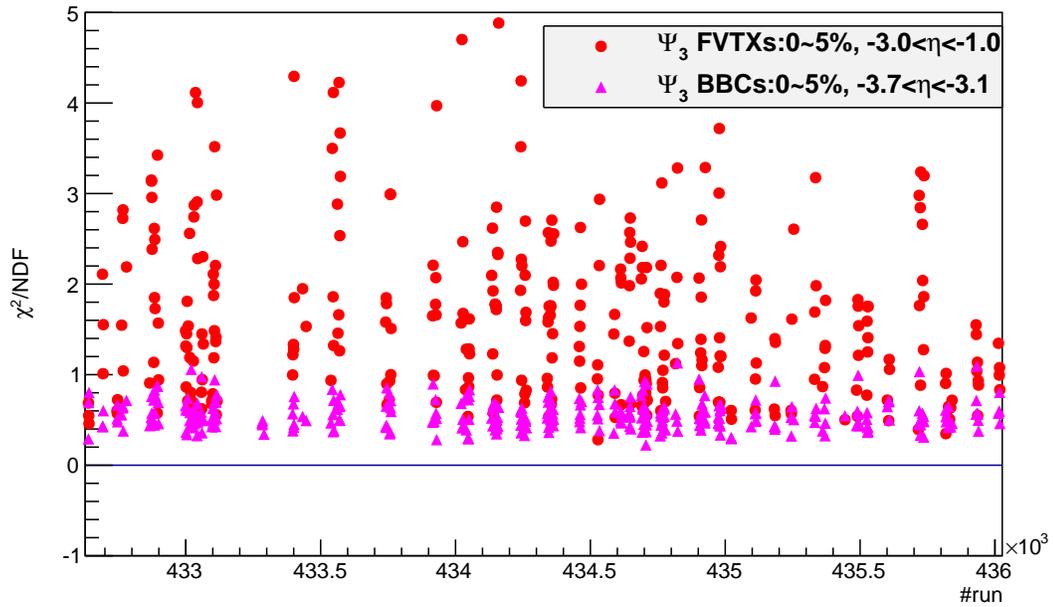
Figure 4.17: The χ^2/NDF from constant fitting of each run for the Ψ_3 of the BBCs and FVTXs event plane vs. run number.
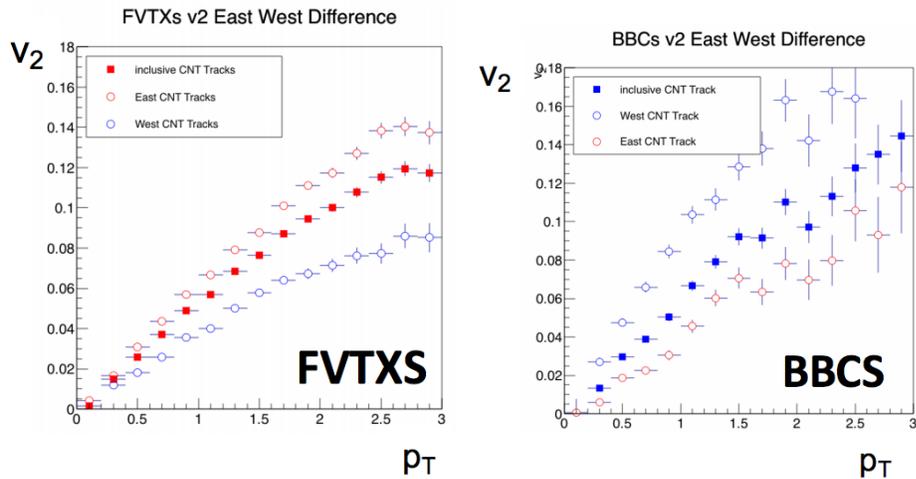
Figure 4.18: The left plot shows the east-west difference in the measurement of v_2 using the FVTX south event plane. The right plot is with the BBC south event plane. There is about 25% difference in the FVTXs measurement and a 40% difference in the BBCs measurement.
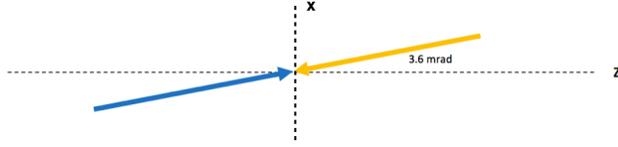
Figure 4.19: A vector diagram illustrating the yellow and blue beam angle.

factor in the FVTX is determined using a data-driven method of inverse ϕ weighting. For this method, the weight factor is determined by plotting all hits in a cylindrical disk detector vs ϕ, normalizing this distribution to unity, and then inverting it. When applying this weight factor to the data, it will produce uniform hit distributions in ϕ in the detectors it is applied to. This will, in turn, make the event plane distribution more uniform when measured in those detectors, thus correcting for the effect.

For the BBC south, the method was slightly changed to correct for the non-uniform particle distribution. Using the distribution of particles in the BBC from the Run15 pp dataset as a baseline, one can apply an inverse ϕ weighting much like the one described in the previous paragraph. In the Run15 pp dataset, there was no issue with the beams colliding at an angle, and the average charge across all 64 PMTs in the BBCs is uniform. In this method, the weight for each PMT is calculated as the charge of the PMT times the average Run15 pp charge of the PMT divided by the average Run15 pAu charge of the PMT.

The combined effect of all these corrections not only makes the east and west arm v_2 measurements using the FVTXs or the BBCs agree to a much better degree, it makes the inclusive v_2 measurements performed with the BBCs or FVTXs agree as well.

$$weight(\phi) = \frac{1}{(\#of\ clusters(\phi)/average\#)} \tag{4.1}$$

The ϕ-weighting is from a data-driven method, which is performed separately in different vertex z bins and run segments. Fig. 4.20 shows the weight applied to the second layer of

FVTX, in the [-10,-8] cm vertex bins and in one segment of run number 435527. If the weight is out of the range of [-20%,20%] of the mean value, we think that this is a bad cluster and skip that cluster:
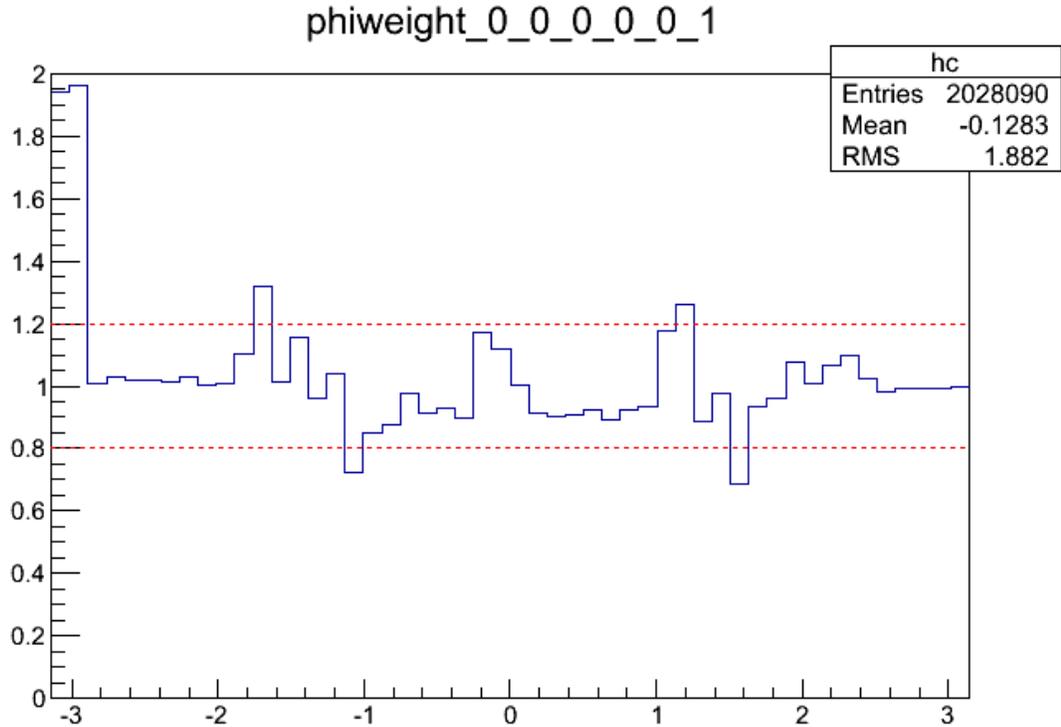
Figure 4.20: weight as a function of azimuthal angle, used in event plane calculation.

The individual 3rd layer yields a very large east/west difference, as shown in Fig. 4.21.

4.3.3 TOF Calibration

4.3.3.1 Bad Slats Removal

There are some bad slats in TOF west and east arm detectors. For good slats, the dϕ and dz distribution should be Gaussian distributed, such as in Fig. 4.22. For some slats, the dϕ and dz distribution show double peaks. Some of the double peaks are distinguishable and one peak will be removed by the 2σ Gaussian cut of the TOF matching, as show in

45
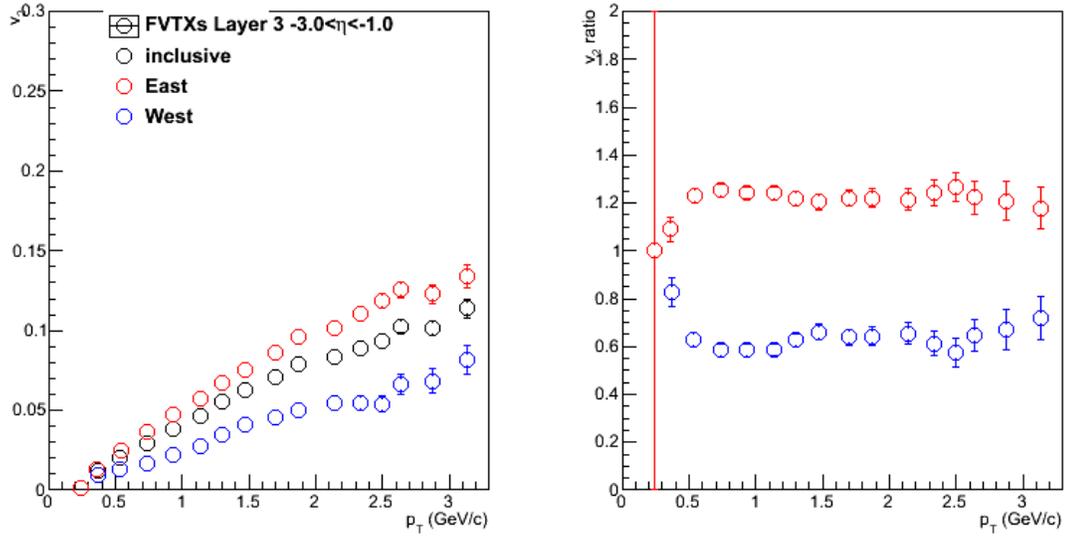
Figure 4.21: Individual 3rd layer in FVTX south detector v_2 east/west differences can reach as high as 60%.

Fig. 4.24, but there are some slats in which the double peak cannot be resolved and we will remove these slats. There are also some slats, in which the signals are very unstable, as shown in Fig. 4.23; we will also remove these slats to ensure the high quality of the selected particles.

4.3.3.2 Hit Position Offset

Due to hardware-related issues, some strips on the TOF west detector have some hit position offset. We need to calculate this offset by fitting the offset with a Gaussian function for each strip and extract the mean. Because some of the offset is very large, two passes were made to calculate the offset. In order to see if there is any vertex dependence, we separate the data into six vertex bins, -30 to -10, -10 to -5, -5 to 0, 0 to 5, 5 to 10 and 10 to 30 cm.

The results for the second vertex bin as an example are shown in Fig. 4.25, 4.26, 4.27 and 4.28.
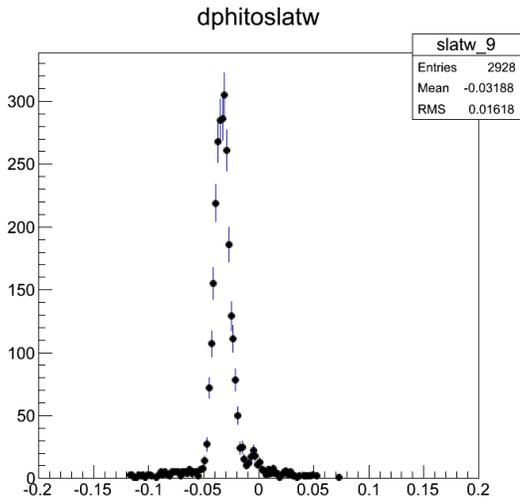
Figure 4.22: The dϕ distribution of slat number 9 in TOF west arm.
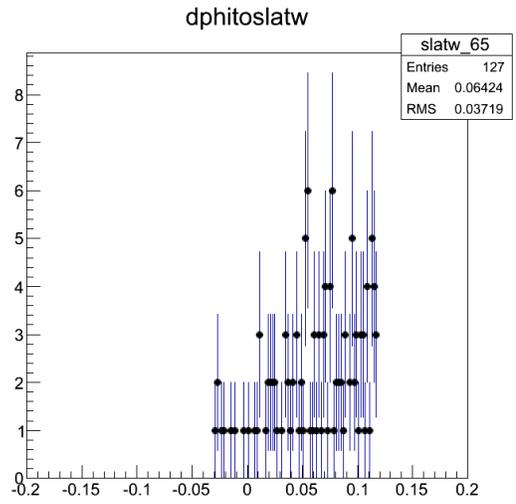
Figure 4.23: The dϕ distribution of slat number 65 in TOF west arm.
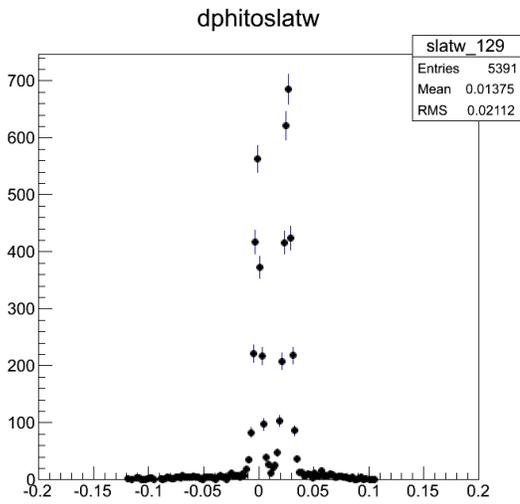
Figure 4.24: The dϕ distribution of slat number 129 in TOF west arm.
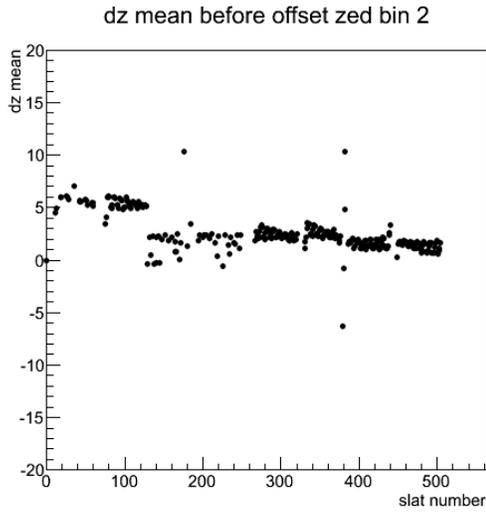
Figure 4.25: Hit position offset in the z-direction before correction.
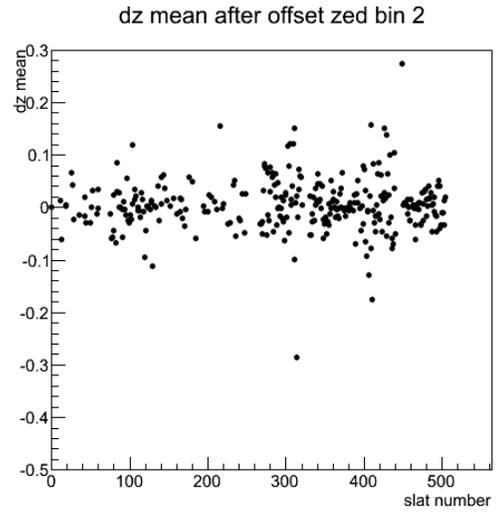
Figure 4.26: Position offset in z-direction after correction.
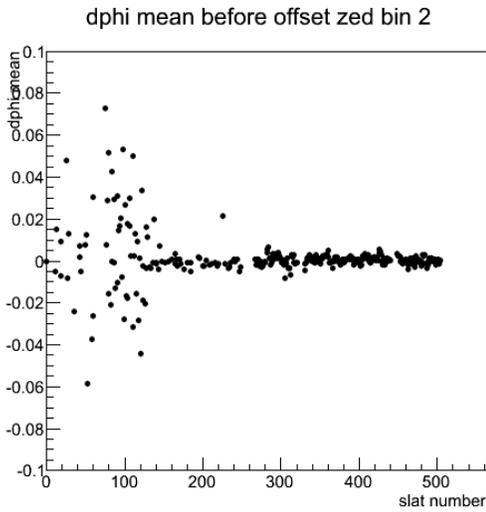
Figure 4.27: Hit position offset in the ϕ direction offset before correction.
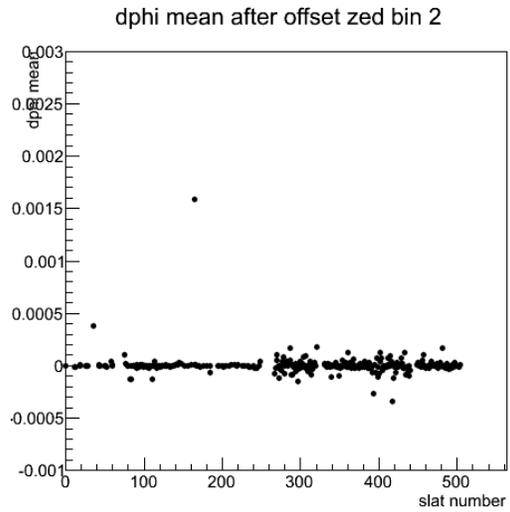
Figure 4.28: Hit position offset in the ϕ direction offset after correction.

48

To do the time calibration, we use the pions as the standard, because the pions are the most abundant particles produced. The time measured by the detector is denoted by t_{mean}, and the time calculated by theory, e.g. - using the known detector geometry and the mass of the pion, is denoted by t_{theo}. The difference between these two values should be a Gaussian function centered at zero. However, because of some hardware conditions such as uneven cable length and time-walk effects of the pulse-height spectrum (slewing effect), there are channel-by-channel timing offset that need to be calibrated in several steps.

4.3.3.3   Slat-by-Slat Offset

Before doing the slat and run time calibration, we find the Δt for TOFw has an overall shift of nearly 30 ns from 0 as shown in Fig. 4.29. So, we need to move it back to 0. To do this, we fit the Δt for each slat with a Gaussian function and subtract the mean value from the Δt. The Gaussian fit of slat number 11 is shown in Fig. 4.30.

The Δt distribution after the slat by slat correction is shown in Fig. 4.31. After this slat offset, we can clearly see the three peaks in the timing distributions, which correspond to pions, kaons, and protons.

4.3.3.4   Run-by-Run Offset

Due to the different configurations between different runs, their Δt may have different mean values. To remove this difference, we need to do a run-by-run offset. The Δt distribution for run number 432639 is shown in Fig. 4.32. We fit it with a Gaussian and get the mean value for this specific run and then subtract the mean value from time measured during this run.
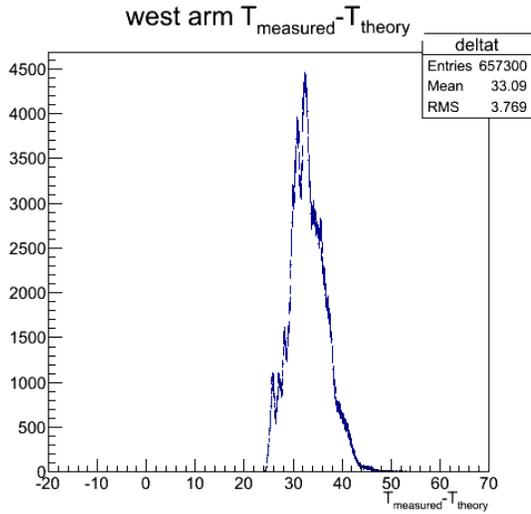
Figure 4.29: The raw Δt distribution of TOFw for all slats.
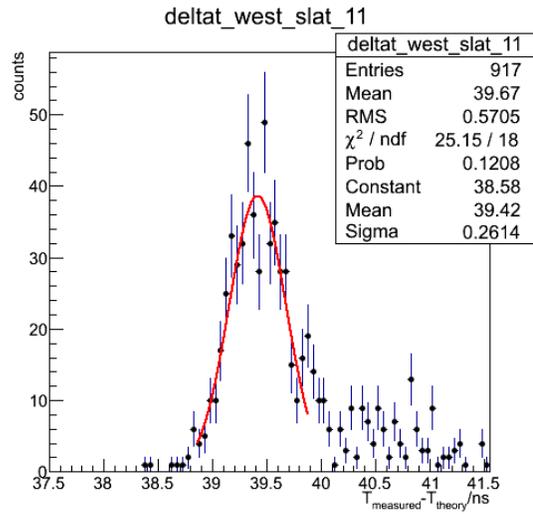
Figure 4.30: A Gaussian fit on the *Delta*t distribution for TOFw, slat number 11.
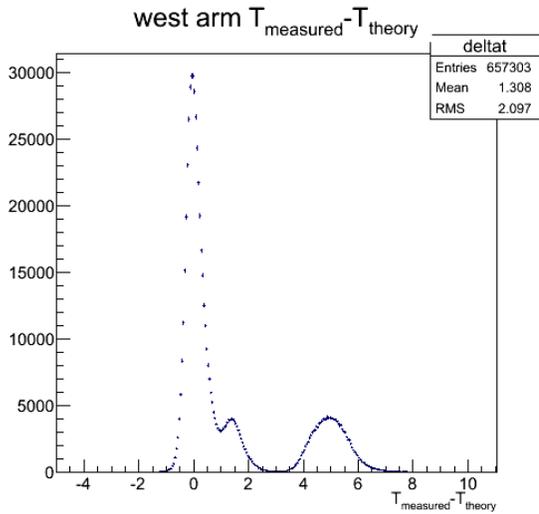
Figure 4.31: The Δt distribution of TOFw after a timing offset is applied.
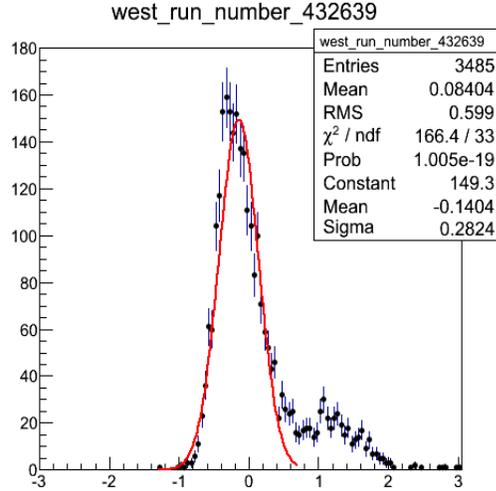
Figure 4.32: The Δt distribution for run number 432639 with all the slats together.

4.3.3.5 Slewing Calibration

The method used to measure the TOFW timing may introduce an amplitude-dependent error. As shown in Fig. 4.33, the two signals should trigger at the same time, however, because of the fact that there exists a minimum level of trigger, the signal with lower amplitude will trigger later, introducing some errors. We need to fix this using a method called slewing calibration. The effect is slat related so it is corrected slat-by-slat. The offset caused by the effect is a function of the average integrated charge of one MRPC strip. The functional form is as follows:

$$T_{slewing} = A + (B/ADC_{STRIP}^{0.4})$$

where ADC is defined as

$$ADC = \sqrt{Q_{up}Q_{down}}$$

So, we draw a 2-D histogram of Δt and ADC and fit it with a two-parameter function. The fit results for slat 11 and slat 489 are shown in Fig. 4.34 and 4.35.
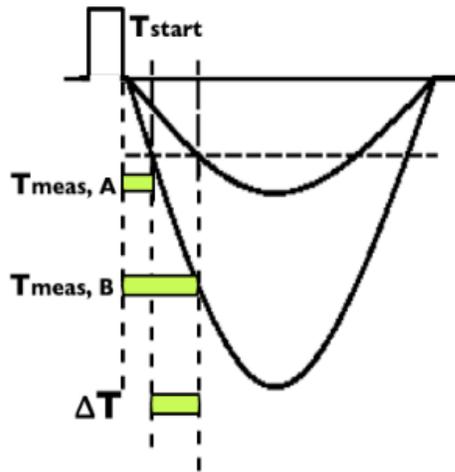
Figure 4.33: Small Pulse Height Induced Time Walk.
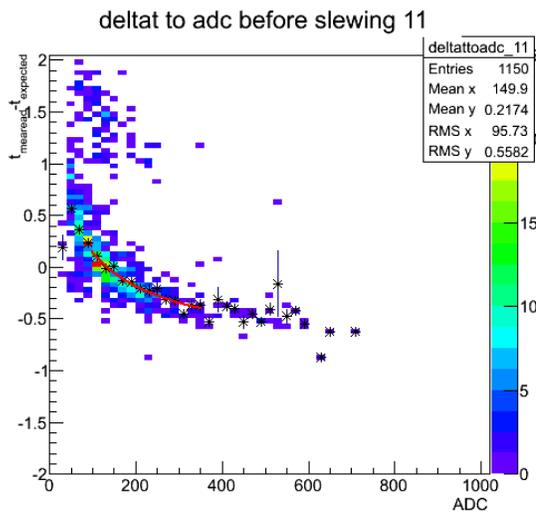
Figure 4.34: Slewing calibration example for slat number 11. The plot shows the correction between ADC values and Δt for all runs together.
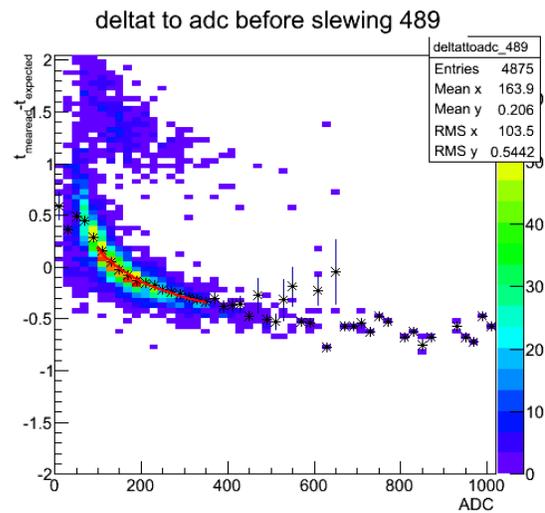
Figure 4.35: Slewing calibration example for slat number 489. The plot shows the correction between ADC values and Δt for all runs together.

4.3.3.6 Slat-by-Slat and Run-by-Run Calibration

After the slewing calibration, we redo the slat-by-slat calibration and run-by-run calibration twice to further reduce the Δt dependence on slat number and run number, the plots are show in Fig. 4.36, 4.37, 4.38 and 4.39.
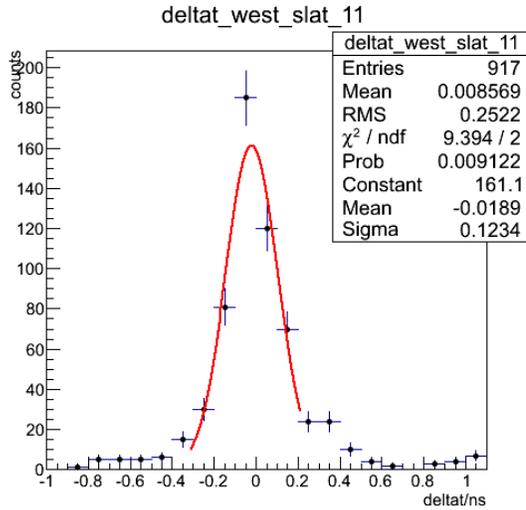
Figure 4.36: First round of slat-by-slat calibration; example fit on slat number 11.
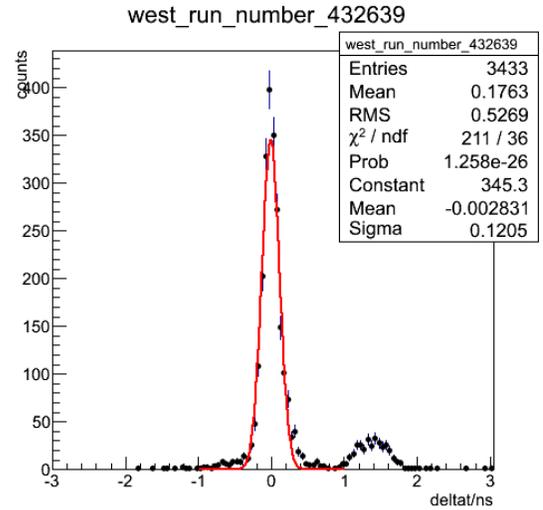
Figure 4.37: First round of run-by-run calibration; example fit on run number 432639.
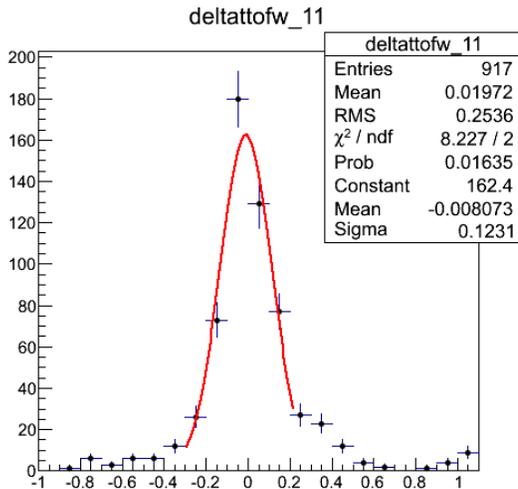
Figure 4.38: Second round of slat-by-slat calibration; example fit on slat number 11.
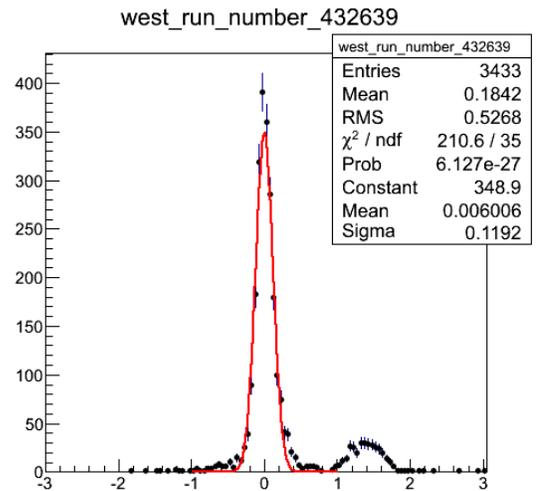
Figure 4.39: Second round of run-by-run calibration; example fit on run number 432639.
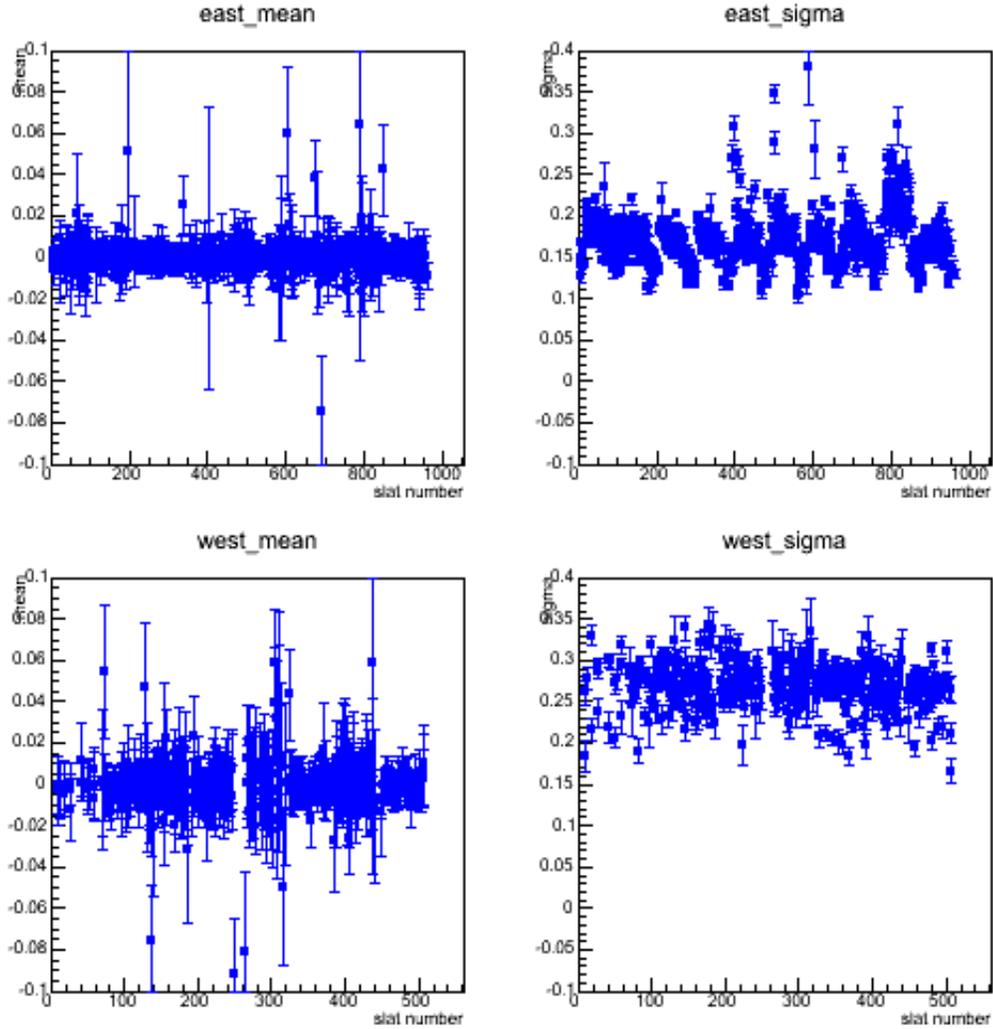
Figure 4.40: The slat-by-slat mean and sigma of Δt distributions before time calibration.

4.3.3.7   Time Resolution after Calibration

In this section we will have a look at the slat-by-slat and run-by-run time resolution before and after the timing calibration. Fig. 4.40 shows the mean and standard deviation σ of the Δt distribution as a function of slat number, and Fig. 4.42 shows the same parameter distribution after timing calibration, we can see there is a large improvement for the timing resolution of the west arm. Also Fig. 4.41 and 4.43 show the run-by-run result.
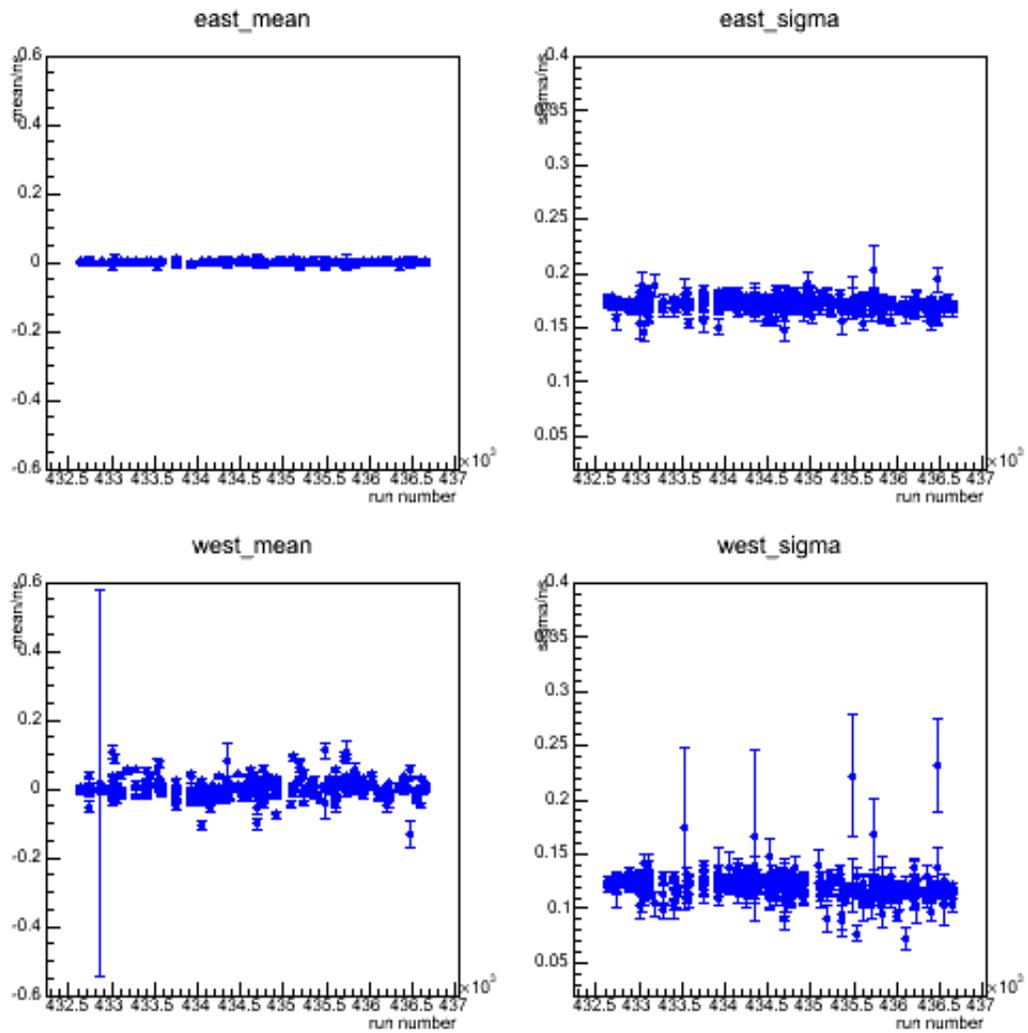
Figure 4.41: The run-by-run mean and sigma of Δt distributions before time calibration.
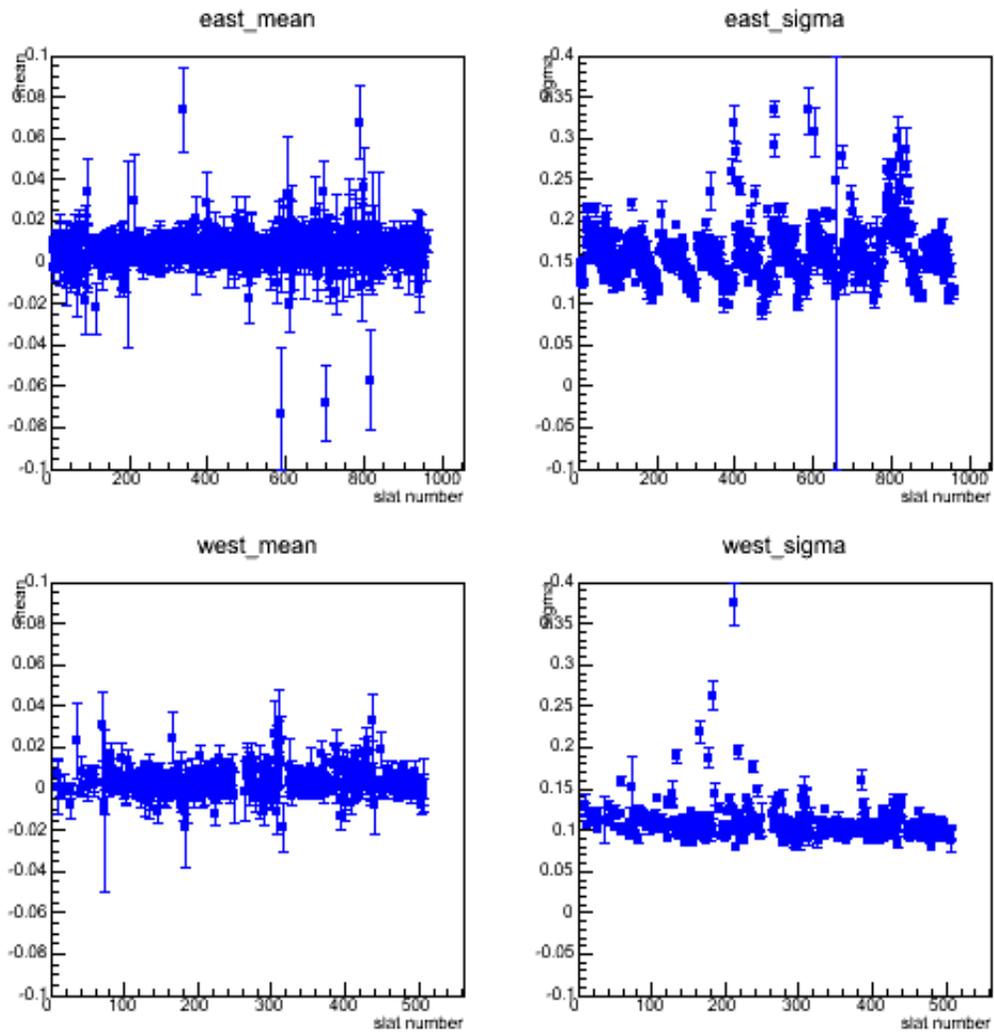
Figure 4.42: The slat-by-slat mean and sigma of Δt distributions after time calibration.
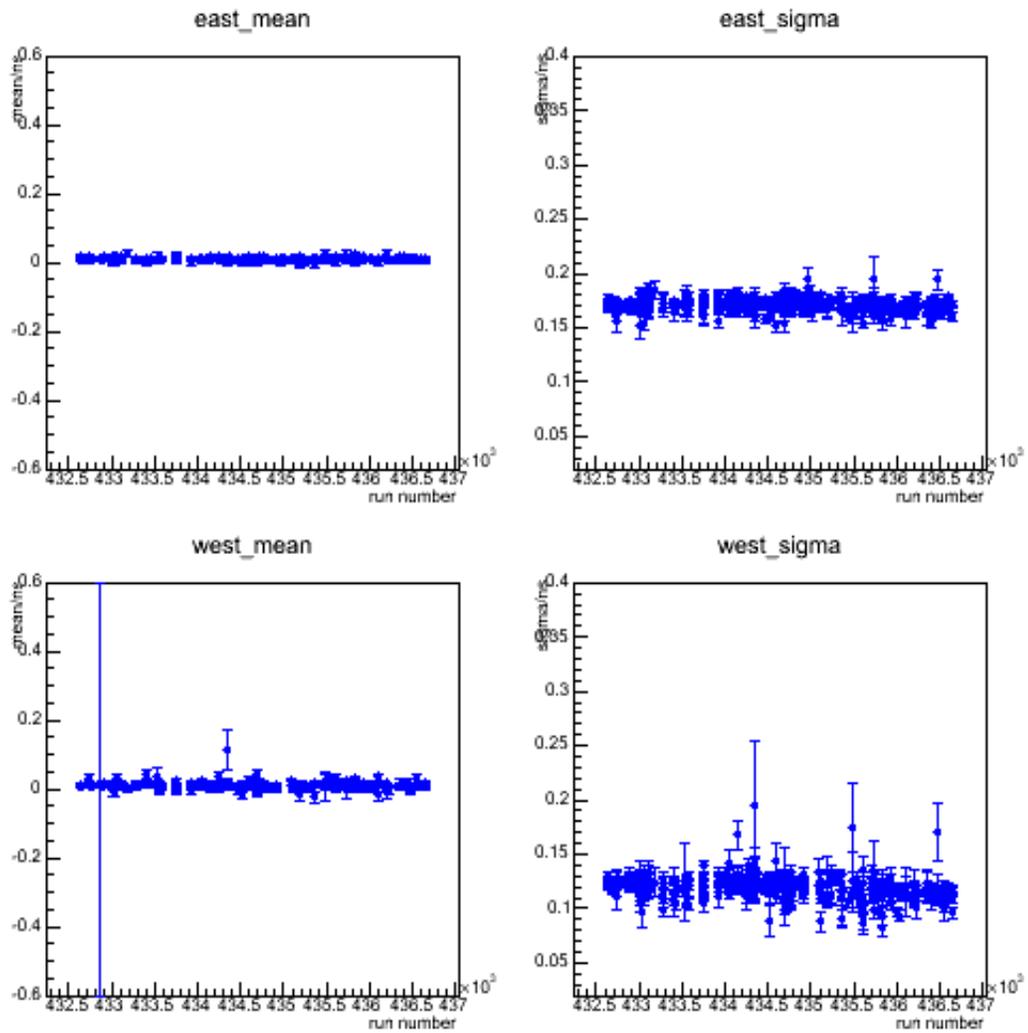
Figure 4.43: The run-by-run mean and σ of the Δt distributions after time calibration.

4.4 Particle Identification

Particle Identification (PID) uses Time-of-flight detectors. After going through the previous steps, the TOF detectors are well-calibrated and the data can be used for analysis.

We now define the selections that will allow us to identify pions, kaons, and protons. Figure 4.44 shows the mass-squared m^2 distribution as a function of $p_T \times$charge for the West arm, and Fig. 4.46 shows the result for the East arm TOF detectors. Figure 4.45 shows the m^2 plot of West arm projection to p_T range 1.8-1.9 GeV and Fig. 4.47 shows the same result from the East arm. The distributions are fitted with a triple Gaussian to extract the mean and σ of the three particle peaks (pion, kaon, and proton). After we extract the mean and σ for different p_T bins; we fit the $\sigma(p_T)$ and parameterize it using the angular resolution σ_α of the DC, a multiple scattering term, σ_{ms}, and the timing resolution of the TOF detector σ_t in the following equation:

$$\sigma_{m^2}^2 = \frac{\sigma_\alpha^2}{K^2}(4m^4 p^2) + \frac{\sigma_{ms}^2}{K^2}(4m^4(1 + \frac{m^2}{p^2})) + \frac{\sigma_t^2 c^2}{L^2}(4p^2(m^2 + p^2)) \qquad (4.2)$$

The fitted result for the West arm is shown in Fig. 4.48, and the result for the East arm is shown in Fig. 4.49. The extracted parameters using equation 4.2 are shown in the Table 4.1, the three parameters: angular resolution, multiple scattering, timing resolution are discussed in the text above, and the fitting with this function is done for the East and West arm separately, negative and positive particles - separately, and pions, kaons, and protons - separately. We notice that both in the East and in the West arm the m^2 distributions for protons at low p_T are much wider than those of anti-protons. This is also reflected in the value of the extracted multiple-scattering term. This is unphysical, since the multiple scattering is related to the detector material that the particles see, and it should be comparable for all particles. This indicates that the protons are contaminated by background that is not removed after PC3 matching. We investigate this issue further by applying a cut based on the track's distance-of-closest approach (DCA) to the collision vertex measured by the
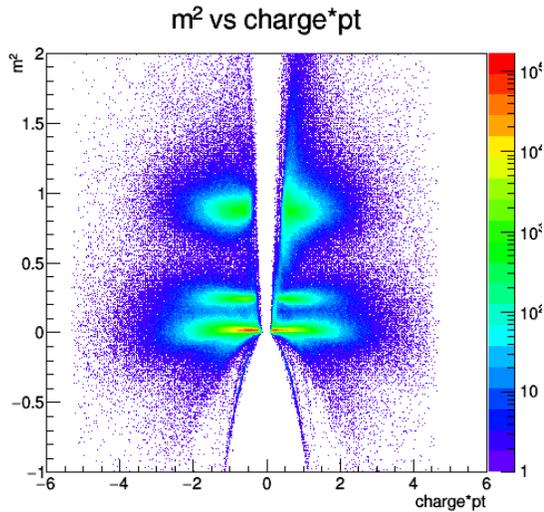
Figure 4.44: Charged-particle mass-squared versus p_T 2D distributions for TOF west arm in real data.
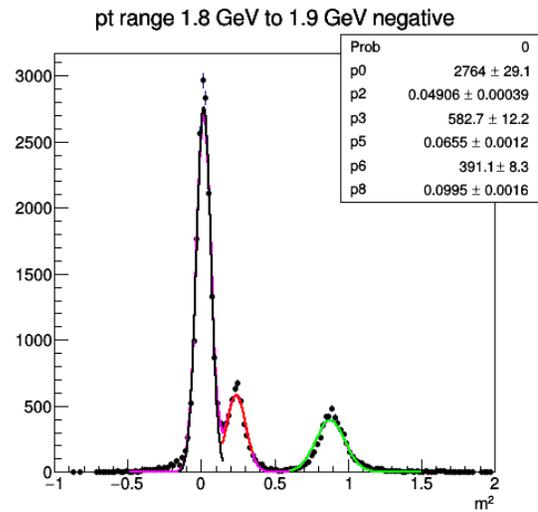
Figure 4.45: Projections of the mass-squared distribution for the p_T range 1.8-1.9 GeV/c for TOF west arm.
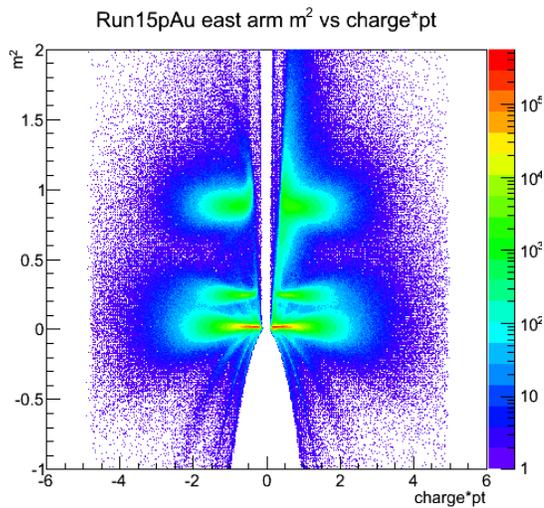
Figure 4.46: Charged particle mass-squared versus p_T 2D distribution for TOF east arm in real data.
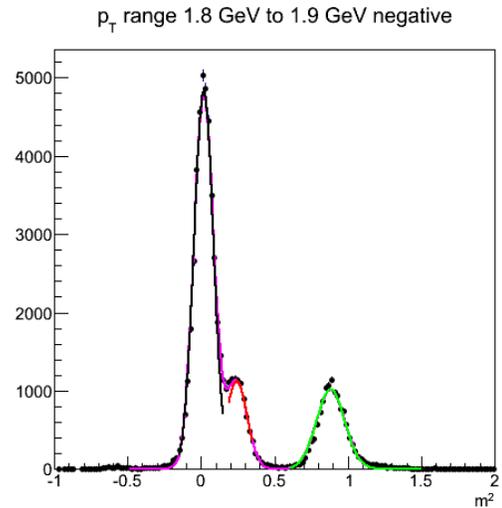
Figure 4.47: Projections of the mass-squared distribution for the p_T range 1.8-1.9 GeV/c for TOF east arm.

59
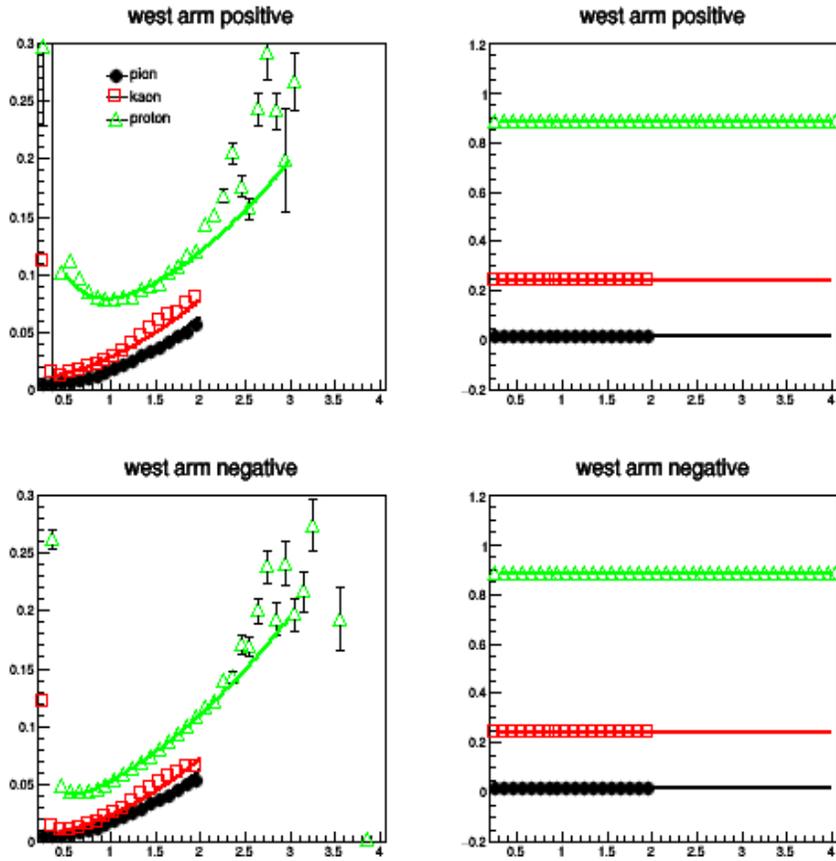
Figure 4.48: (Left) The detector time resolution as a function of p_T for TOF west arm. (Right) Mean of the particle mass as a function of p_T for TOF west arm. (Top) are for positive particles, (Bottom) are for negative particles.

VTX detector as explained further in Section 4.5.

The m^2 distribution plot after the DCA cut is shown in Fig. 4.69. The projection of m^2 to different p_T bins before and after the DCA cut is shown in Figs. 4.65–4.68. This cut resolves the problem. After that, we use the same PID bands for positive and negative particles.
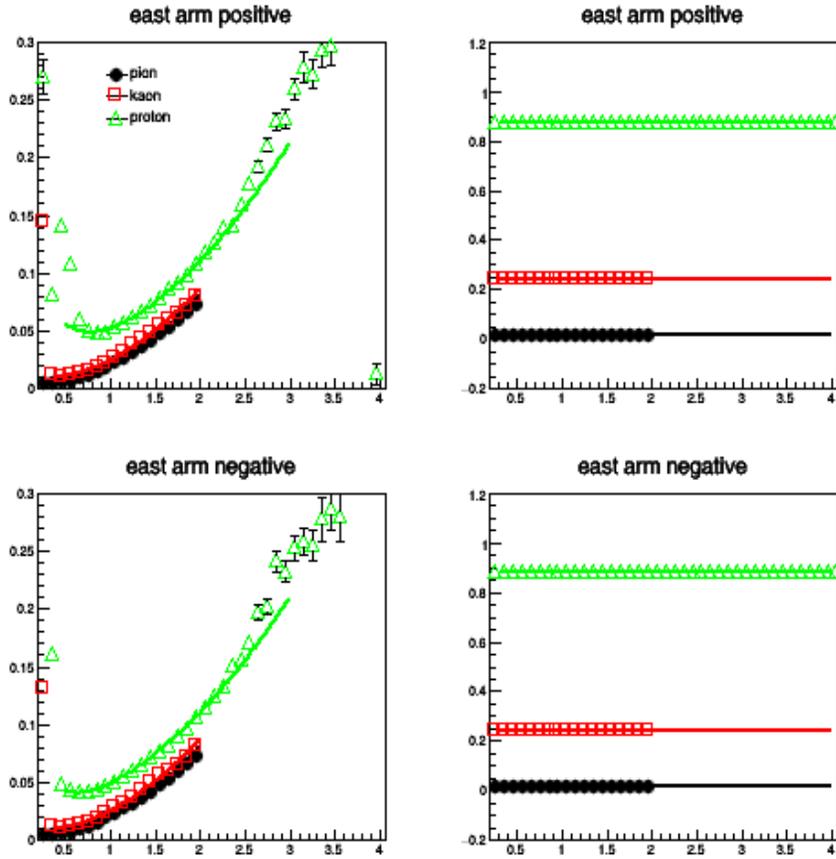
Figure 4.49: (Left) The detector time resolution as a function of p_T for TOF east arm. (Right) Mean of the particle mass as a function of p_T for TOF east arm. (Top) are for positive particles, (Bottom) are for negative particles.

Table 4.1: Fitting parameters in equation 4.2 for TOF east/TOF west pion/kaon/proton separately.

	angular resolution	multiple scattering	timing resolution
west pos pion	10	10	0.13
west pos kaon	3.5	1.35	0.16
west pos proton	2.38	2.76	0.13
west neg pion	10	10	0.13
west neg kaon	3.11	0.4	0.13
west neg proton	2.4	0.97	0.13
east pos pion	1.3	1.0	0.17
east pos kaon	1.3	1.09	0.17
east pos proton	1.58	1.49	0.17
east neg pion	9.6	10	0.16
east neg kaon	1.57	1.08	0.17
east neg proton	1.84	1.06	0.16

4.5 Background Proton Study

4.5.1 The Problem of Background Protons

In the m^2 vs *charge* $\times$ p_T distributions 4.65 and 4.67, we can see that the protons spread wider than anti-protons. To understand the reason we performed further studies.

The Monte-Carlo simulation study is a powerful way to study the detector effect. PHENIX provides a full detector simulation package called PISA [55]. In the simulation, we simulate 15 million pions. The p_T distribution of the simulated particles is flat, the vertex zed distribution is -10 centimeters to 10 centimeters, x and y position are set to be zero, the ϕ angle is centered at 0.25, which is the center of the TOF west detector and varies from -π to π, and the rapidity range is flatly distributed between -0.6 to 0.6. Because of this, most particles are out of the detector range, and we get only around 155K pions and about 1.5K background protons. This means that the produced background protons are about 1% of the produced pions, which is comparable to the real protons in real data. We also examined the parent of the background protons and found that the parent of the protons are pions. Because it is obvious that the pions cannot decay into protons, the background protons must come from somewhere else, we suspect that they are knocked out from the detector material. To test this, we plot the vertex position of the background protons, as shown in Fig. 4.50.

From the Fig. 4.50, we can see clearly that there is a pattern of the vertex positions of background protons, and that these vertices correspond to the position of the VTX detector. So, the background protons are coming from the VTX detectors knocked out by pions and/or kaons.

4.5.2 DCA Cut and the Cut Effect in Simulation

To remove the background in the proton sample, the VTX detector [56] is used in conjunction with the DC to select proton tracks with $p_T < 1$ GeV/c based on their distance
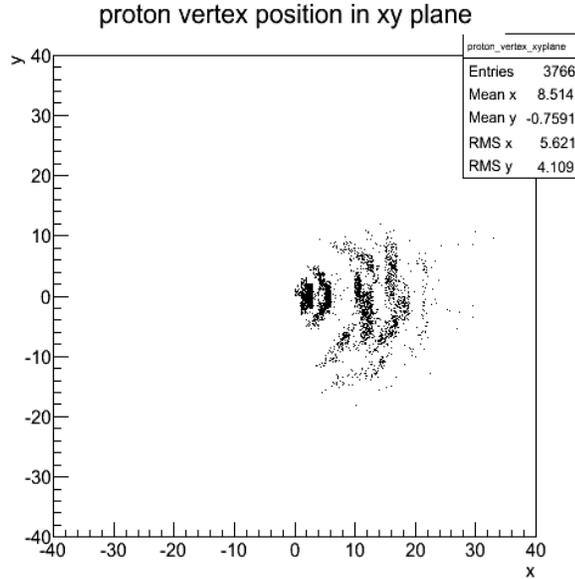
Figure 4.50: Proton vertex position in xy plane in Monte-Carlo study.

of closest approach to the primary vertex in the xy plane transverse to the beam direction. It is defined as the shortest distance from the vertex to the secondary tracks as illustrated in Fig. 4.51.

To define a DCA cut, we fill a histogram with DCA2d value in 50 different p_T bins, East arm and West arm, positive and negative particles separately. Then we fit the distribution with a double Gaussian, extract the mean and sigma to calculate the standard deviation for the signal. Fig. 4.52 is an example of a DCA distribution, which is for positive particles detected in the west arm, in the p_T range of 1.8-1.9 GeV.

In the simulation, we did the PC3 track matching and TOF track matching as in real data and cut two standard deviations σ. After that, we plot the m^2 for negative pion input and positive pion input separately. For both cases, we see proton background but no anti-proton background, as shown in Fig. 4.53 and Fig. 4.54. We also simulate negative kaons and positive kaons in the detector, and we also found that there are background protons produced by kaons, as shown in the m^2 plot for kaons in Fig. 4.55 and Fig. 4.56. The simulation for proton input particles is shown in Fig. 4.57 and Fig. 4.58.

electron track

magnetic field

Primary vertex

R (=bending radius)

Center of the circle

L (=distance)

$$DCA_T \equiv L - R$$
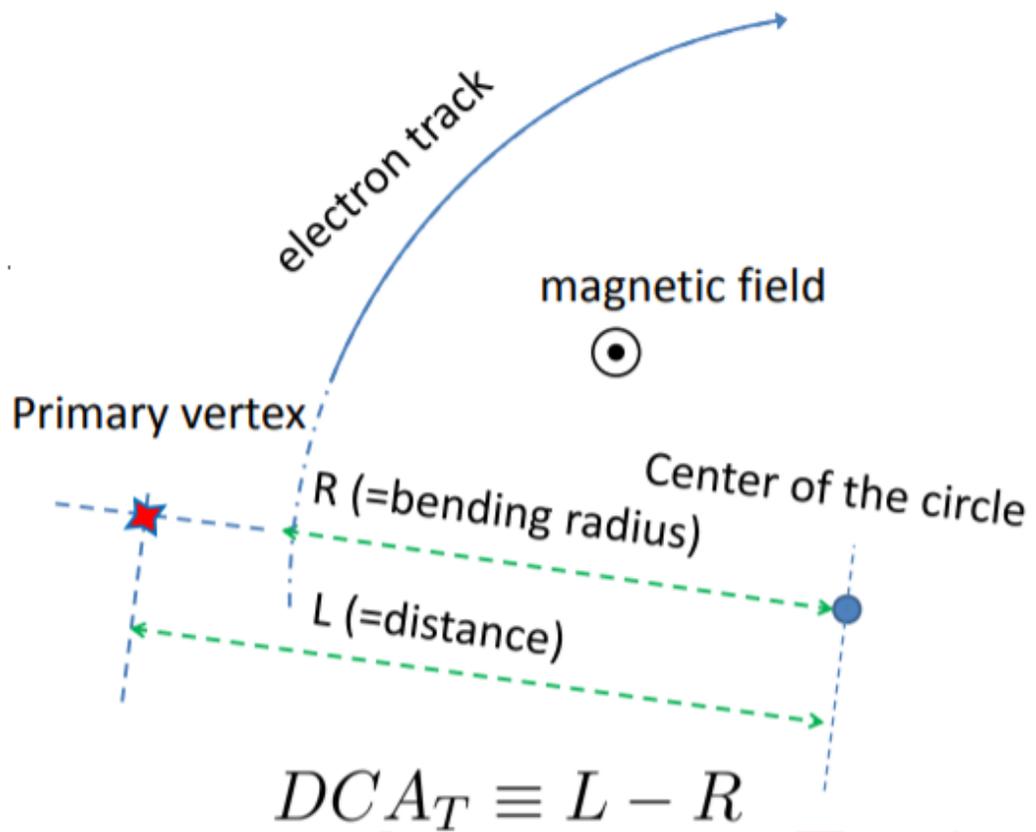
Figure 4.51: Schematics figure to illustrate the definition of DCA in VTX detector.
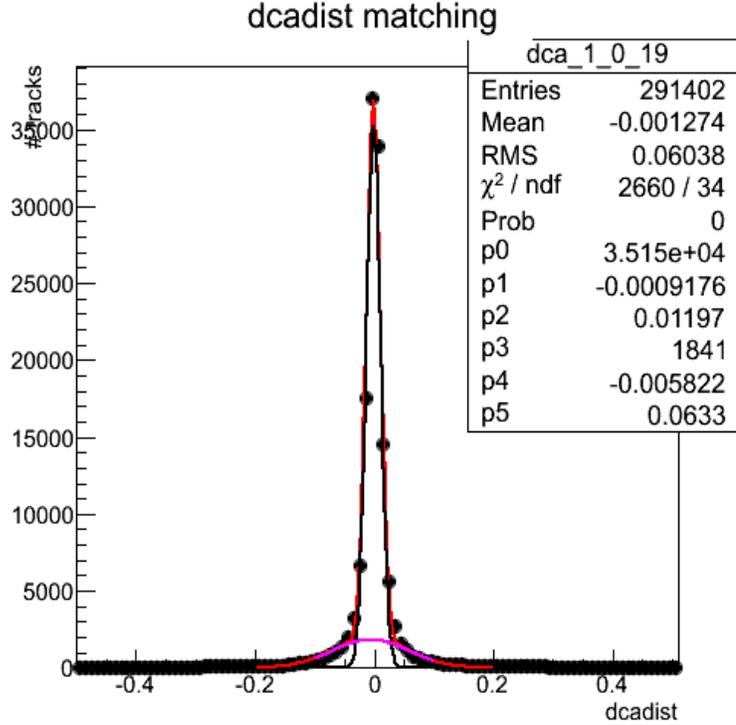
Figure 4.52: DCA2d distribution in p_T range 1.8-1.9 GeV for west arm positive particles.

To test the effectiveness of the DCA cut, we applied the DCA cut and re-plotted the m^2 plot, as shown in Figs. 4.59 – 4.64. We can see from these figures that the background particles are removed.

4.5.3 DCA Cut and the Cut Effect in Real Data

We require the track measured by CNT with a DCA value less than 2 σ. This will cut a lot of background protons. The m^2 plot after DCA cut is shown in Fig. 4.69.

We can see that after the DCA cut, the positive proton band becomes much narrower, which means that the background protons are reduced significantly.

We calculated the v_2 values for protons and anti-protons after the DCA cut and compared them with the values before the DCA cut. The results are shown in Figs. 4.70 and 4.71.

In p+Au collisions after the cut the v_2 value of protons at low p_T is lower than before
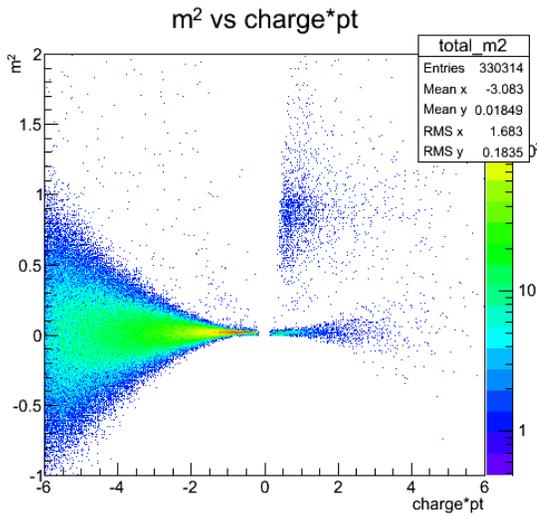
Figure 4.53: Charged particle mass-squared versus p_T 2D distribution for negative pion input in MC-simulation.
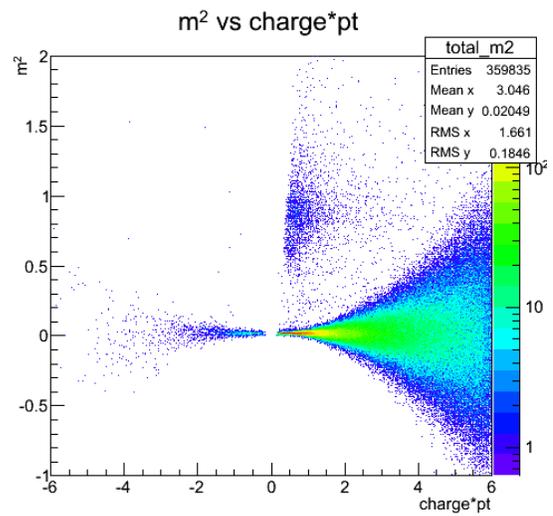
Figure 4.54: Charged particle mass-squared versus p_T 2D distribution for positive pion input in MC-simulation.
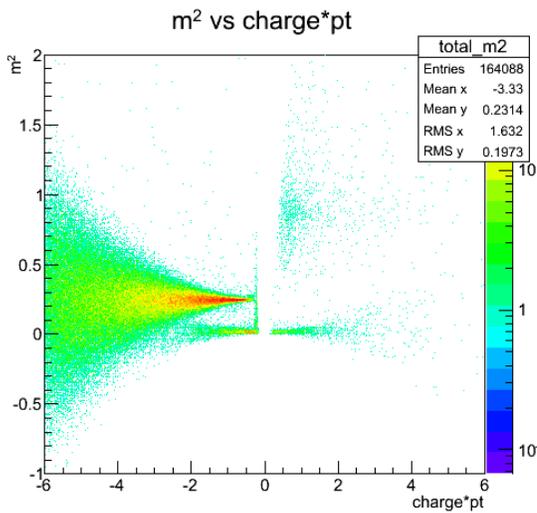
Figure 4.55: Charged particle mass-squared versus p_T 2D distribution for negative kaon input in the MC-simulation.
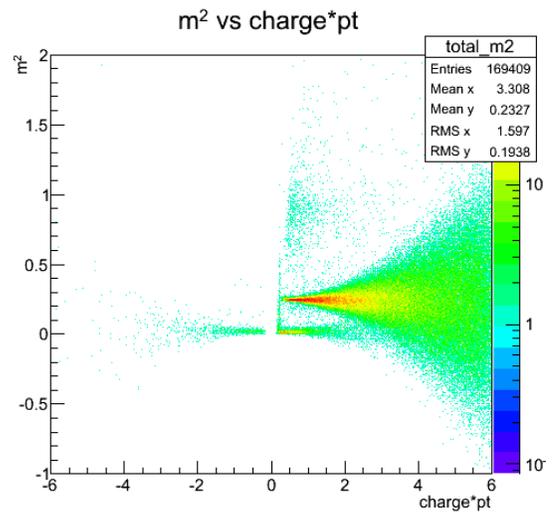
Figure 4.56: Charged particle mass-squared versus p_T 2D distribution plot for positive kaon input in the MC-simulation.
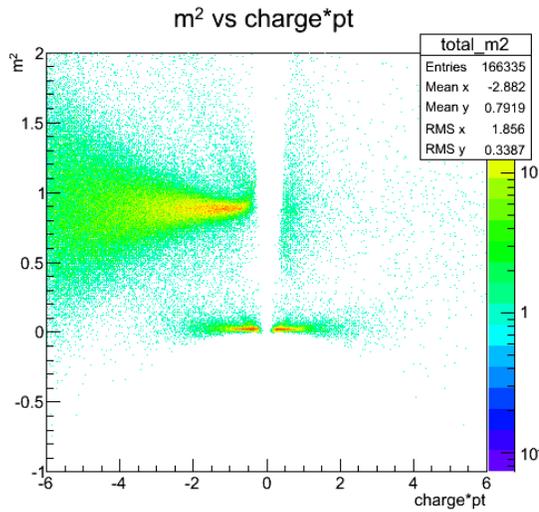
Figure 4.57: Charged particle mass-squared versus p_T 2D distribution for negative proton input in the MC-simulation.
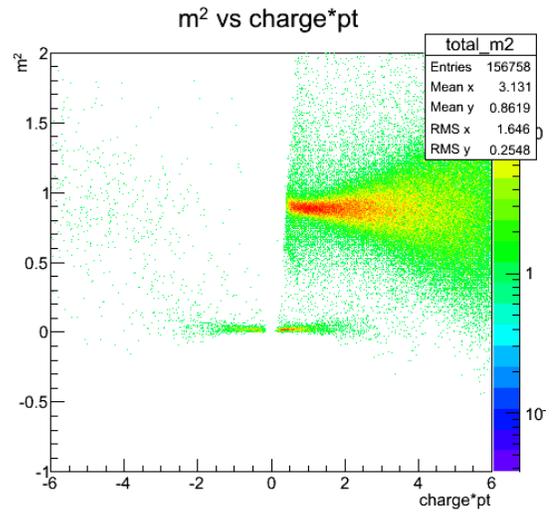
Figure 4.58: Charged particle mass-squared versus p_T 2D distribution for positive proton input in MC-simulation.
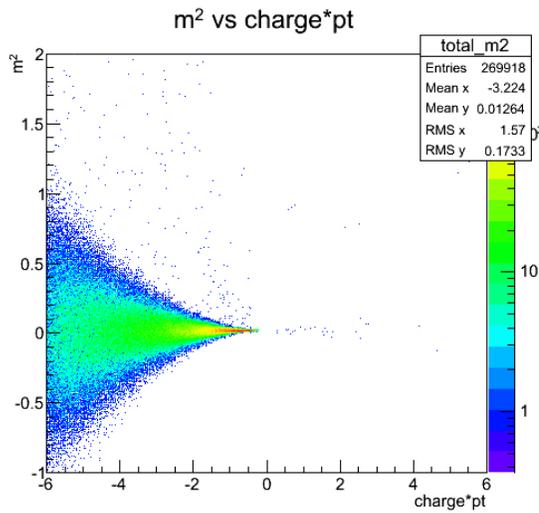
Figure 4.59: Charged particle mass-squared versus p_T 2D distribution for negative pion input after DCA cut in the MC-simulation.
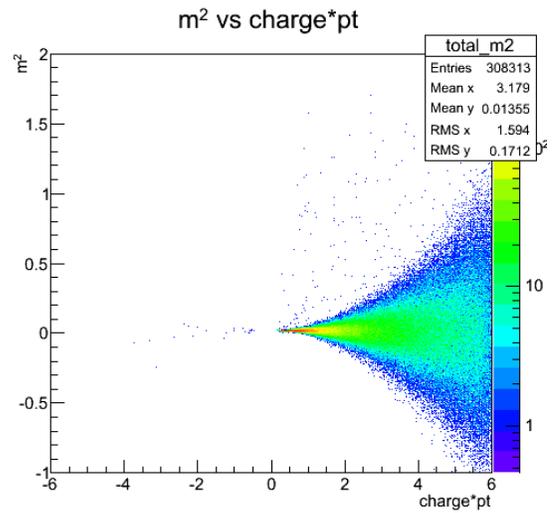
Figure 4.60: Charged particle mass-squared versus p_T 2D distribution for positive pion input after DCA cut in the MC-simulation.
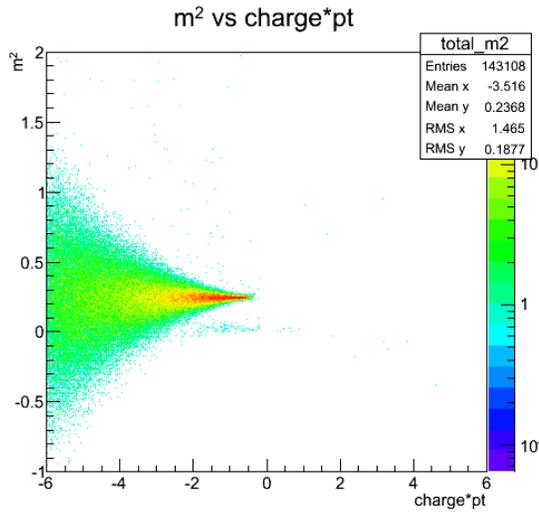
Figure 4.61: Charged particle mass-squared versus p_T 2D distribution plot for negative kaon input after DCA cut in the MC-simulation.
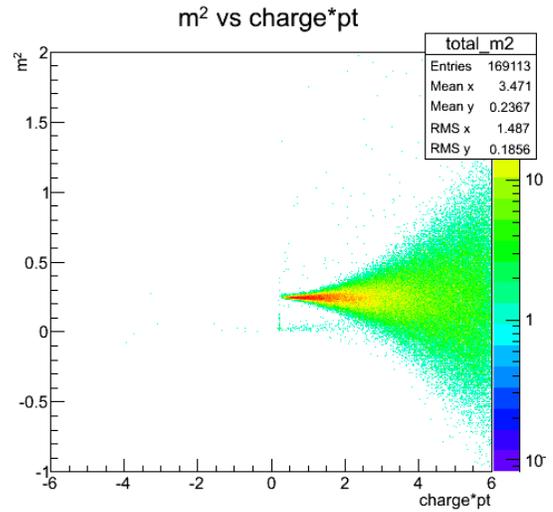
Figure 4.62: Charged particle mass-squared versus p_T 2D distribution plot for positive kaon input after DCA cut in the MC-simulation.
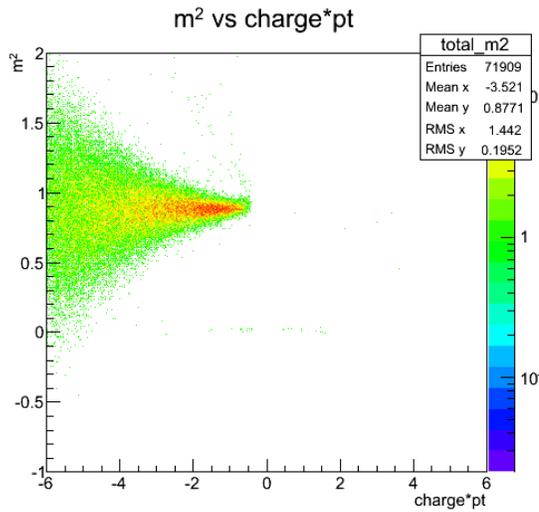
Figure 4.63: Charged particle mass-squared versus p_T 2D distribution plot for negative proton input after DCA cut in the MC-simulation.
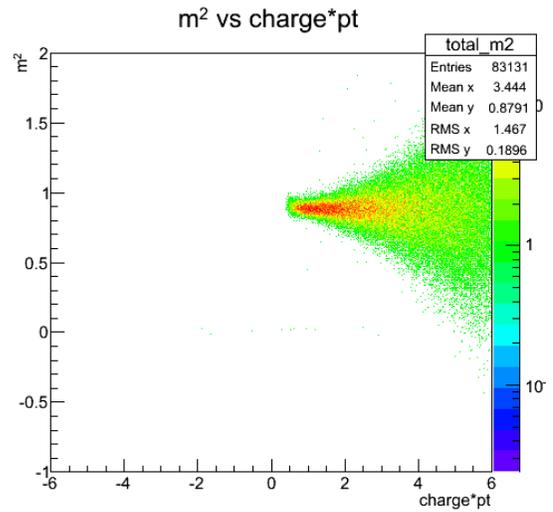
Figure 4.64: Charged particle mass-squared versus p_T 2D distribution plot for positive proton input after DCA cut in the MC-simulation.
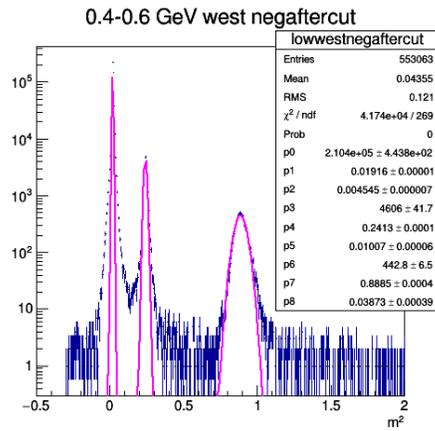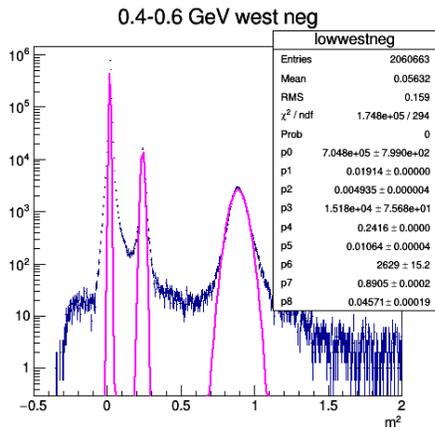
Figure 4.65: Negative charged Particle mass square 1D distribution plot using the West arm before the DCA cut.

Figure 4.66: Negative charged particle mass-squared 1D distribution plot using the West arm after the DCA cut.
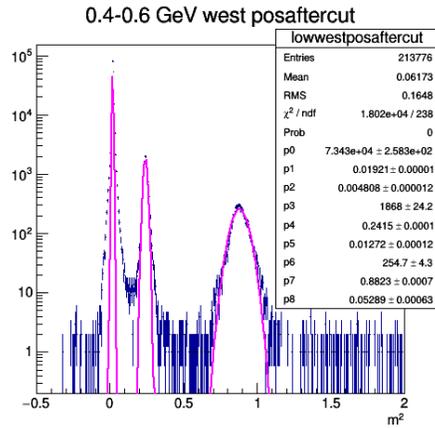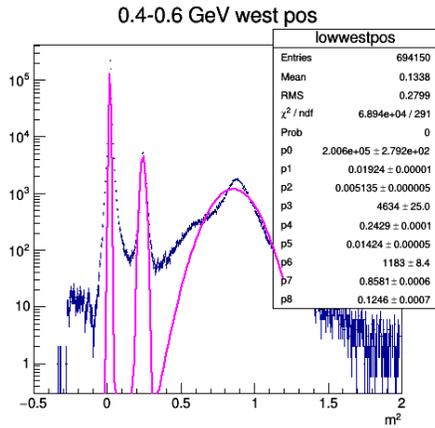
Figure 4.67: Positive charged particle mass-squared 1D distribution plot using the West arm before the DCA cut.

Figure 4.68: Positive charged particle mass-squared 1D distribution plot using the West arm after the DCA cut.
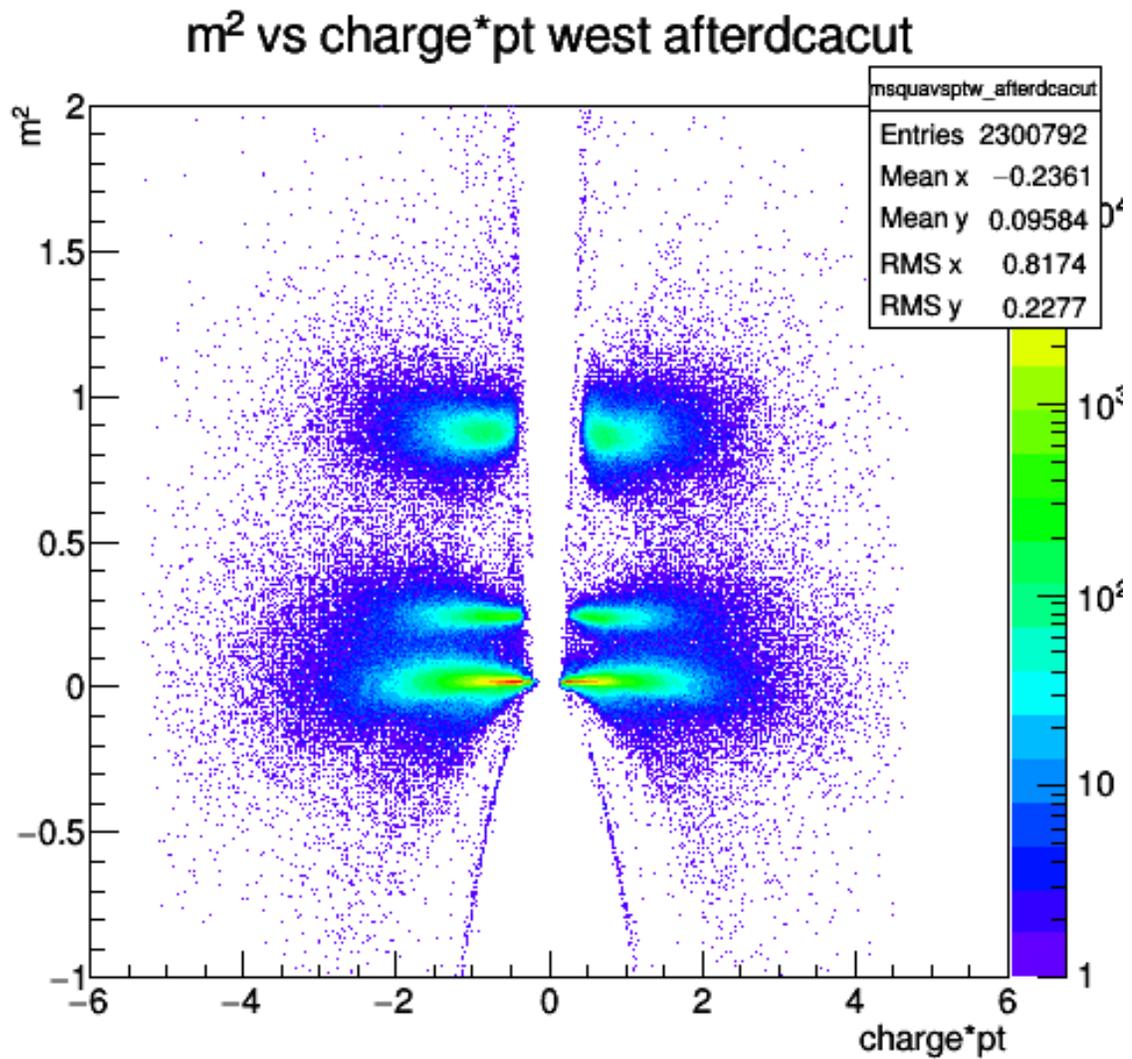
Figure 4.69: Charged particle mass-squared versus p_T 2D distribution plot after the DCA cut in real data.
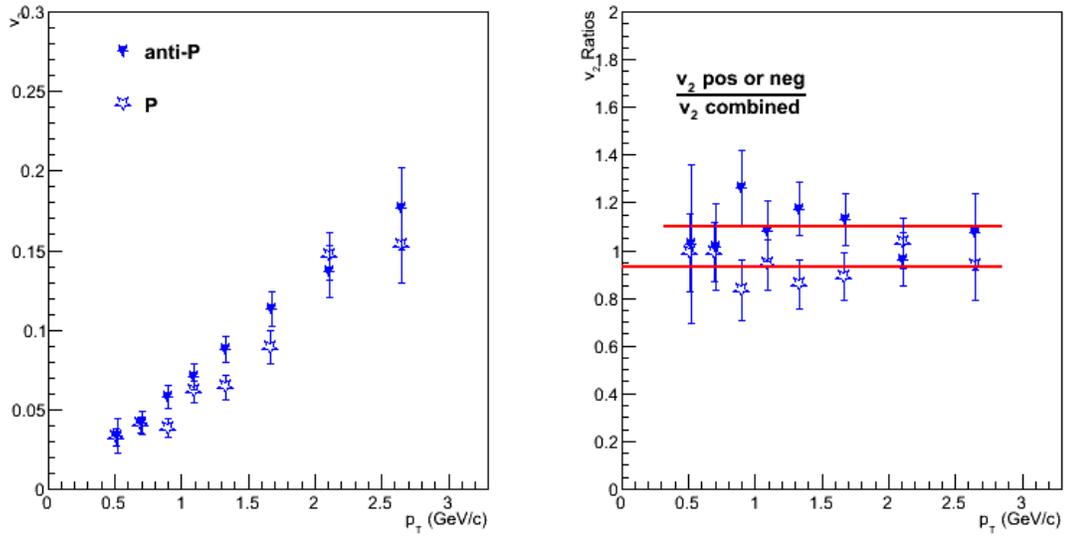
Figure 4.70: v_2 for proton and anti-proton before the DCA cut
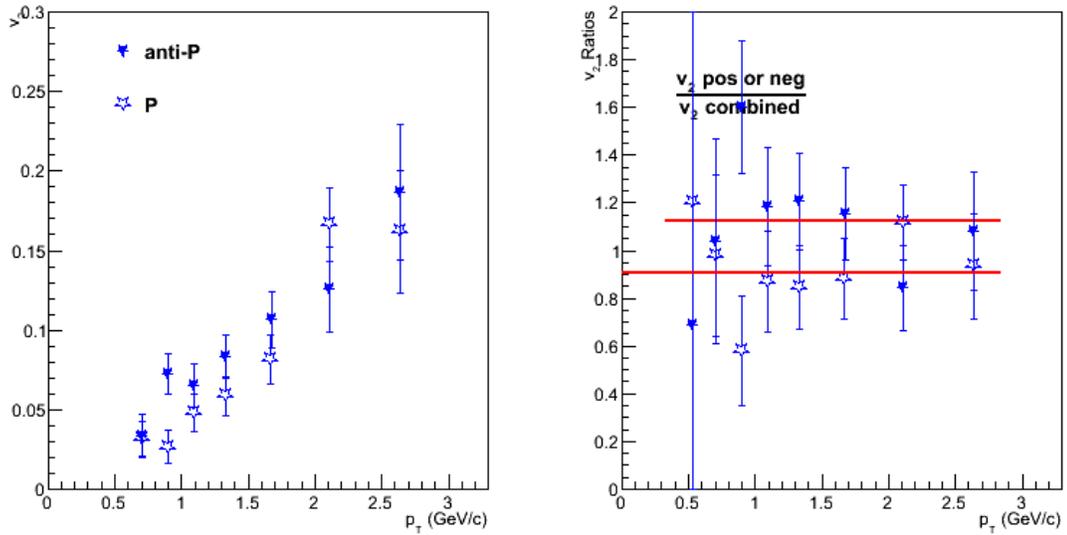
Figure 4.71: v_2 for proton and anti-proton after the DCA cut

the cut. This could be understood if the background protons have higher v_2 than the true protons.

In summary, the tracks are required to be within two standard deviations of the mean value of the DCA distribution. This additional selection is not applied at higher p_T nor for particle species for which the secondary-particle contamination is negligible. The pions and protons selected for the analysis are identified with purity of over 98% for p_T up to 3 GeV/c in all collision systems.

We used a DCA cut for particles with $p_T < 1$ GeV. The cut does not influence the v_2 results much above 1 GeV, but reduces the statistics- that is why we did not apply a DCA cut for $p_T > 1$ GeV/c.
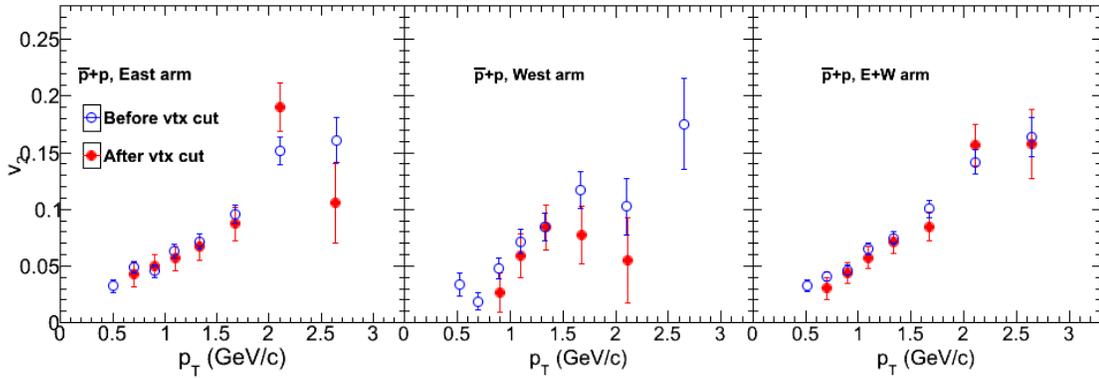
Figure 4.72: Measurement of v_2 for inclusive protons before and after DCA cut in pAu

4.6 Experimental Method for Flow Measurement

The real data collected from detectors contains the position, three-momentum of the final state particles, etc. Using the following experimental analysis techniques, we are able to extract the azimuthal anisotropy of the bulk system given we have enough statistical precision, thus, the collectivity of the system is implied [57].

4.6.1 Two-Particle Azimuthal Correlation

If all particles correlate with the common event plane in one event, they must correlate with each other. The two-particle correlation function is given by [58]:

$$C(\Delta\phi) = 1 + \sum_{n=1}^{\infty} 2c_n \cos(n\Delta\phi)$$

where $C(\Delta\phi)$ is the correlation function defined by the distribution of the differences between the azimuthal angle of two particles emitted in the same event, and the two-particle Fourier coefficients are related to the single-particle Fourier coefficients by $\sqrt{c_n} = v_n$. These are often referred to as flow harmonics, or flow coefficients. In real data analysis, because of the existence of local correlations and background noise, we need to select particles from two detectors for pairing and a background mixed correlation function is necessary to subtract the background contamination, in this circumstances, $c_n = v_{n,part1} * v_{n,part2}$.

Experimentally, Eq. 4.3 is used to extract correlation function. Here ϕ_{Track} is the azimuth of the track as it leaves the primary vertex, ϕ_{PMT} is the azimuth of the center of the PMT activated in the beam-beam counter; and we choose the weighting to be the total charge deposited in all PMTs. We construct the signal distribution $S(\Delta\phi, p_T)$ of track-PMT pairs over relative azimuthal opening angle $\Delta\phi = \phi_{Track} - \phi_{PMT}$, each with weight from the charge measured by each PMTs in BBC, in bins of track transverse momentum p_T. This method suffers from non-flow contributions and we need to take steps to separate now-flow effects from flow effects. We use particles from detectors which have a large separation in η so that the jet contribution and correlations from momentum conservation law are reduced. To correct for PHENIX's non-uniform azimuthal acceptance, we then construct the corresponding mixed-event distribution $M(\Delta\phi, p_T)$ over track-PMT pairs, where the tracks and PMT signals are from different events in the same centrality and vertex position class. Ten equally sized bins are used within the range of $|z| < 10$ cm in the event mixing. We then construct the normalized correlation function.

$$S(\Delta\phi, p_T) = \frac{d(w_{pmt} N_{sameevent}^{Track(p_T) - PMT})}{d\Delta\phi}$$

$$C(\Delta\phi, p_T) = \frac{S(\Delta\phi, p_T)}{M(\Delta\phi, p_T)} \frac{\int M(\Delta\phi', p_T) d\Delta\phi'}{\int S(\Delta\phi', p_T) d\Delta\phi'}$$

(4.3)

4.6.2 Extraction of c_n From the Two-particle Correlation Functions

We analyze the distributions by fitting each $C(\Delta\phi, p_T)$ to a four-term Fourier cosine expansion,

$$f(\Delta\phi) = 1 + \Sigma_{n=1}^{4} c_n(p_T) \cos(n\Delta\phi)$$

(4.4)

The sum function and each cosine component are plotted in Fig. 5.1 and Fig. 5.2 for each distribution. We observe that the $p + p$ distribution shape is described almost entirely by the dipole term $cos(\Delta\phi)$, which could be the product of di-jet fragmentation or other transverse-momentum-conserving processes.

4.6.3 Event Plane Method

As pictured in Fig. 2.1, the plane spanned by the collision impact parameter b and the direction of beam pipe z is called the Reaction Plane (RP), which varies event-by-event. It is not possible to directly access the RP orientation experimentally. We approximate it as an event plane, which is determined using all the produced particles, under the assumption that they flow collectively in response to pressure gradients in the initial geometry. However, since in reality the multiplicity of the final-state particles is finite, plus the detectors have limited resolution, there may be a shift between the reaction plane and the event plane orientation. Hence, we define a correction factor called the "event plane resolution" to correct for this effect. The calculation of the event plane orientation starts with flow vectors, Q:

$$Q_x = \Sigma_{i=1}^{N} w_i \cos(n\phi_i)$$

$$Q_y = \Sigma_{i=1}^{N} w_i \sin(n\phi_i) \qquad (4.5)$$

$$\Psi_n = atan(Q_y/Q_x)$$

where the N is number of PMT hits in the BBC south, the weight factor of is the charge deposited in each of the PMTs. The ϕ_i is the ϕ angle of the center position of each PMT and the Ψ_n is the n_{th} harmonic event plane angle. The event-plane determination is also subject to non-flow effects, so we usually utilize a large η separation between the particles of interest and the particles used to determine the event-plane angle. A standard event-plane flattening technique has been applied to remove the residual non-uniformities in the distribution of event-plane angles. The v_n from the event plane methods is extracted by:

$$v_n = \frac{< \cos(n(\phi - \Psi_{n,BBC_{south}})) >}{Res(\Psi_{n,BBC_{south}})} \qquad (4.6)$$

A three sub-events methods is used to determine the resolution of the second-order event plane measured by the BBC south or FVXT south by interchanging those detectors as shown below. For example the $\Psi_{n,BBC_{south}}$ can be expressed as Equation 4.7:

$$Res(\Psi_{n,BBC_{south}}) = < \cos(n(\Psi_{n,BBC_{south}} - \Psi_{RP})) > =$$
$$\sqrt{\frac{< \cos(n(\Psi_{n,BBC_{south}} - \Psi_{n,CNT})) >< \cos(n(\Psi_{n,BBC_{south}} - \Psi_{n,FVTX_s})) >}{< \cos(n(\Psi_{n,CNT} - \Psi_{n,FVTX_s})) >}} \qquad (4.7)$$

where, the $\Psi_{n,CNT}$ is the nth order event plane measured with low p_T (0.2 GeV/c $< p_T <$ 2.0 GeV/c) tracks from DC to avoid the jet contribution. And the $\Psi_{n,FVTXs}$ is the nth order event plane measured with forward silicon vertex detector, FVTX, located in the Au-going direction. We use the FVTX south in the analysis as the main results. Alternatively, the BBC south can be used to determine the event plane in a combination with the central

tracks and the FVTX.

The value of the second-order event-plane resolution for BBC south is 0.062, while for FVTX south it is 0.171, which illustrates why we chose FVTX for the main result. In the case of the third-order event plane direction, $\Psi_{3,obs}$ is determined using the BBC south. The resolution number for the third order BBC south event plane is 0.067±0.009, while the resolution for the FVTX south event plane is 0.024. FVTX clusters have a larger proportion of noise signals than the BBC PMTs, and since the v_3 signal is quite small and sensitive to noise the FVTX resolution for v_3 is significantly affected.

4.7 Non-flow Estimation

4.7.1 Non-flow Estimate Based on a Comparison With Minimum Bias $p+p$ Collisions

Some portion of the correlation strength c_n in the p+Au data could be due to elementary processes such as di-jet fragmentation (mainly from away side) and resonance decays. We can estimate the effect of such processes under the assumptions that (i) all correlations present in minimum bias $p+p$ collisions are due to elementary processes, and (ii) those same processes occur in the measured p+Au system as a simple superposition of several nucleon-nucleon collisions. In this case, we would expect the contribution from elementary processes to be equal to the $c_n^{p+p}(p_T)$ but diluted by the increase in particle multiplicity between $p+p$ and p+Au, if the number of elementary processes is proportional to the multiplicity of the other particles used in pair correlations. We estimate the ratio of the $p+p$ to p+Au general multiplicities by measuring the ratio of the total charge seen in the BBC-S in $p+p$ versus p+Au events, which we find to be approximately 5.03/58.9 and only weakly dependent on the track p_T. We can then separate $c_n^{p+\mathrm{Au}}(p_T)$ into elementary and

non-elementary components:

$$c_n^{p+\text{Au}}(p_T) = c_n^{Nonelem.}(p_T) + c_n^{Elem.}(p_T) \approx$$

$$c_n^{Nonelem.}(p_T) + c_n^{p+p}(p_T) \frac{\Sigma Charge^{p+p}}{\Sigma Charge^{p+\text{Au}}} \tag{4.8}$$

Fig. 4.73 and Fig. 4.74 show the values of c_n in high-multiplicity p+Au and $p+p$ collisions and the estimation of second and third order non-flow based on the their ratios.
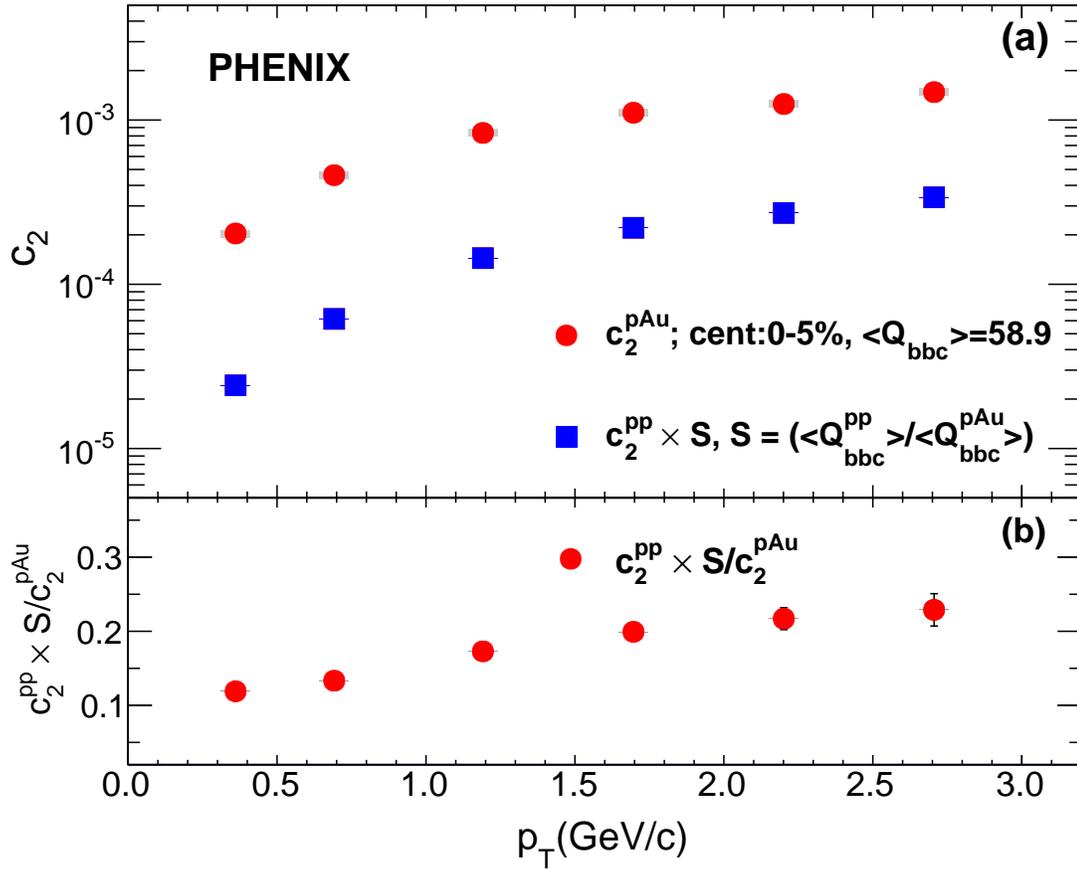
Figure 4.73: Second order coefficient c_2 from Fourier fitting to correlation functions comparison of 0-5% p+Au to minimum bias $p+p$ collisions. The ratio estimates the non-flow contribution.
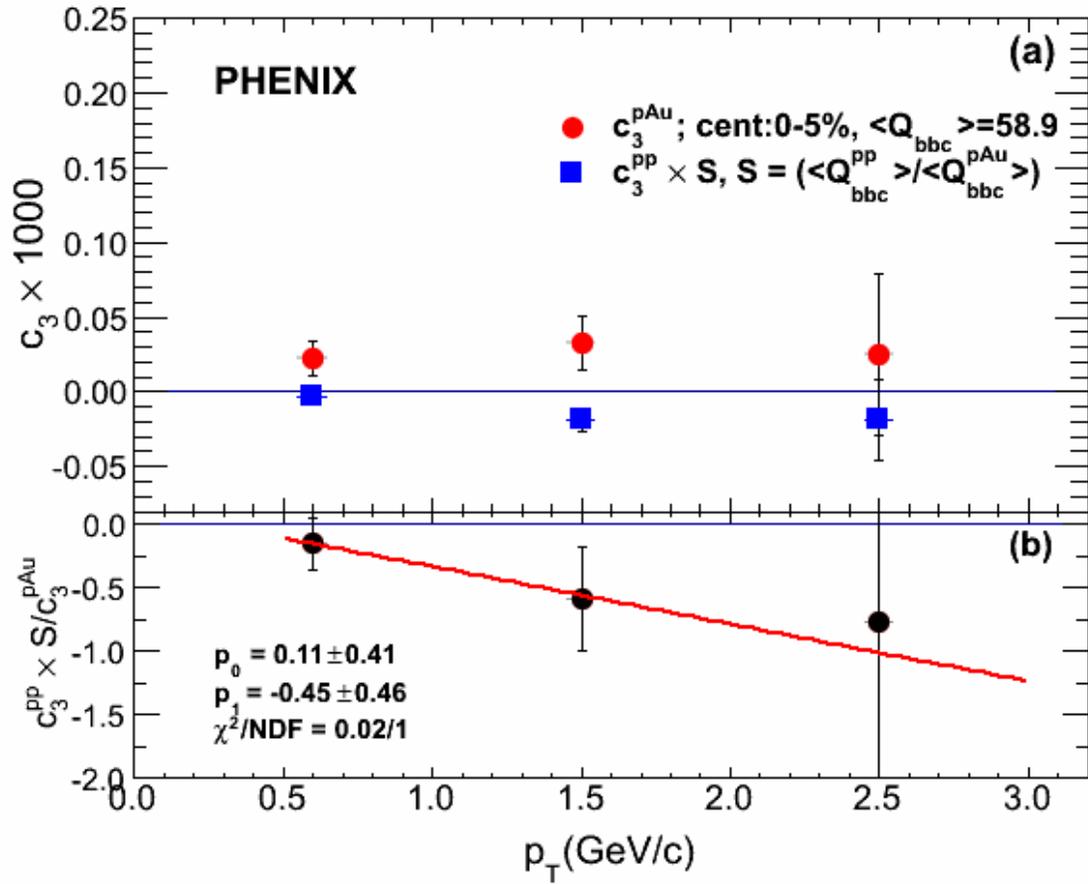
Figure 4.74: Third order coefficient c_3 from Fourier fitting to correlation functions comparison of 0-5% p+Au to minimum bias $p + p$ collisions. The ratio estimates the non-flow contribution.

4.7.2 Monte-Carlo Verification

To demonstrate our method using c_2 in minimum bias $p + p$ collision to estimate the non-flow fraction in central p+Au collisions is valid, we test this method in HIJING simulation, which has no hydrodynamic flow input but contains jets and jet-like short-range correlations. We would expect a non-zero c_2 in p+Au even there is no flow presented. We compare the c_2 yield in central p+Au collisions and the scaled c_2 in $p + p$ collisions, and we find that elementary process in $p + p$ scaled by a dilution factor is a good representation of non-flow in central collisions in real data. In the v_2 measurement, we include the non-flow as one dominant source of systematic uncertainties.

Similar to the analysis step we did on real data in p+Au and $p + p$ collisions, we generated several hundred millions p+Au and $p + p$ events and calculated the correlation functions between mid-rapidity and forward rapidity. The centrality in p+Au is defined using the percentile in the number of charged particles produced in the forward pseudorapidity range of $-4 < |\eta| < -3$. The results are plotted as a function of p_T and centrality.
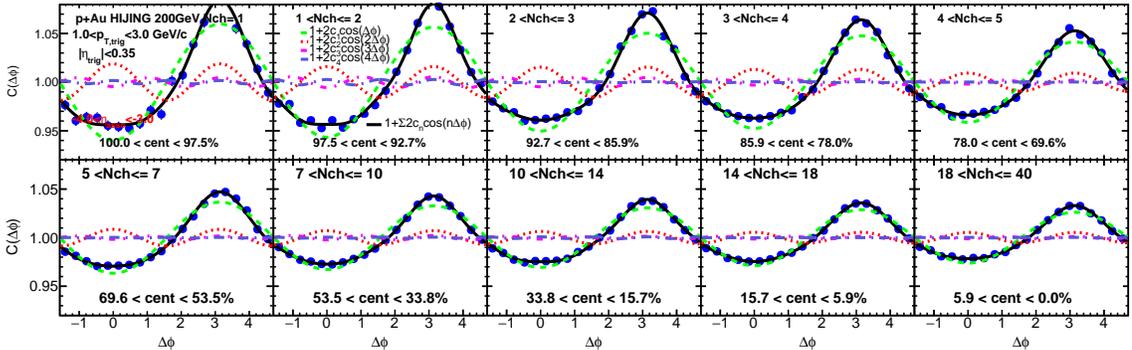
Figure 4.75: The azimuthal correlation functions $C(\Delta\phi, p_T)$, as defined in Eq. 4.3 , for charged-particle pairs with different centrality selections in $1.0 < p_T < 3.0$ (GeV/c) from p+Au collisions at $\sqrt{s_{NN}} = 200$ GeV in a HIJING simulation. The pairs are formed between charged tracks measured in $|\eta| < 0.35$ and $-4 < \eta < -3$. Each correlation function is fit with a four-term Fourier cosine expansion; the individual components n = 1 to n = 4 are drawn in each panel, together with the fit function sum.

Also we also plotted correction functions in $p + p$ collisions in Fig. 4.77, which will be used as a baseline estimation.
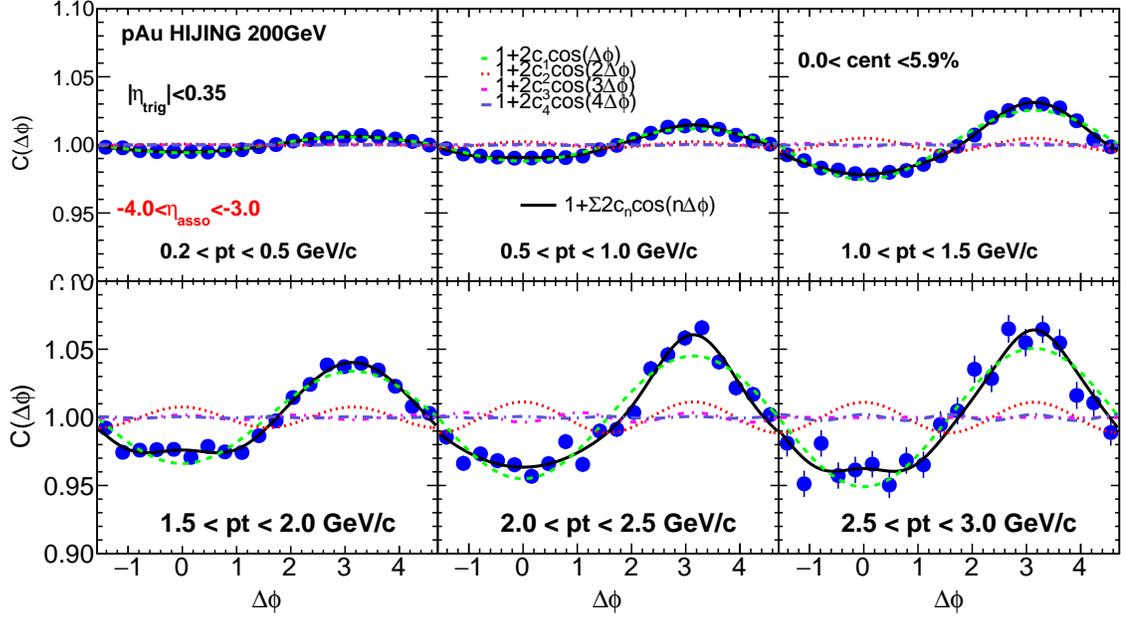
Figure 4.76: The azimuthal correlation functions $C(\Delta\phi, p_T)$, as defined in Eq. 4.3 , for charged particle pairs with different p_T selections in 0-5% central p+Au collisions at $\sqrt{s_{NN}}$= 200 GeV in HIJING simulation. The pairs are formed between charged tracks measured in $|\eta| < 0.35$ and $-4 < \eta < -3$. Each correlation function is fit with a four-term Fourier cosine expansion; the individual components n = 1 to n = 4 are drawn in each panel, together with the fit function sum.
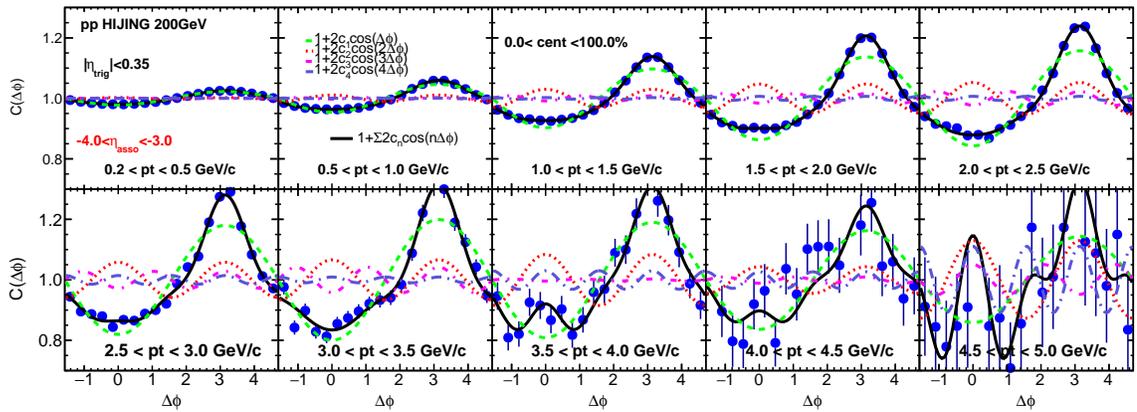
Figure 4.77: The azimuthal correlation functions $C(\Delta\phi, p_T)$, as defined in Eq. 4.3 , for charged particle pairs with different p_T selections in 0-5% central p+Au collisions at $\sqrt{s_{NN}}$= 200 GeV in HIJING simulation. The pairs are formed between charged tracks measured in $|\eta| < 0.35$ and $-4 < \eta < -3$. Each correlation function is fit with a four-term Fourier cosine expansion; the individual components n = 1 to n = 4 are drawn on each panel,together with the fit function sum.

4.7.3 Subtraction Methods

Using Hijing simulation results, we can quantify how well our subtraction method works. Two methods are shown in Fig. 4.78 and the difference between them is how we define the scale factor. The result clearly demonstrate that at the p_T range 0.5 to 3 GeV/c, multiplicity dilution factor works better than the c_1 factor. We choose multiplicity factor as our final non-flow estimation method.
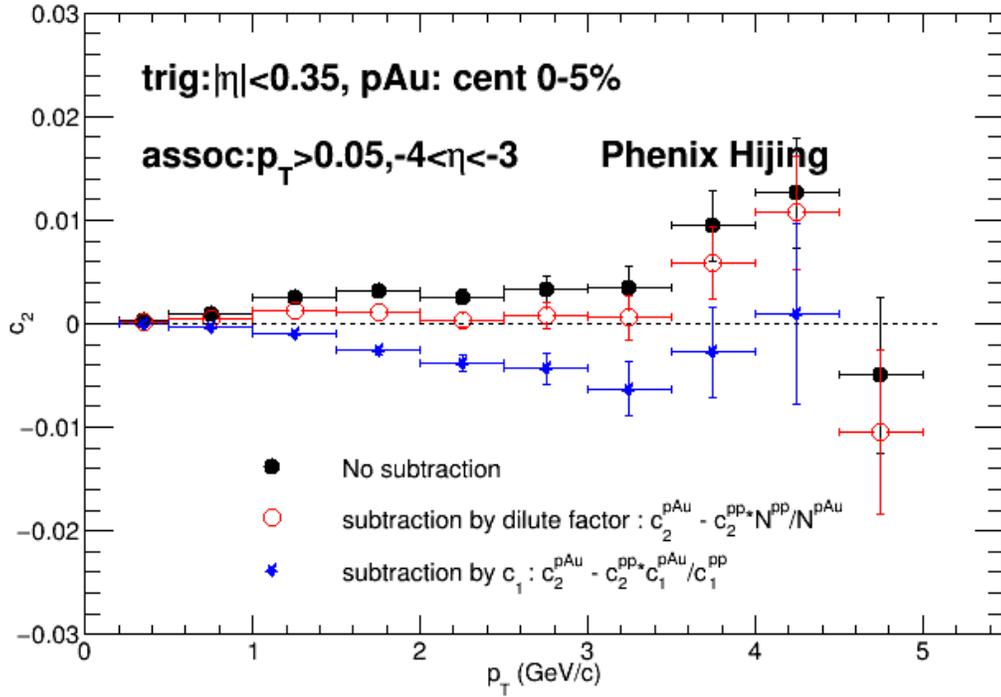
Figure 4.78: The c_2 as a function of p_T, in central p+Au Monte-Carlo simulations, subtracted by different definition of dilution factor times the c_2 of $p + p$ minbias in Hijing.

4.7.4 Data-driven 3-subevent Method Cross Check

The 3-subevent method can estimate the v_2 directly. We constructed 3 types of correlation functions in the same events and fit with Fourier functions to get three types of c_2: $c_{2,CNT-BBCsouth}$, $c_{2,CNT-FVTXsouth}$, $c_{2,BBCsouth-FVTXsouth}$, the BBC south means the PMTs

in BBC south side and FVTX south means the FVTX reconstructed tracks in south side. Then

$$v_{2,cnt} = \sqrt{\frac{c_{2,CNT-BBCsouth} * c_{2,CNT-FVTXsouth}}{c_{2,BBCsouth-FVTXsouth}}} \qquad (4.9)$$

Notice all the c_2s include the non-flow contribution so we again use minbias $p+p$ collisions to subtracted the non-flow part and re-estimate the v_2 directly. Fig. 4.79 shows our default non-flow estimation has a very good agreement with the data-driven 3-subevent method.
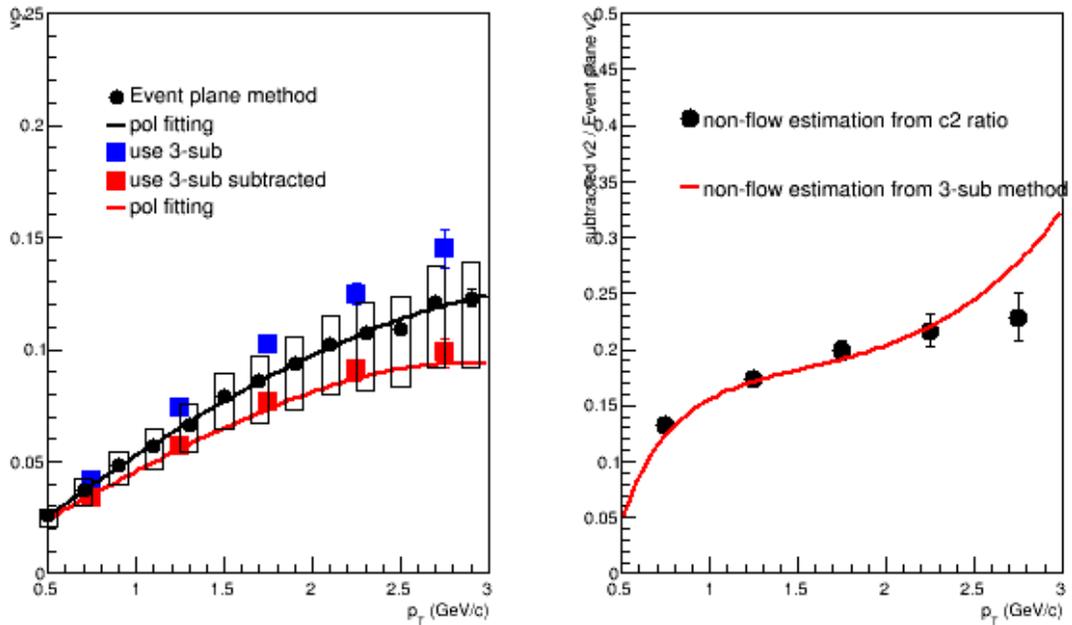
Figure 4.79: Left panel:The measured v_2 vs p_T comparison between event plane method, 3-subevent method before subtraction and 3-subevent method after subtraction. Right panel: non-flow estimation cross check between c_2 method and 3-subevent method.

4.8   Systematics Uncertainties

4.8.1   Systematic Uncertainties in c_2 from PC3 Matching

We vary the PC3 matching criteria from $\sigma = 3$ to $\sigma = 2$. The c_2 systematic uncertainty from PC3 matching is less than 5% as shown in Fig. 4.80. We cite it as 3%.
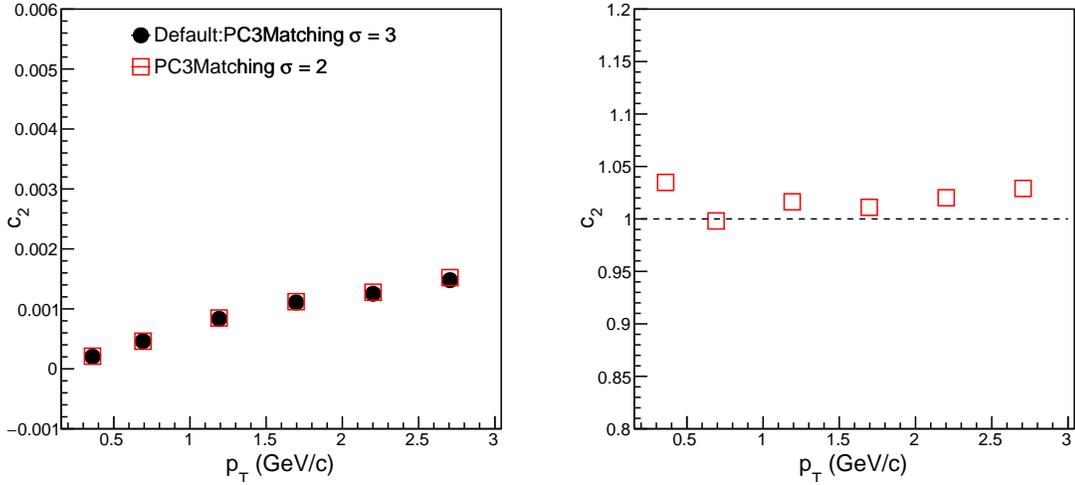
Figure 4.80: Measurement of c_2 systematic uncertainty by varying the PC3 matching cut.

4.8.2   Systematic Uncertainties in c_2 from Pile-Up

We cite the difference from high luminosity (rate>150kHz) and from low luminosity (rate<150kHz) as the systematic uncertainties for pile-up events. We give 4% for the pile-up systematics in top 0-5% events c_2, as shown in Fig.4.81.

4.8.3   Systematic Uncertainties in v_2 from PC3 Matching

PC3 matching cut is also a systematic source for v_2 determination. Fig. 4.82 shows the v_2 change by varying PC3 cut from 3σ to 2σ. This effect is very small and we cite 1% as the systematic uncertainties in $p_T < 2.0$ GeV/c and 2% in $p_T > 2.0$ GeV/c.
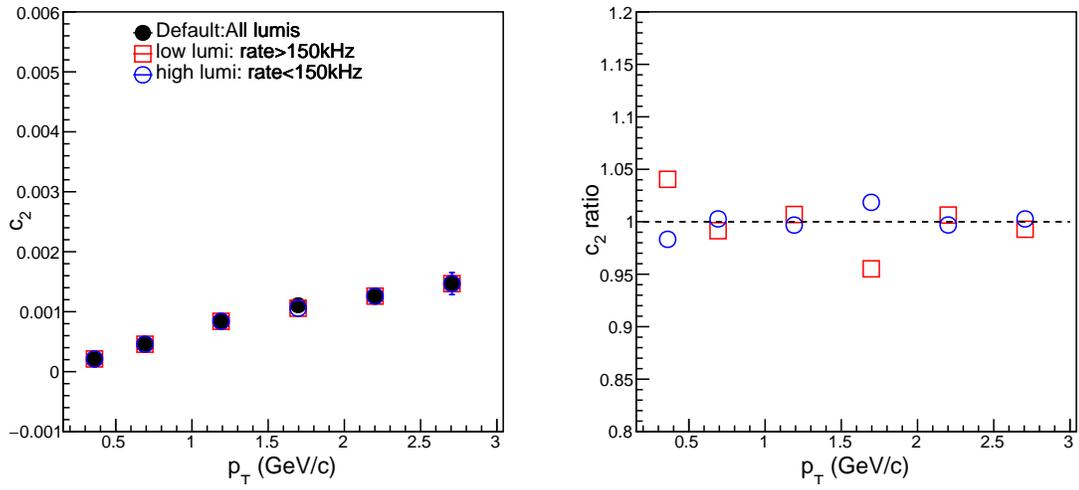
Figure 4.81: Measurement of c_2 systematic uncertainties by analysis on high luminosity events and low luminosity events.
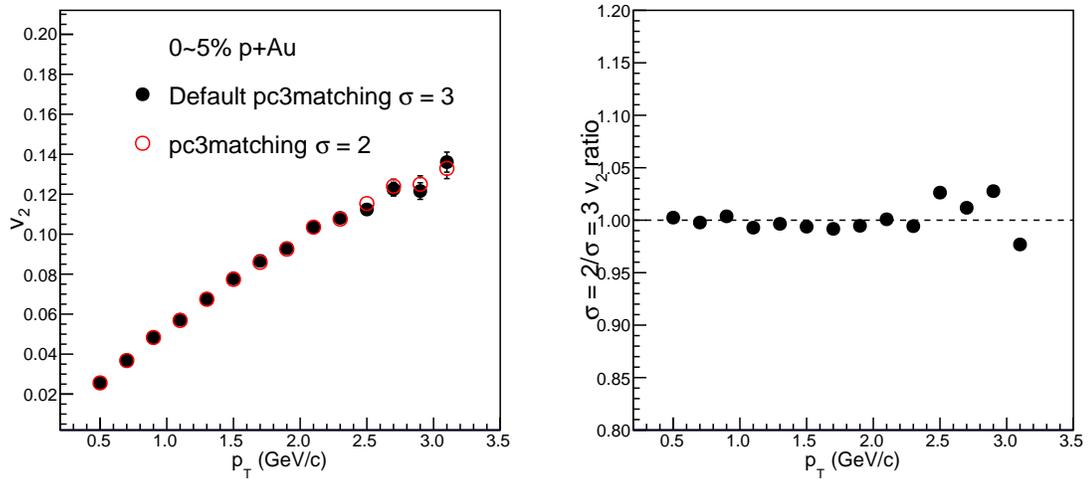
Figure 4.82: Measurement of v_2 systematic uncertainties by varying the PC3 matching cut.

4.8.4 Systematic Uncertainties in v_2 from Pile-Up

We cite the difference from high luminosity (rate$>$150kHz) and from low luminosity (rate$<$150kHz) as the systematic uncertainties for pile-up events.

By model calculation, the pile-up events in central p+Au collision are around 8%. To study the effect of pile-up, we also measure the v_2 in the high luminosity event in which the pile up is around 17%. The v_2 difference between the high luminosity events and inclusive event is less than 2%, We assign 4% systematic uncertainty in top 0-5% events to account for this 8% pile-up. as shown in Fig. 4.83.
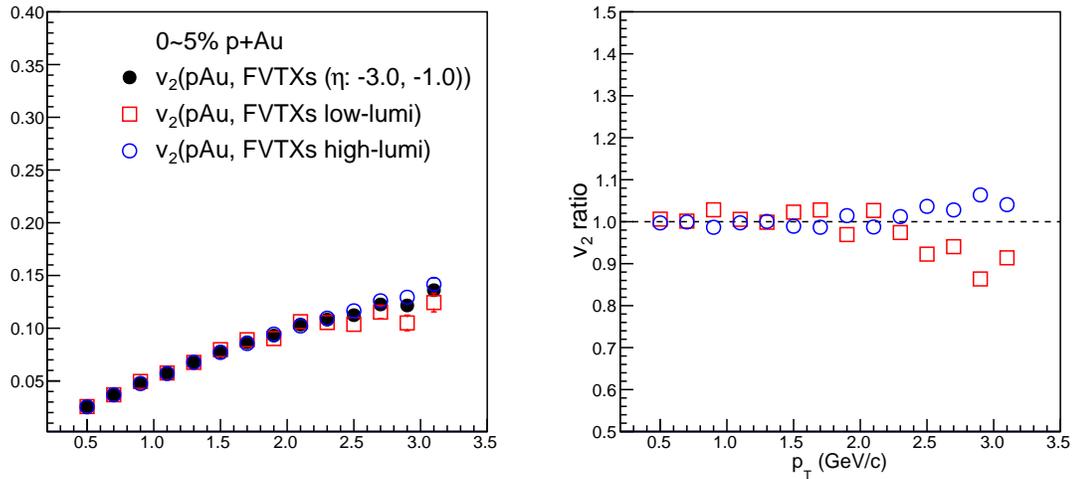
Figure 4.83: Measurement of v_2 systematic uncertainty by analysis on high luminosity events and low luminosity events.

4.8.5 Systematic Uncertainties in v_2 Using Event Plane Method from Different Detectors

We can calculate v_2 from different event plane angles, which come from various detectors, here we use v_2 from FVTX south detector as main results. Other detectors results are here for systematic uncertainty sources. We cite 3% as the systematic uncertainty.
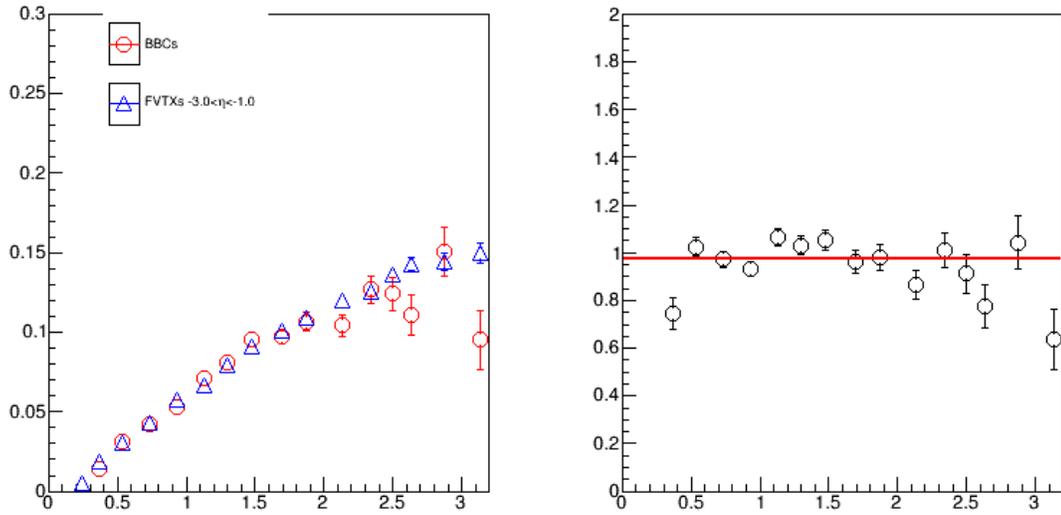
Figure 4.84: Measurement of v_2 systematic uncertainty results from different event planes.

4.8.6 Systematic Uncertainties in v_2 Using East/West Drift Chamber

We assume that the true v_2 lies in between the east arm v_2 and the west arm v_2 and has a flat distribution. The systematic uncertainties are estimated by the (upper limit - lower limit)/$\sqrt{(12)}$, which is $(12\% + 7\%)/\sqrt{(12)} = 5\%$

4.8.7 Systematic Uncertainties Table for v_2

Table 4.2 gives the table for systematic uncertainties.

4.8.8 Systematic Uncertainties in v_3 from track matching

The fake tracks are rejected by DC central PC3 matching in both ϕ and z direction. The default cut is 2 σ. We vary the cut values to a looser cut of 3 σ. This change is done both for the tracks used in the v_3 measurement and for the tracks used in the CNT event plane determination, which in turn enters the determination of the event plane resolution. This uncertainty is, therefore, a convolution between the uncertainty from background tracks
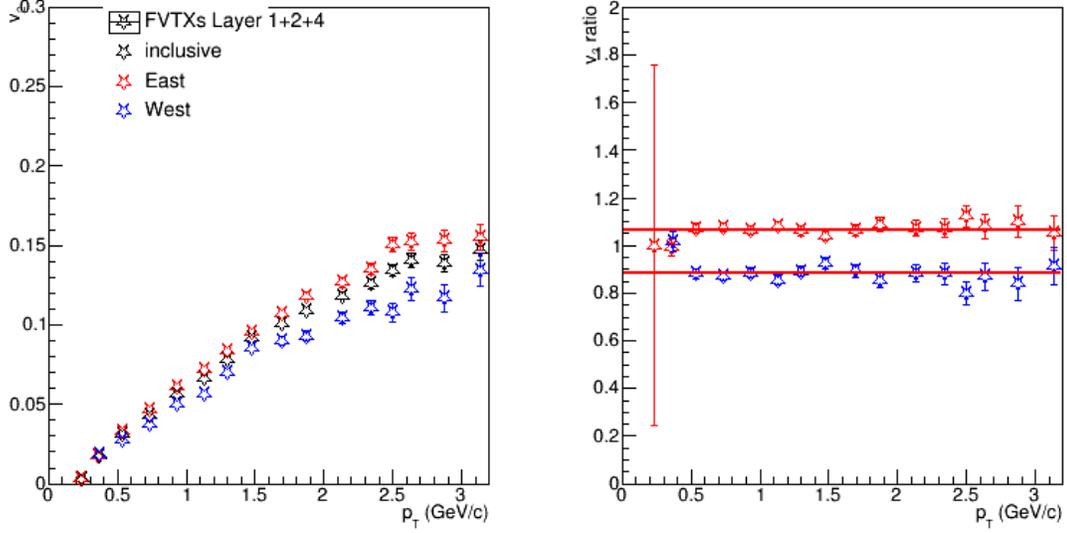
Figure 4.85: Measurement of v_2 systematic uncertainty results from east/west difference

source	track matching	pile-up	non-flow	EP de-tector	e/w diff	total
up	1 ($p_T < 2$) 2 ($p_T > 2$)	4	0	3	5	7.1 ($p_T < 2$) 7.3 ($p_T > 2$)
down	1 ($p_T < 2$) 2 ($p_T > 2$)	0	12.0 ($0 < p_T < 0.5$) 13.3 ($0.5 < p_T < 1.0$) 17.3 ($1.0 < p_T < 1.5$) 19.9 ($1.5 < p_T < 2.0$) 21.7 ($2.0 < p_T < 2.5$) 22.9 ($2.5 < p_T < 3.0$)	3	5	13.4 ($0 < p_T < 0.5$) 14.6 ($0.5 < p_T < 1.0$) 18.3 ($1.0 < p_T < 1.5$) 20.8 ($1.5 < p_T < 2.0$) 22.6 ($2.0 < p_T < 2.5$) 23.7 ($2.5 < p_T < 3.0$)

Table 4.2: Systematic Uncertainties table for unidentified $v_2(p_T)$

and the uncertainty in the event plane resolution. There are two competing effects. The event plane resolution improves with the inclusion of more real tracks, but the background tracks that enter the3 σ track selection will dilute the signal. The ratio between the result with 3σ and 2σ cut is shown in Fig. 4.86. In this ratio plot, since the numerator and the denominator are fully correlated, the error bars for the ratio σ_r is calculated taking into account the covariance:

$$\sigma_r = \frac{E_A}{E_B} * \sqrt{\frac{\sigma_A^2}{E_A^2} + \frac{\sigma_B^2}{E_B^2} - \frac{2}{E_A E_B} \sigma_A^2}$$

where $r = \frac{A}{B}$ and E_A, E_B are the values of physics quantity A and B, and σ_A, σ_B are the statistics errors of A and B correspondingly.

The total uncertainty from this source is of the order 1% and is type B. The part that changes the event plane resolution is a scale uncertainty that moves all the points together;

4.8.9 Systematics Uncertainties in v_3 from Pile-Up Rejection

As stated in the previous section, we use the pile-up filter using BBC south time with time window 0.5 ns: $fraction < 0.9$. Comparing the v_3 with a looser pile-up filter $fraction < 0.95$. The systematic uncertainty is estimated to be 3%.

4.8.10 Systematics Uncertainties in Third-Order Event Plane Resolution

Since Central arm tracks are used to determine the event plane resolution for BBCs, the way we select the p_T range of the tracks makes the results different. The default p_T range is from 0.4 to 2 GeV/c as this is the best tracking performance range. Changing it to a broader range 0.2 GeV to 3 GeV/c may result in more background tracks, the resolution calculated is 0.062. The systematic uncertainty is estimated to be (0.067 - 0.062) / 0.067 = 7%.
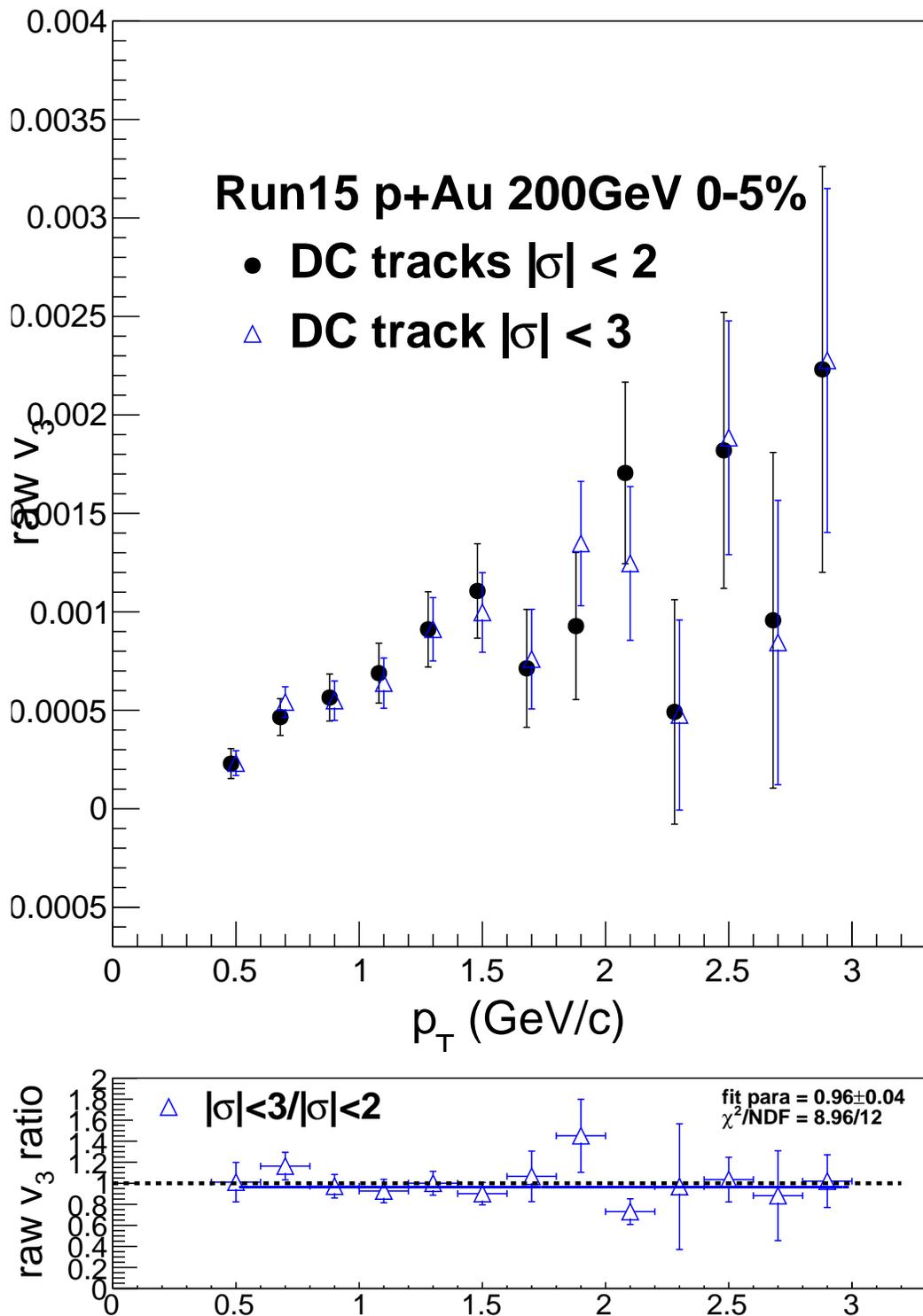
Figure 4.86: Measurement of v_3 systematic resulting from track matching. This is raw v_3 excluding the effect of the change of event plane resolution. The horizontal bars are bin widths.
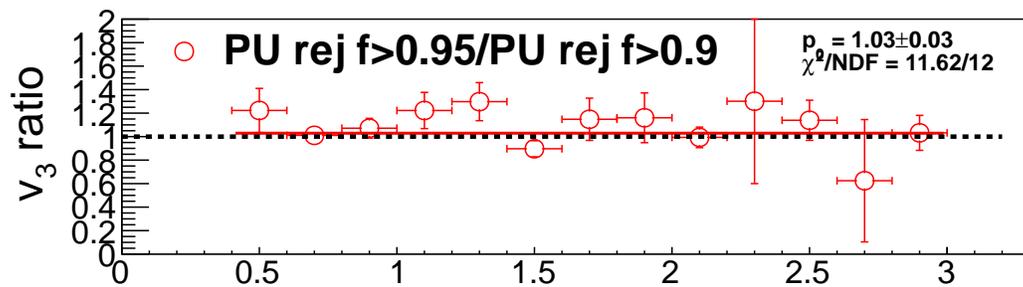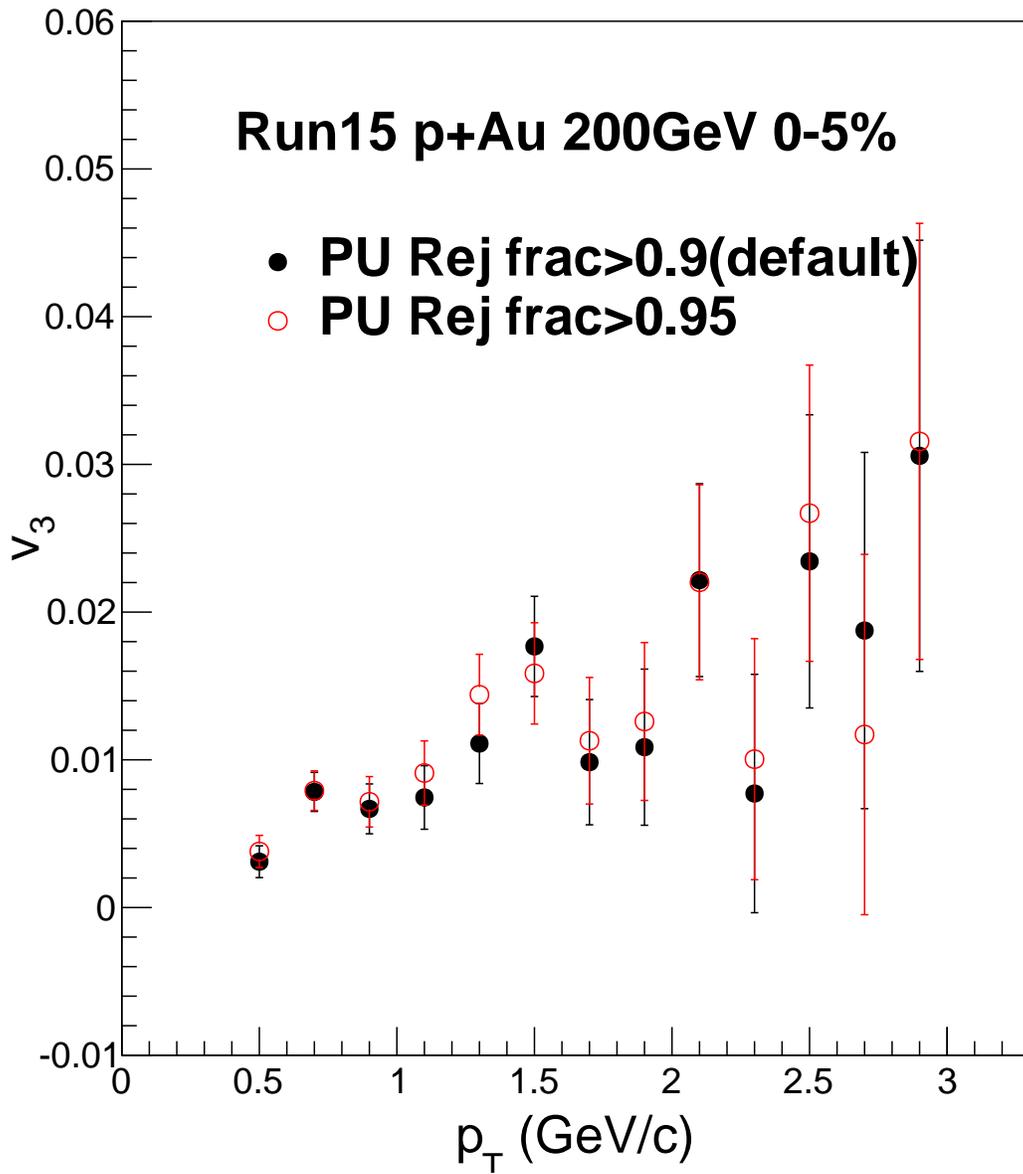
Figure 4.87: Measurement of v_3 systematic results from event pile-up study.

4.8.11 Systematics Uncertainties in v_3 Using the Event Plane Method with Different Detectors

The third-order event plane angle, ψ_3 can be calculated using different event plane detectors. This in turn yields different v_3 results. Here we use v_3 from the BBCs detector as the main results and use the results from other detectors as a calculation of the systematic uncertainty. We cite 13%. as the systematic uncertainty.

4.8.12 Systematics Uncertainties in v_3 Using East/West Drift Chamber

We assume that the true v_3 lies in between the east arm v_3 and the west arm v_3 and has a flat distribution. Based on Fig.4.88, the ratio east/inclusive is 20%, and west/inclusive is 15%. We therefore assign 11% type B for the systematic uncertainty because of detector misalignments.

$$(upperlimit - lowerlimit)/\sqrt{(12)} \tag{4.10}$$

4.8.13 Summary of Systematic Uncertainties for v_3

All assigned systematic uncertainties are summarized in Tab. 4.3. The systematic uncertainties are assigned types where

Type A: point-to-point uncorrelated;

Type B: point-to-point correlated;

Type C: global scale uncertainties.

4.8.14 Systematics Uncertainties in Identified Particle v_2

The systematic uncertainties in the PID v_2 measurement can be broadly characterized according to the following categories: 1) event-plane as measured using different detectors;
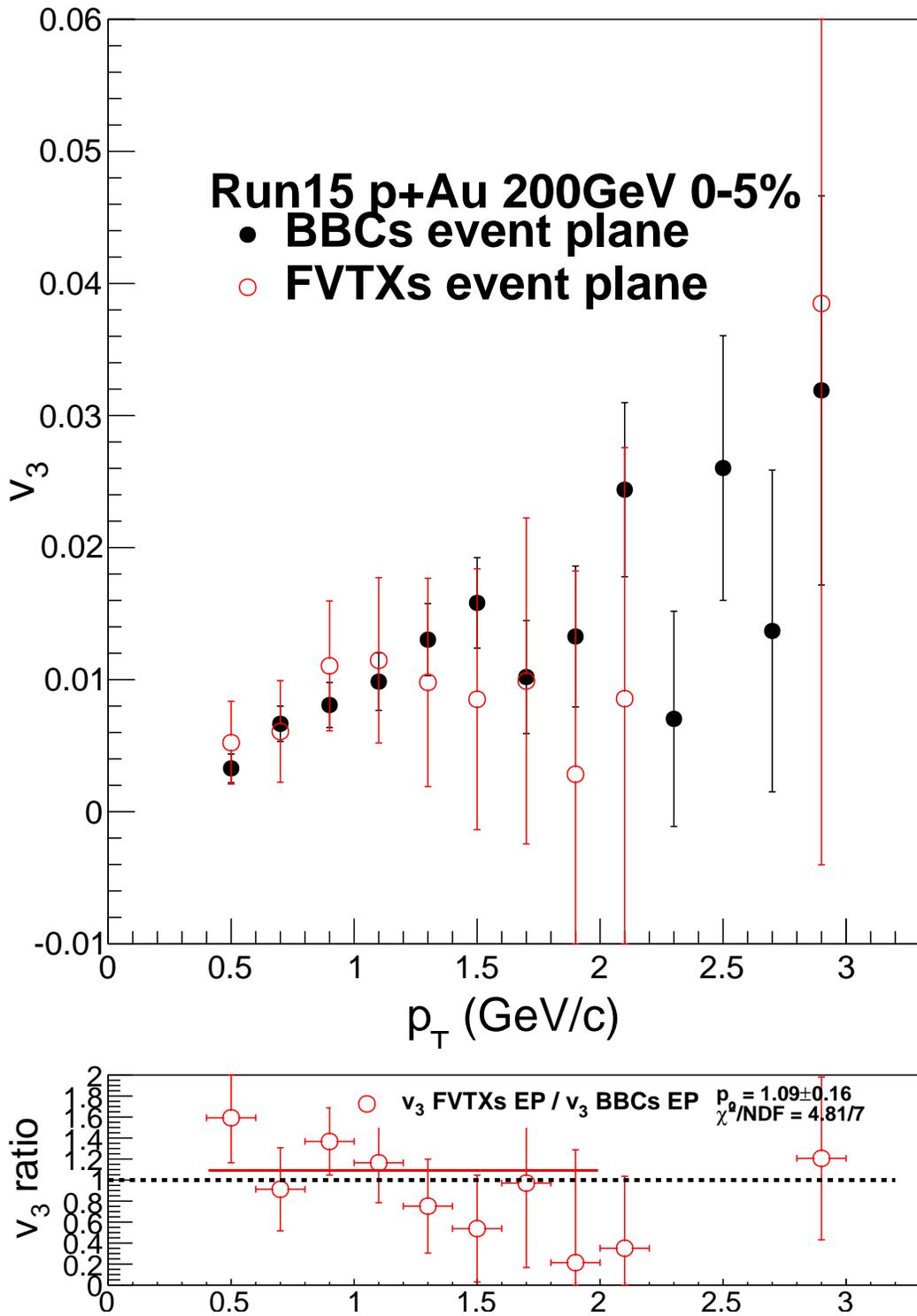
Figure 4.88: Measurement of v_3 systematic results from different event planes. Here shows the p_T differential result.
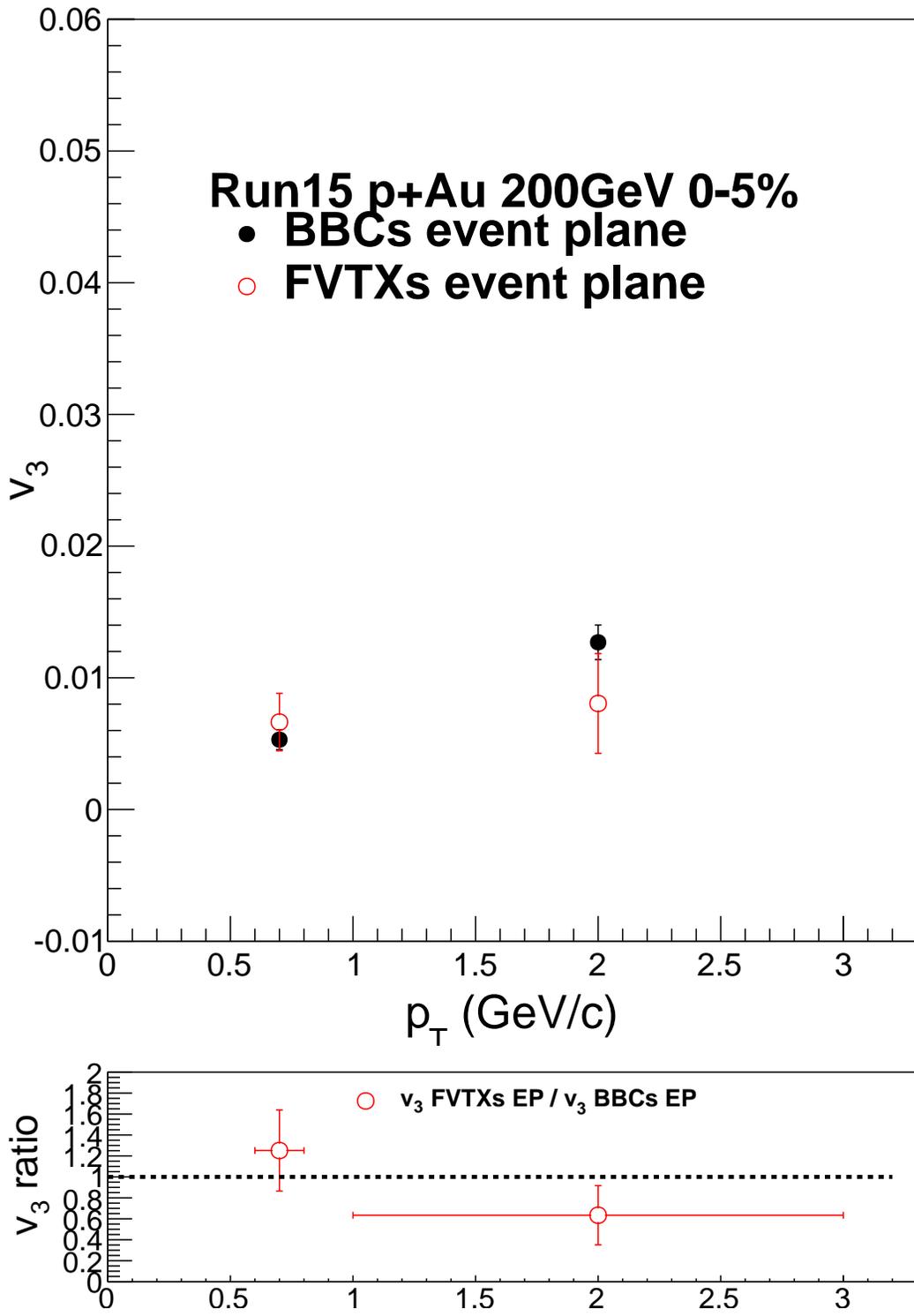
Figure 4.89: Measurement of v_3 systematic results from east/west difference. Here shows the integrated results over p_T ranged from 0.4-1 GeV/c and 1-3GeV/c.
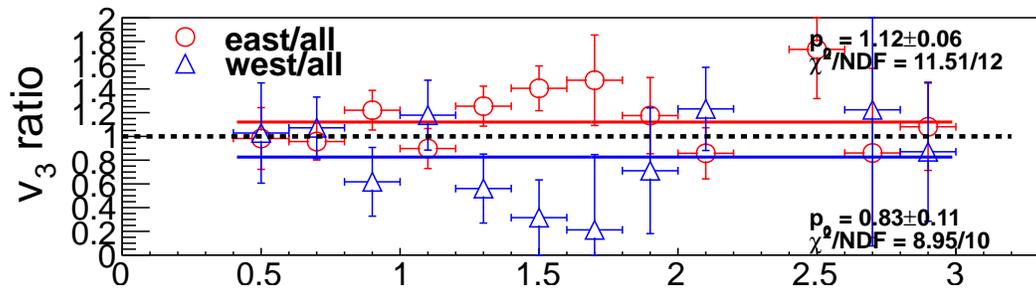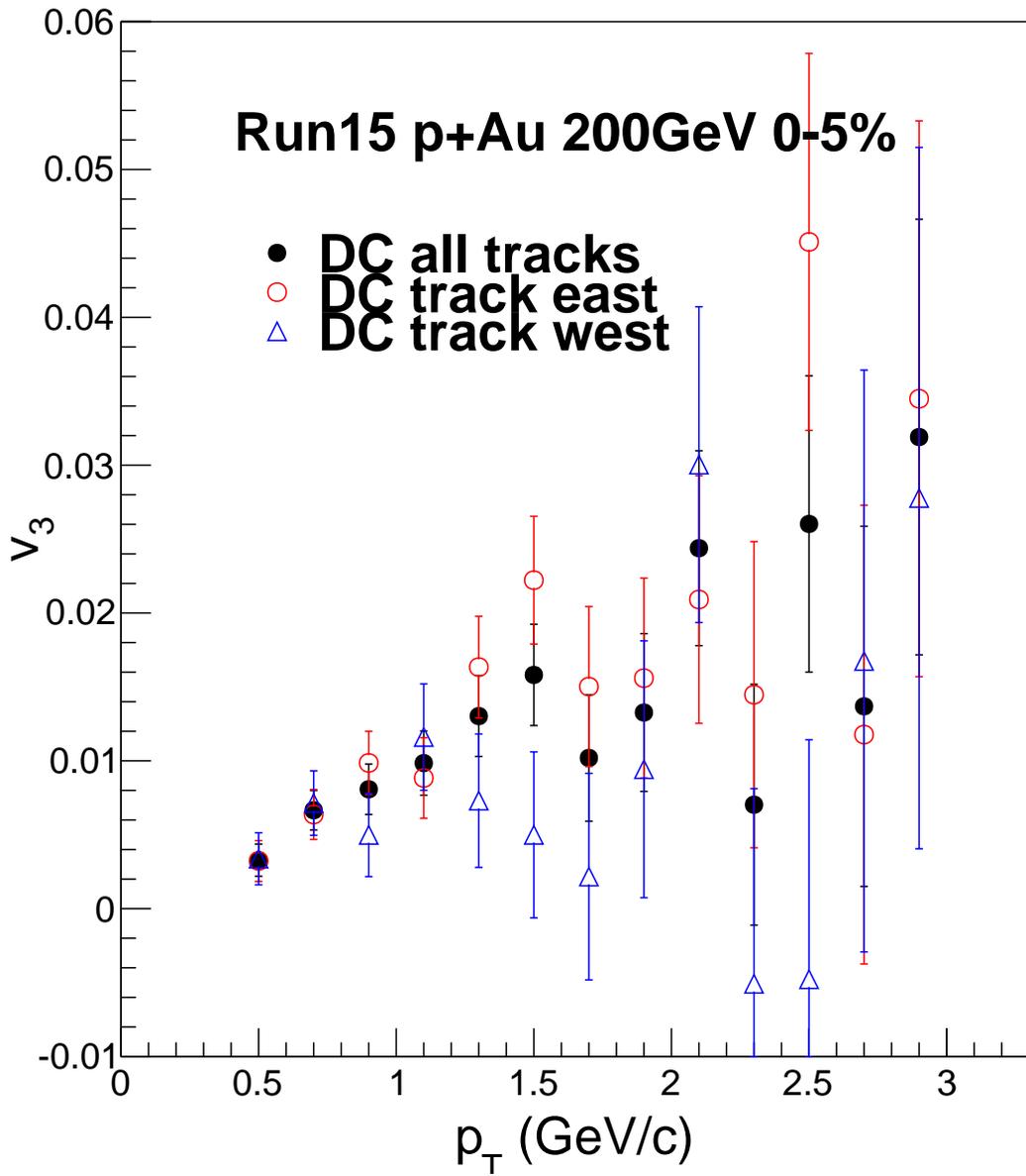
Figure 4.90: Measurement of v_3 systematic results from east/west difference. Here shows the p_T differential result.
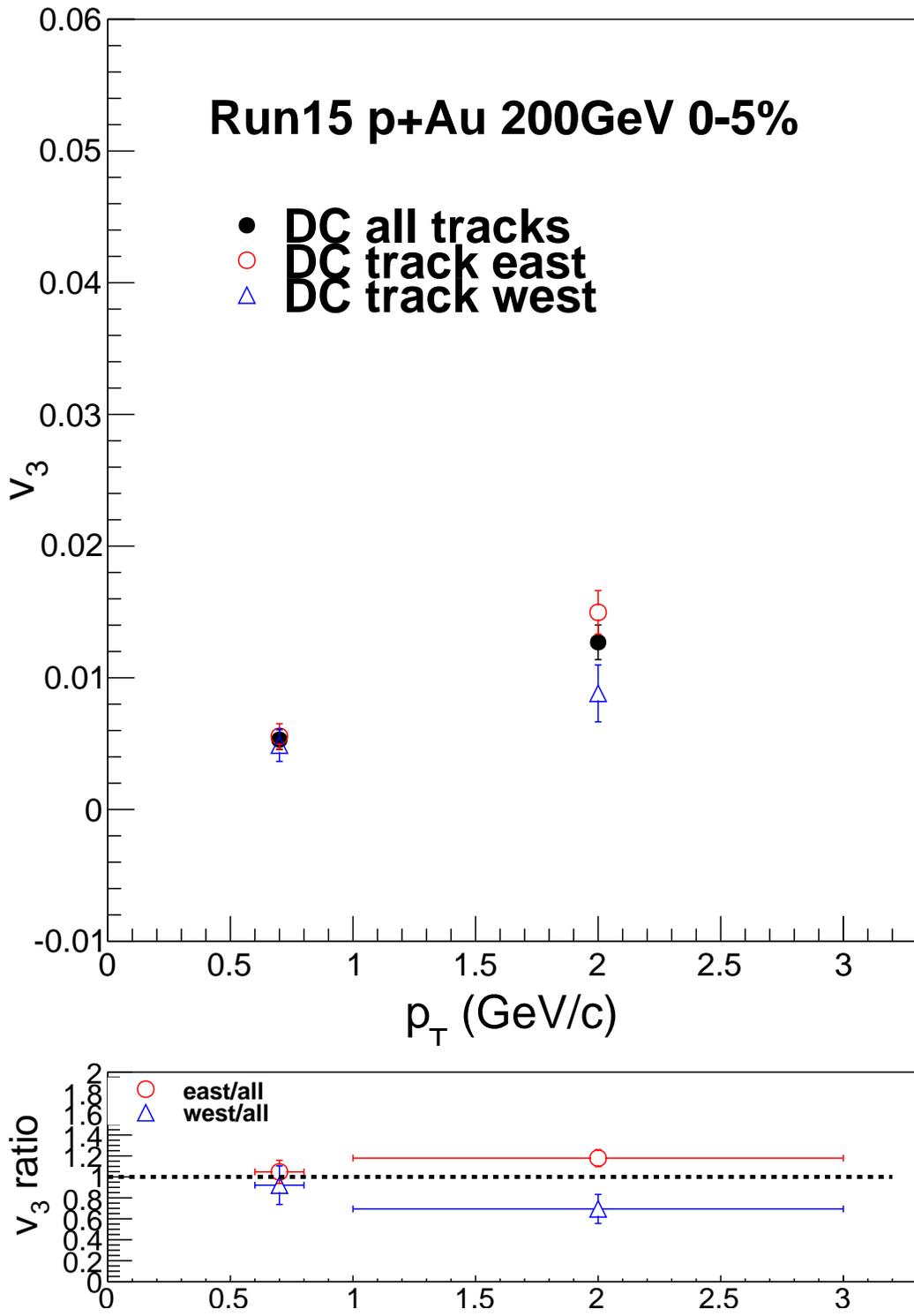
Figure 4.91: Measurement of v_3 systematic results from east/west difference. Here shows the integrated results over p_T ranged from 0.4-1 GeV/c and 1-3 GeV/c.

Source	Type	Upper Limit	Lower Limit
Track Matching and EP resolution	B+C	4%	4%
Pile-Up	B	0%	3%
Resolution syst.	B	7%	7%
Resolution stat.	B	13%	13%
EP-Detector	B	0%	0%
E/W Difference	B	9%	9%
Non-flow effect	B	11% - 113%	0%
Total	B+C	21%-114%	18%

Table 4.3: Systematics table for unidentified $v_3(p_T)$.
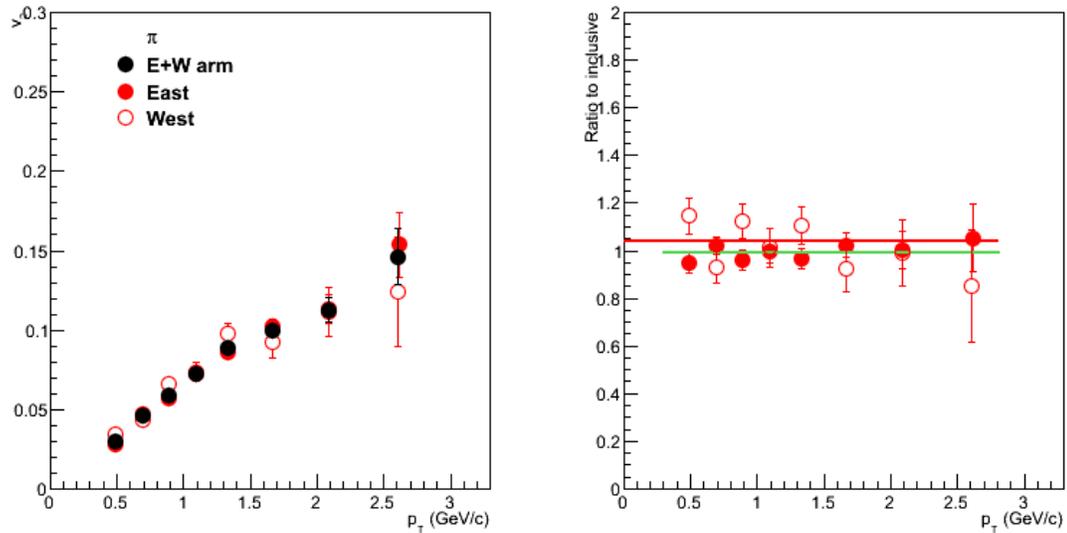
Figure 4.92: The pion's v_2 measured by TOFe and TOFw separately as a function of p_T from FVTXs in 0-5% central $p + Au$ collisions
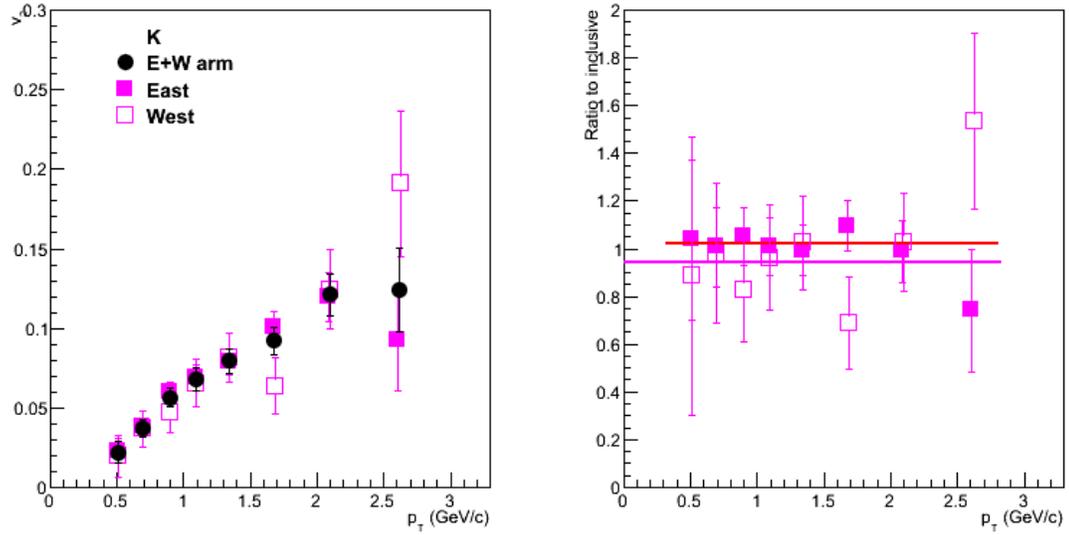
Figure 4.93: The kaon's v_2 measured by TOFe and TOFw separately as a function of p_T from FVTXs in 0-5% central $p + Au$ collisions
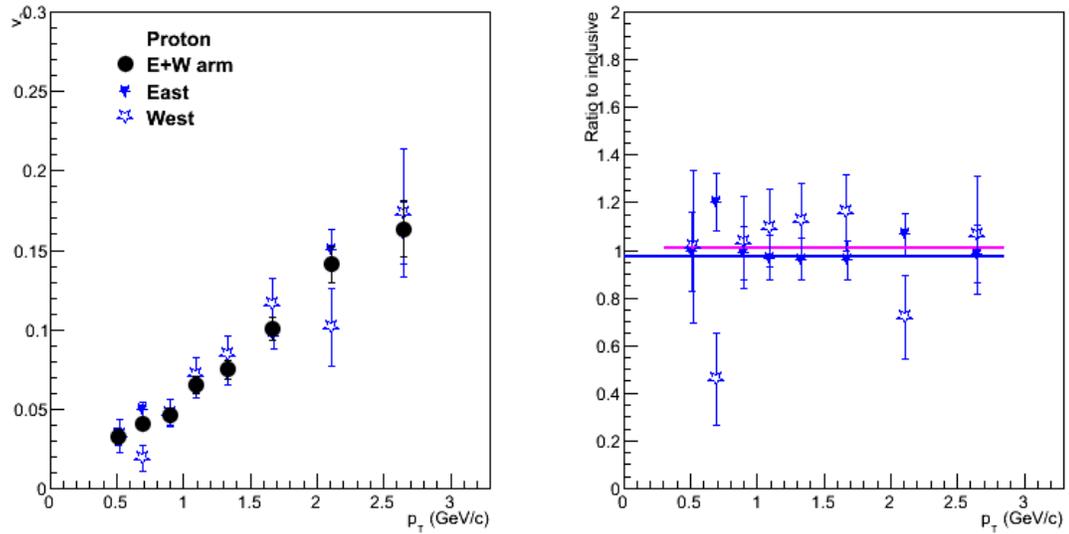
Figure 4.94: The proton's v_2 measured by TOFe and TOFw separately as a function of p_T from FVTXs in 0-5% central $p + Au$ collisions

2) v_2 from background tracks; 3) pile-up effect; 4) difference between tofw and tofe; and 5)PID purity. For 1), 2) and 3), they are same as charged hadrons, For the 4), the difference are shown in the Fig. 4.92, Fig. 4.93 and Fig. 4.94 for pion, kaon and proton respectively. The difference is within the 5% difference of the v_2 from tofw+tofe together. 5% systematic uncertainties are assigned for it.

For 5), The uncertainty due to particle purity is estimated by varying the PID selection bands changing from 2 σ to 1.5 σ in m^2 and redoing the analysis of v_2. The differences are shown in Fig. 4.95. A systematic uncertainty of 2% is assigned for the pions, kaons and protons. Since the DCA cut effectively removes the background protons, no additional uncertainty is assigned for it.
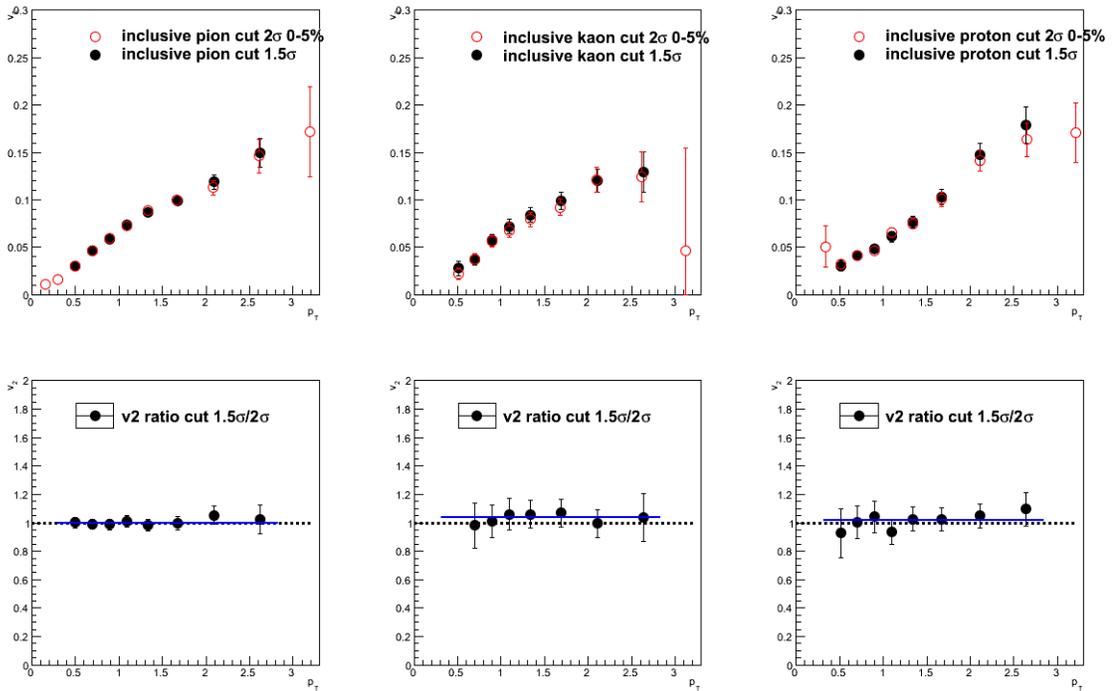
Figure 4.95: The v_2 of p_T difference by changing the purity cut from 2 sigma to 1.5 sigma of from FVTXs in 0-5% central $p + Au$ collisions
.

The detailed systematic uncertainties table can be found in Table. 4.4,

Table 4.4: Systematic table for identified particle v_2 (p_T).

Uncertainty Sources	p+Au	^{3}He+Au	Type
Track Background	2%	2%	A
Event Pile-up	$^{+4}_{-0}$%	$^{+5}_{-0}$%	B
Non-flow	$^{+0}_{-23}$%	$^{+0}_{-7}$%	B
Beam Angle	5%	5%	C
Event-Plane Detectors	3%	5%	C
Particle Purity	2%	2%	B

RESULTS

5.1 Measurement of Correlation Functions in p+Au Collisions

Using the two-particle correlation method, we can plot the 1D 2-particle correlation function in different p_T ranges and event classes. Below are the correlation functions in the range $1.0 < p_T < 3.0$ (GeV/c). To estimate the elementary contribution from jets and res-
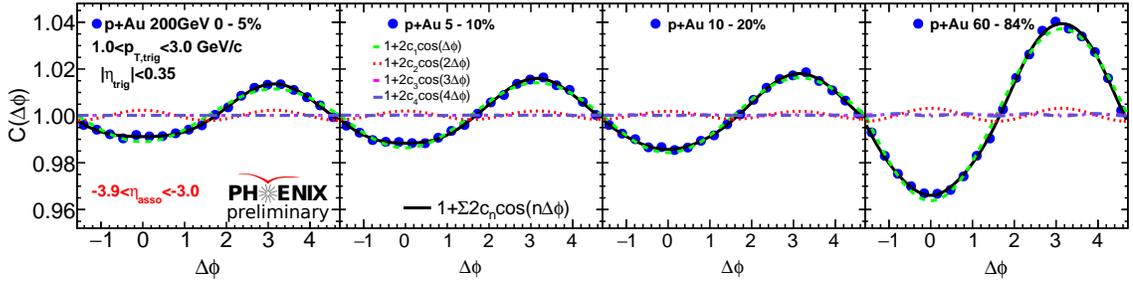
Figure 5.1: The azimuthal correlation functions $C(\Delta\phi, p_T)$, as defined in Eq. 4.3 , for track-PMT pairs with different centrality selections in $1.0 < p_T < 3.0$ (GeV/c) central p+Au collisions at $\sqrt{s_{NN}} = 200$ GeV. The pairs are formed between charged tracks measured in the PHENIX central arms at $|\eta| < 0.35$ and BBC in the Au-going in the range $-3.7 < \eta < -3.1$. Each correlation function is fit with a four-term Fourier cosine expansion; the individual components n = 1 to n = 4 are drawn on each panel, together with the fit function sum.

onance decays, we also measured the long range angular correlation in p+p collisions. The p+p data is taken in the years 2005, 2006, 2008 and 2009. Since the BBC-S and BBC-N are identical, we combine them for pp measurement to further enhance the statistics. Fig. 5.1 shows the correlation functions $C(\Delta\phi, p_T)$ for different p_T bins, for the high multiplicity p+Au collisions and for minimum bias p+p collisions.

Since we see a flat shape at the near-side ($\Delta\phi = 0$) regime at p+Au, which is a hint of a ridge structure, we turn to the event plane method to precisely measure the second- and
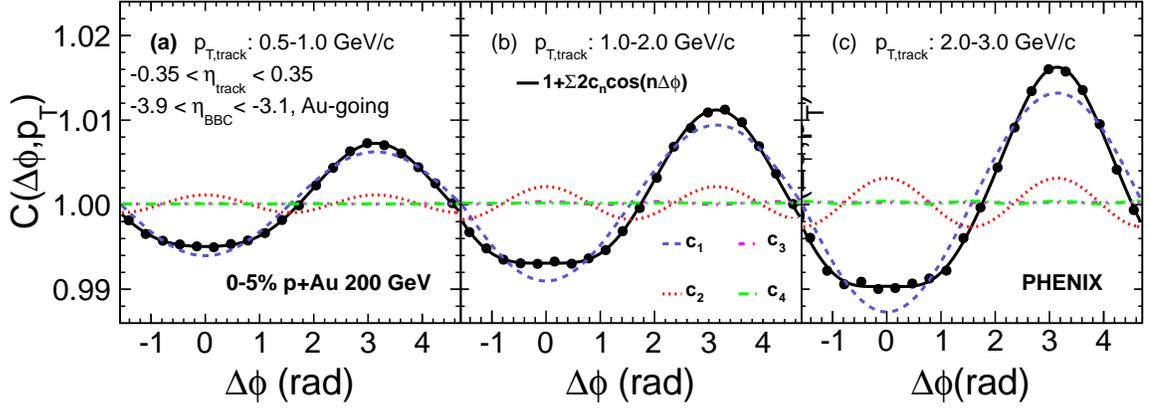
Figure 5.2: The azimuthal correlation functions $C(\Delta\phi, p_T)$, as defined in Eq. 4.3 , for track-PMT pairs with different track p_T selections in 0-5% central p+Au collisions at $\sqrt{s_{NN}}$= 200 GeV. The pairs are formed between charged tracks measured in the PHENIX central arms at $|\eta| < 0.35$ and BBC in the Au-going in the range $-3.7 < \eta < -3.1$. Each correlation function is fit with a four-term Fourier cosine expansion; the individual components n = 1 to n = 4 are drawn on each panel, together with the fit function sum.
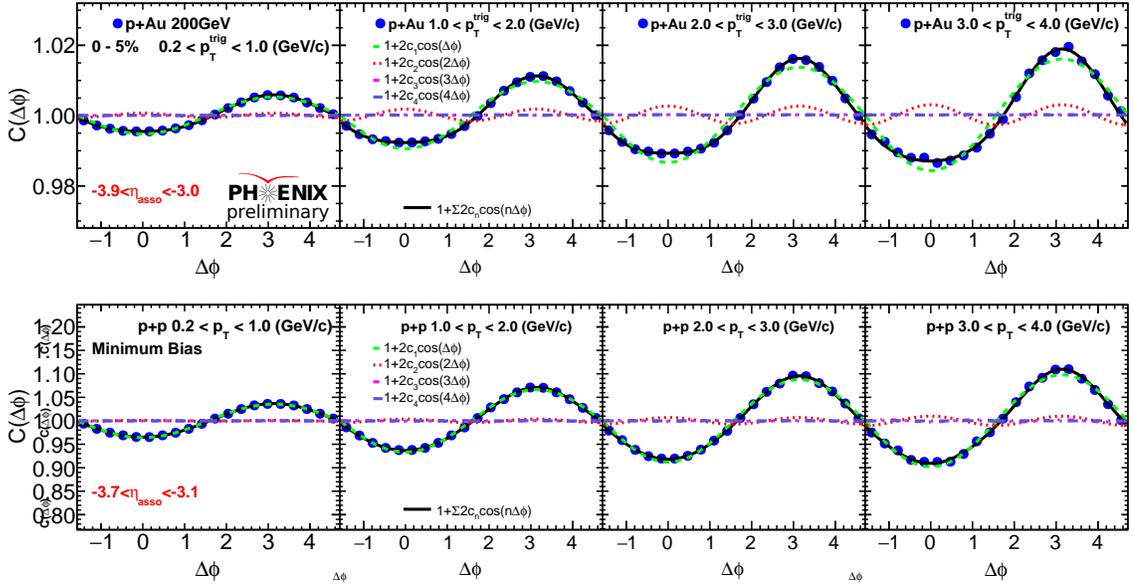
Figure 5.3: Top panel: The azimuthal correlation functions $C(\Delta\phi, p_T)$, as defined in Eq. 4.3 , for track-PMT pairs with different p_T range in centrality 0-5% central p+Au collisions at $\sqrt{s_{NN}}$= 200 GeV. The pairs are formed between charged tracks measured in the PHENIX central arms at $|\eta| < 0.35$ and BBC in the Au-going in the range $-3.7 < \eta < -3.1$. Bottom panel: The azimuthal correlation functions $C(\Delta\phi, p_T)$, for track-PMT pairs with different p_T range in minimum bias p+p collisions at $\sqrt{s_{NN}}$= 200 GeV.

third-order azimuthal anisotropy.

5.2 Event Plane Measurements of $v_n(p_T)$ in p+Au collisions

Fig. 5.4 shows the v_2 vs p_T in the top 0-5% events in p+Au collisions.
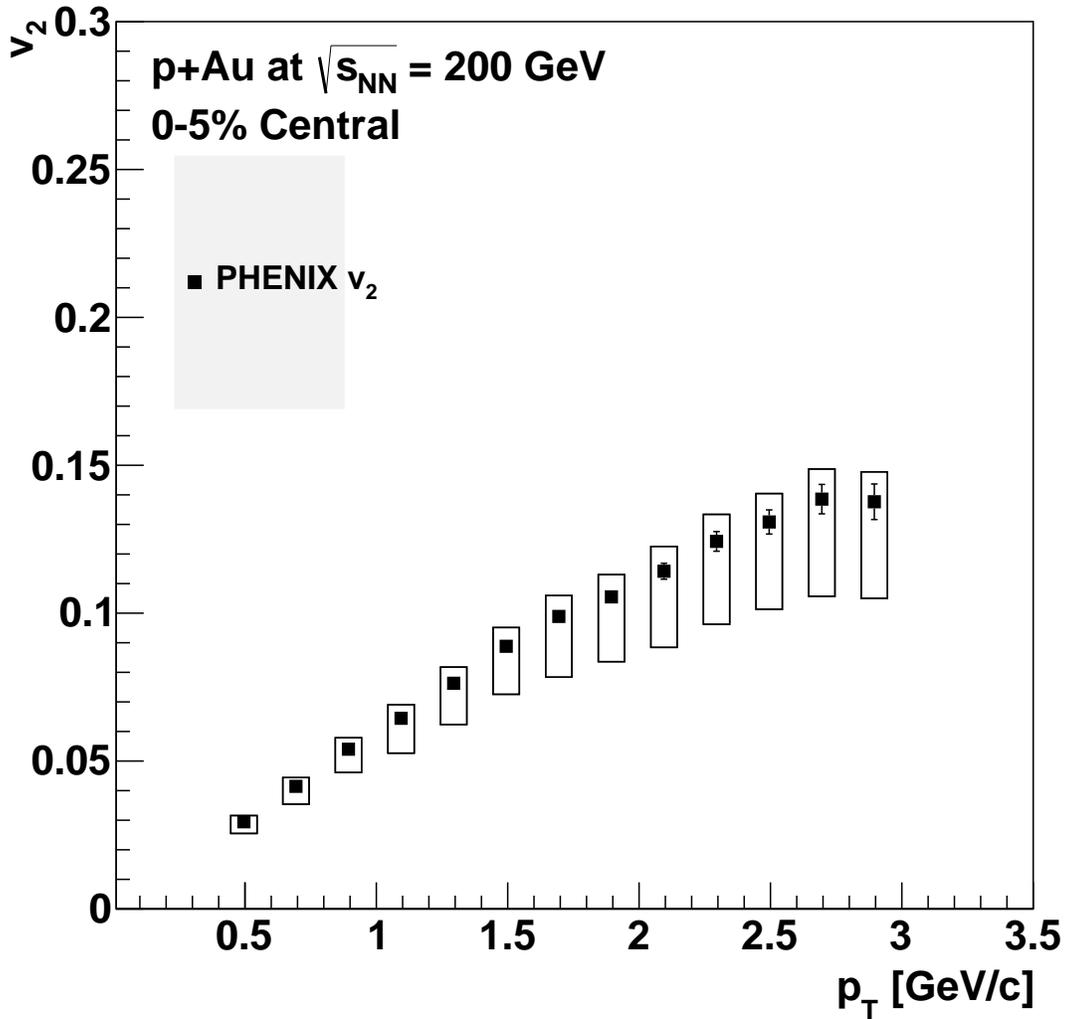
Figure 5.4: Measurement of $v_2(p_T)$ for charged hadrons using event plane method.

Fig. 5.5 shows the v_3 vs p_T in top 0-5% events in p+Au collisions.

Fig. 5.6 shows the v_2 vs p_T in top 0-5% events in p+Au collision for identified particles in comparison to similar measurements in d+Au and ^{3}He+Au collisions.
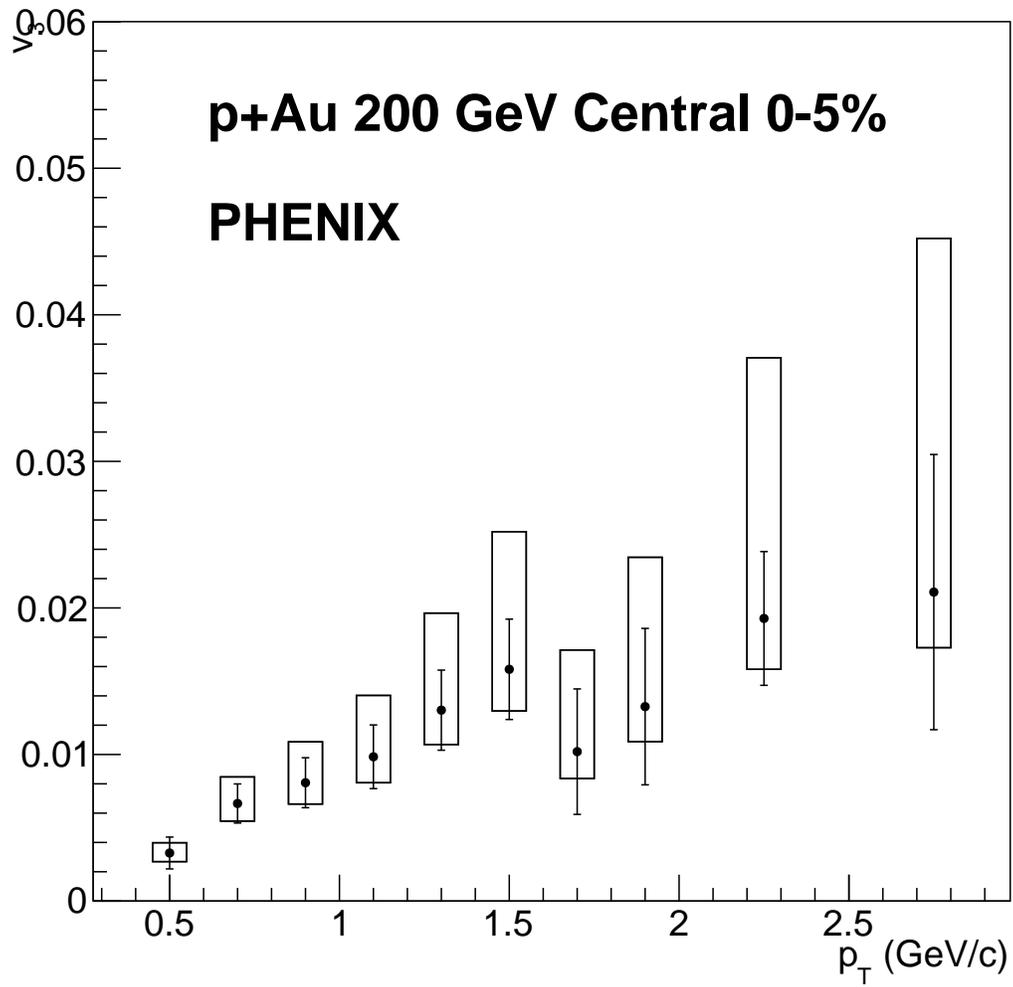
Figure 5.5: Measurement of $v_3(p_T)$ for charged hadrons using event plane method.
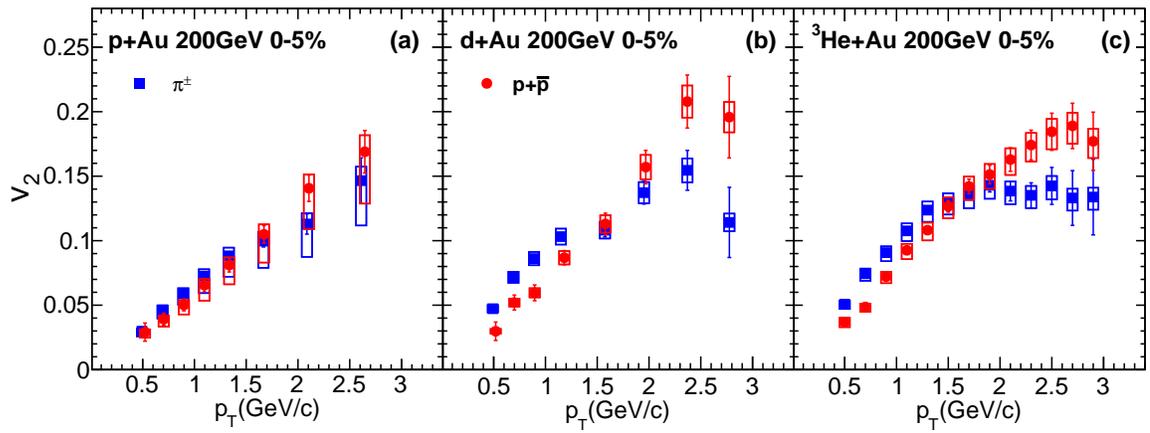
Figure 5.6: Measurement of $v_2(p_T)$ for identified particles using event plane method.

Chapter 6

DISCUSSIONS

With the results at hand, we can now discuss our hypothesis tests by comparing with other measurements and various theoretical models to reach the conclusions.

6.1   Hypothesis Test 1 – Initial Geometry Effect in Small Systems

6.1.1   Measurement of p+Au v_2 Results Compared to Different Models

We have several theoretical models that predict the flow coefficients of p+Au collisions at the top 0-5% centrality. Here Fig. 6.1 shows the comparison between several different models: AMPT, SUPERSONIC, SONIC, IPGlasma+Hydro and PHENIX p+Au data results.

It is seen that SONIC and SUPERSONIC model describe the data well within the uncertainties, throughout the measured range from low p_T to high p_T. They incorporate Glauber initial condition and hydrodynamics evolution. AMPT can match the data up to about 1 GeV/c, but under-predicts the data above that p_T range. The IP-Glasma initial condition plus hydrodynamics well under-predicts the p+Au data and does not reflect the non-linear shape of the $v_2(p_T)$ distribution.

6.1.2   Measurement of v_2 in p+Au Collisions in Comparison to Measurements in Central d+Au and ^{3}He+Au Collisions

PHENIX also has published results on d+Au and ^{3}He+Au v_2. We make a direct comparison of v_2 between these three small systems in Fig. 6.2.

We can see that d+Au and ^{3}He+Au are grouped together, while p+Au data are systematically lower. They are all predicted by SONIC model simultaneously. The SONIC model incorporates standard Monte Carlo Glauber initial conditions followed by viscous hydro-
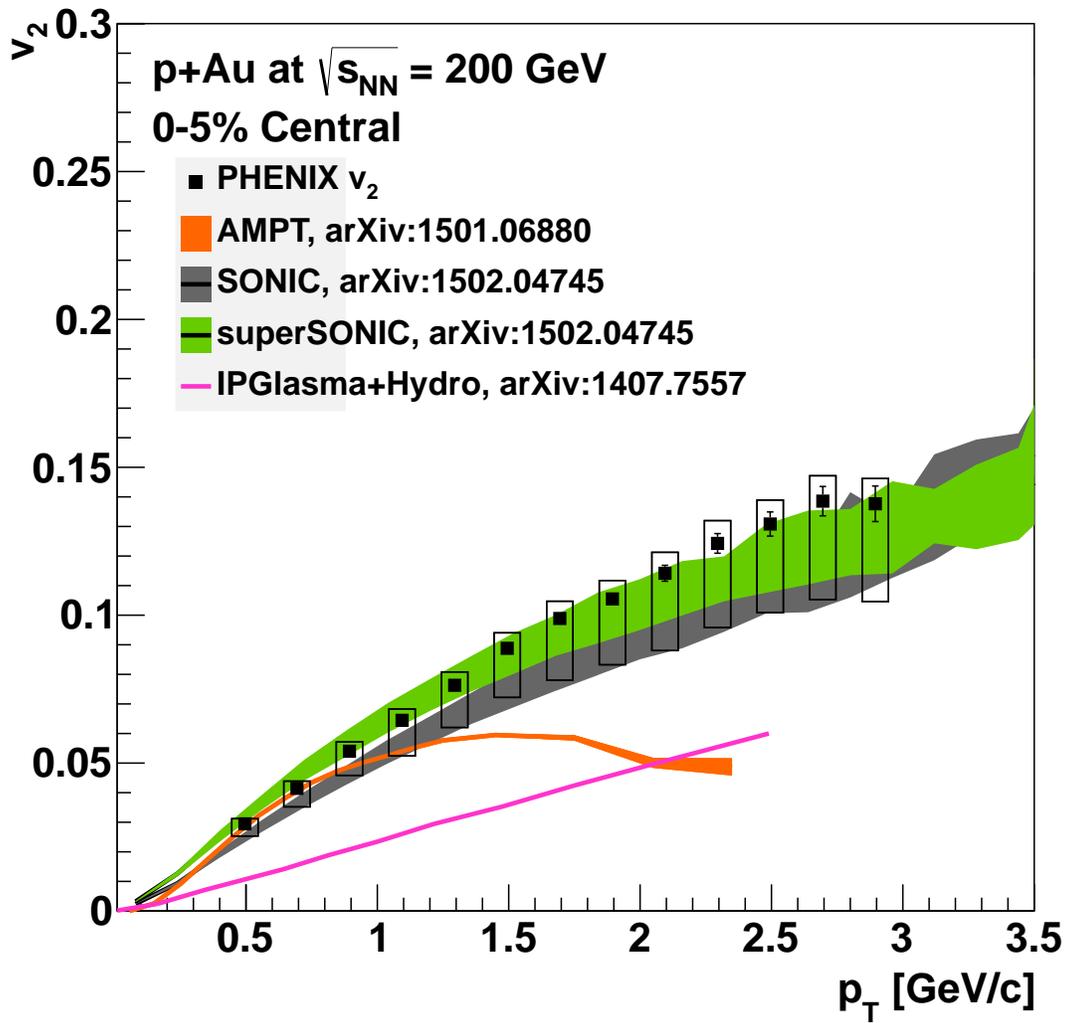
Figure 6.1: Measurement of *p*+Au *v*₂ results in comparison with various model calculations.
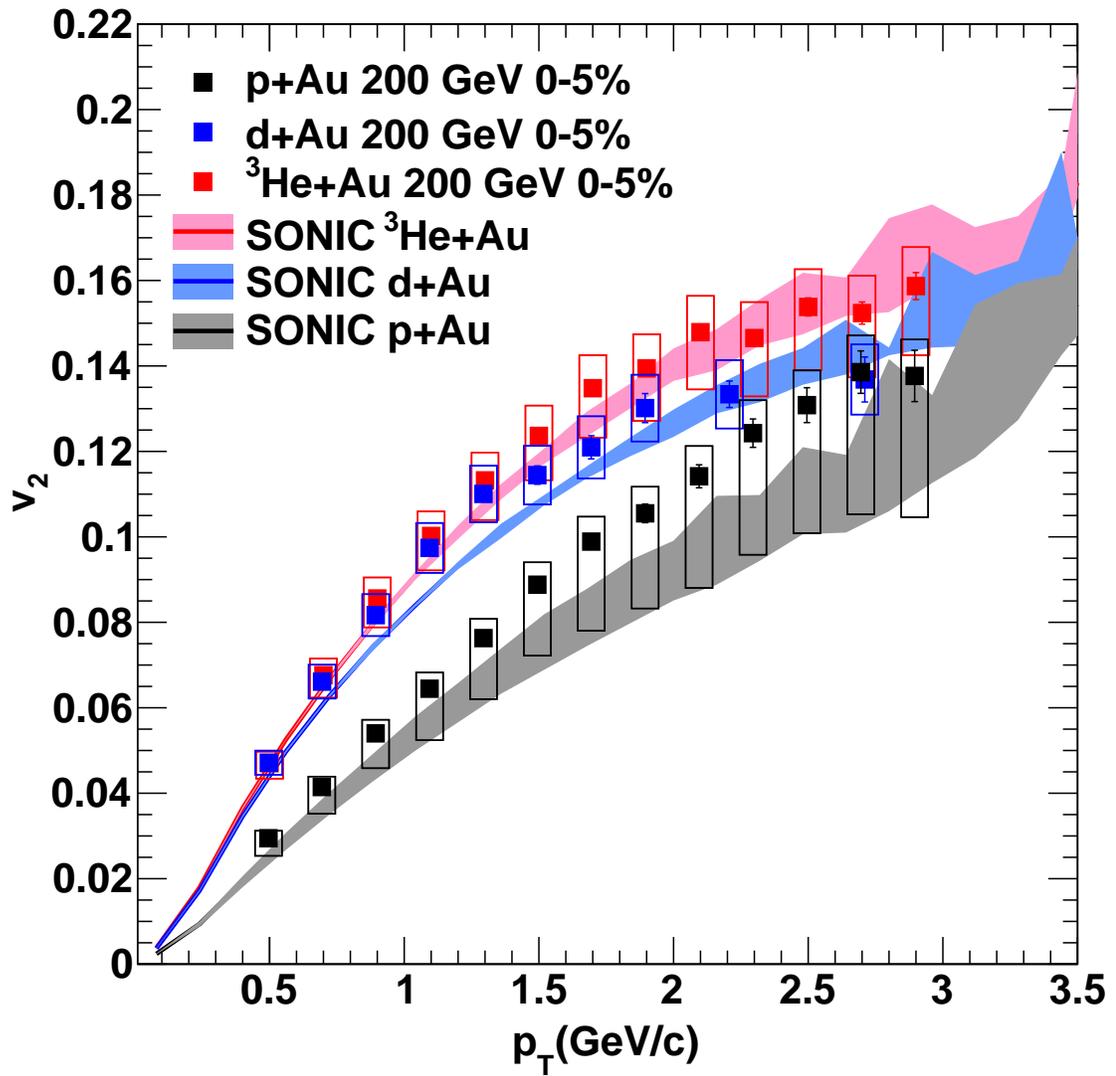
Figure 6.2: Comparison of p/d/^{3}+Au 200GeV v_2 results, overlaid with SONIC predictions.

dynamics with $\eta/s = 0.08$, and a transition to a hadronic cascade at $T_c = 170$ MeV. These model calculations for each system are matched to the charged particle density at midrapidity, with the exact values for 0%-5% centrality of 10.0, 20.0, and 27.0, for p+Au, d+Au, and ^{3}He+Au collisions, respectively [36]. The value of 10.0 for p+Au was extrapolated from measurements in the other two systems [36]. Although we have control over the same centrality range for the three systems, the multiplicity for these systems are different. The calculations incorporate both the change in eccentricity and the relative collision multiplicity. In all cases, a good agreement is seen within uncertainties between the data and the calculation. This a strong evidence to support the idea that initial geometry, coupled to the hydrodynamic evolution of the medium is the key to understand small system collectivity.
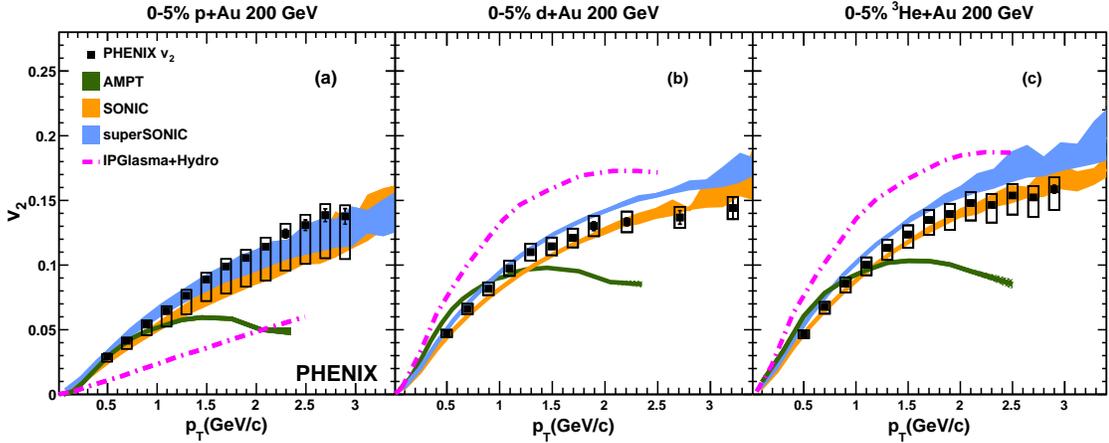
Figure 6.3: Comparison of p/d/^{3}He+Au 200GeV v_n results to various theory model predictions.

The SUPERSONIC model uses the same settings for initial conditions, hydrodynamic expansion, and hadronic cascade as SONIC, yet additionally incorporates pre-equilibrium dynamics with a calculation in the framework of the AdS/CFT correspondence [59, 60, 35]. These two models agree well with the data within uncertainties, supporting the idea of that the initial geometry drives the v_n signal in all systems. Furthermore, this illustrates how these results impose useful constraints to reduce the number of *free parameters* of the model, e.g., η/s, the transition temperature to a hadronic freeze-out, and the Monte Carlo

Glauber smearing of nucleon coordinates of $\sigma = 0.4$ fm.

Calculations using IP-Glasma initial conditions followed by viscous hydrodynamics have been successfully used to describe collectivity in A+A collisions [61]. However, when applied to small collision systems with $\eta/s = 0.12$ as shown in Fig. 6.3, they overestimate the data for d+Au and ^{3}He+Au, while underestimate the data for p+Au. IP-Glasma generates very *circular* initial conditions for p+Au, assume the protons have round shape, resulting in low ε_2 values; however, the presence of several hot spots in d+Au and ^{3}He+Au result in IP-Glasma values for ε_2 more comparable to those from Glauber. This is shown in Table 6.1. For the d+Au and ^{3}He+Au data, a better agreement with data can be achieved by increasing the value of η/s or by including a hadronic cascade stage. However, in the mean time, such modification lowers the prediction for p+Au even further. This demonstrates that IP-Glasma is not a appropriate initial conditions model to account for measured v_n via hydrodynamic flow for small systems.

AMPT combines partonic and hadronic scattering in a single model. Despite the very different physics of AMPT compared to the other models, it has successfully been applied to a variety of systems at RHIC and the LHC [62, 63, 64, 65, 65]. Central AMPT events with impact parameter $b < 2$ have a midrapidity $dN_{ch}/d\eta = 8.1$, 14.8, and 20.7 for p+Au, d+Au, and ^{3}He+Au, respectively, well matched the experimental data. The AMPT samples were generated with the same Monte Carlo Glauber initial conditions used to characterize event geometry, and thus have very similar eccentricities to those given in Table 6.1. Using the initial Glauber geometry information to compute v_2 relative to the participant plane [63] yields results that agree reasonably well with the data below $p_T \approx 1$ GeV/c, yet underpredict them at higher p_T.

6.1.3 Initial Eccentricity Scaling

To investigate the initial geometry effect quantitatively, we try to establish a simple relationship between the v_2 in the three small systems, which reflects the final state correlation,

with initial eccentricities ε_2 which are gotten from different initial model calculations. See Fig. 6.4.
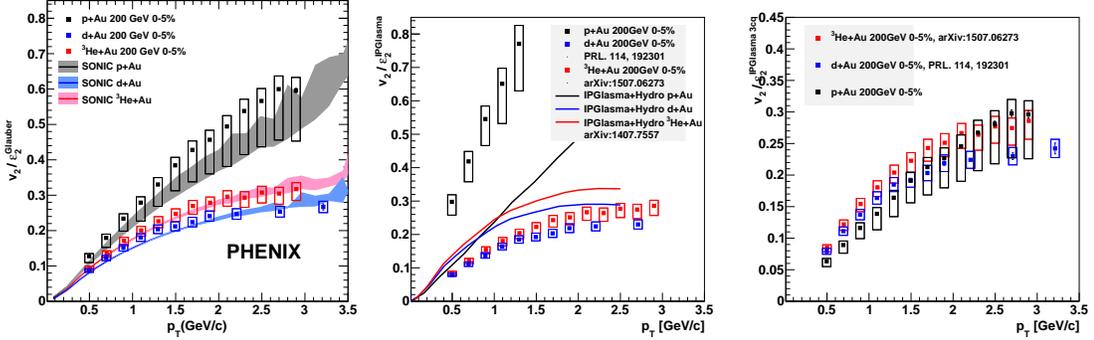
Figure 6.4: Comparison of p/d/^{3}He+Au 200GeV v_2/ε_2 results to various theory model predictions. (left)ε_2 comes from Glauber initial configuration, (middle) ε_2 comes from CGC initial configuration, (right) ε_2 comes from CGC constituent quarks configuration.

From the calculation of Monte Carlo Glauber model, Table. 6.1 shows the initial eccentricity of these collisions for small impact parameter, which corresponds to central events.

To further explore this idea, we divide the v_2 curves by their corresponding ε_2 from Table 2.1, attempting to establish a linear scaling relation between the two quantities. Fig. 6.4 shows that the ratios do not collapse to a common curve. This behavior is also reproduced by the SONIC calculation, as expected since both data and calculations are divided by the same ε_2 values. The imperfect eccentricity scaling in the SONIC calculation can be understood from d+Au and ^{3}He+Au events where the neutron and proton from the deuteron projectile are far separated and create hot spots upon impacting the Au nucleus. There are a small set of events with very large $\varepsilon_{2(3)}$, but with small final v_2. These events were found to have those two/three hot spots are so far apart, thus ε is large, but the hydrodynamic fluids never connect during the time evolution, and thus there is almost no elliptic flow.

Constituent quark models incorporate collisions between constituent quarks [66], which provides additional partonic degrees of freedom extending the current Glauber approach. This framework has been successfully applied to the description of midrapidity charged particle multiplicity and transverse energy production [25, 67]. In Fig. 13(f) of Ref. [68],
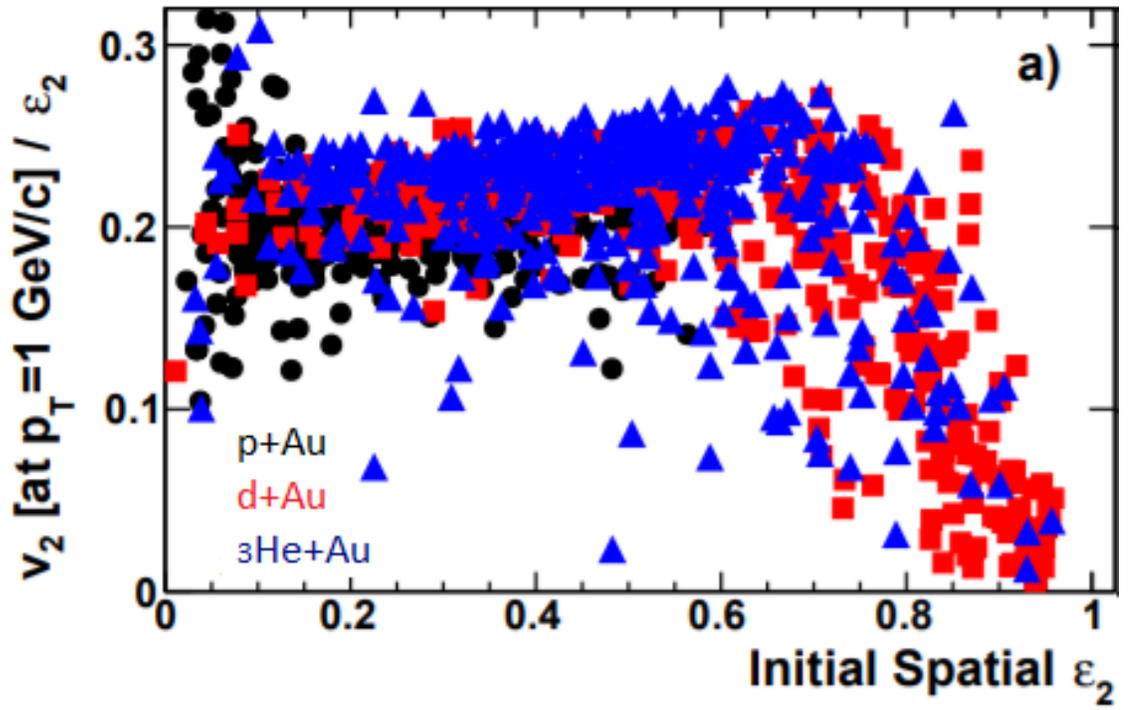
Figure 6.5: Scatter plot for v_2/ε_2 versus ε_2 for pions with $p_T = 1.0$ GeV/c from p+Au, d+Au, and ^{3}He+Au central (b < 2 fm) events. The results are with input parameters $\eta/s = 1/4\pi$ and initial Gaussian smearing $\sigma = 0.4$ fm and freeze-out temperatures of $T_f = 170$ MeV, respectively. [7]

Table 6.1: Initial eccentricity ε_2 of small systems at $\sqrt{s_{NN}} = 200\,\text{GeV}$ for 0%-5% centrality from Monte Carlo Glauber initial conditions smeared with a two-dimensional Gaussian of width $\sigma = 0.4$ fm, and IP-Glasma initial conditions.

	p+Au	d+Au	^{3}He+Au
Glauber $\langle \varepsilon_2 \rangle$	0.23 ± 0.01	0.54 ± 0.04	0.50 ± 0.02
IP-Glasma $\langle \varepsilon_2 \rangle$	0.10 ± 0.02	0.59 ± 0.01	0.55 ± 0.01

the initial eccentricities ε_2 in p+Au, d+Au, and ^{3}He+Au obtained by incorporating constituent quarks in addition to multiplicity fluctuations are found to be $\varepsilon_2 = 0.42$, 0.54, and 0.54, respectively. This calculation assumes a low-x smeared Gaussian gluons density distribution with width 0.3 fm around each constituent quark. The constituent quark Glauber model results shows that the d+Au and ^{3}He+Au systems exhibit almost no change in the ε_2 values. However, under the same circumstances, p+Au has a substantially larger ε_2 than in the models shown in Table 6.1. The constituent quark model provides additional variance to the shape of the traditional 'round' proton and thus significantly increase the initial eccentricity. The scaling behavior is more consistent among the geometry-dependent systems when using constituent quark model especially concerning proton collisions.

6.1.4 Measurement of p+Au v_3 Results Compared to Models

Fig. 6.6 shows the $v_3(p_T)$ in top 0-5% events in $p/d/^3$He+Au collisions. The $v_3(p_T)$ from ^{3}He+Au is larger than the the $v_3(p_T)$ for p/d+Au which are consistent with each other.

From table 6.2, we can conclude that the ordering of ε_3 also follows that ^{3}He+Au is greater that p/d+Au, which is another strong evidence of an initial geometry effect.

Several theoretical models predict the flow coefficients in p+Au collisions at the top 0-5% centrality. Fig. 6.7 shows the comparison between the PHENIX p+Au data and several different models: AMPT, (SUPER)SONIC, and iEBE-VISHNU (with and without scattering). With the exception of AMPT which is a transport model, these are all hydrodynamic models.

Table 6.2: Initial eccentricity ε_3 of small systems at $\sqrt{s_{NN}} = 200\,\text{GeV}$ for 0%-5% centrality from Monte Carlo Glauber initial conditions smeared with a two-dimensional Gaussian of width $\sigma = 0.4$ fm

	p+Au	d+Au	^{3}He+Au
Glauber $\langle \varepsilon_3 \rangle$	0.16 ± 0.01	0.19 ± 0.01	0.283 ± 0.024

The models (SUPER)SONIC and iEBE-VISHNU use Glauber initial conditions with hadronic cascade. From v_3 alone, we can conclude that the model which describe the data the best is the iEBE-VISHNU model. The two SONIC models over-predict high p_T v_3 while the AMPT overestimates p+Au v_3 but underestimates ^{3}He+Au. The ^{3}He+Au data prefers the version of iEBE-VISHNU with rescattering more.

The $v_2(p_T)$ and $v_3(p_T)$ data for $p/d/^3$He+Au are presented compared to (SUPER)SONIC (Fig. 6.8), iEBE-VISHNU (Fig. 6.9), and AMPT (Fig. 6.10). These pictures give us a general idea about how well different models can fit the second-order/third order and $p/d/^3$He+Au simultaneously, the measurement of v_3 provides additional constraint about the parameters in the models. The SONIC calculations are more consistent with the data than the SU-PERSONIC calculations which include a preflow stage. The iEBE-VISHNU results with and without hadronic rescattering match the data at low p_T, but the values without hadronic rescattering under-predict as p_T increases while the values with hadronic rescattering are mostly within error bars.

6.2 Hypothesis Test 2 – Mass Splitting in Small Systems

If collectivity in small systems indeed originates from the expansion of QGP fluid along pressure gradients determined by initial geometry, there should be a mass order-ing of $v_2(p_T)$ for identified final-state hadrons since they have different masses, flowing in a common velocity field. Strong radial expansion in the hydrodynamic evolution results in a shifting of the anisotropy pattern to higher p_T for higher mass hadrons [69]. This feature of $v_2(m, p_T)$ is one of the key signatures of the collective nature of the QGP formed in A+A
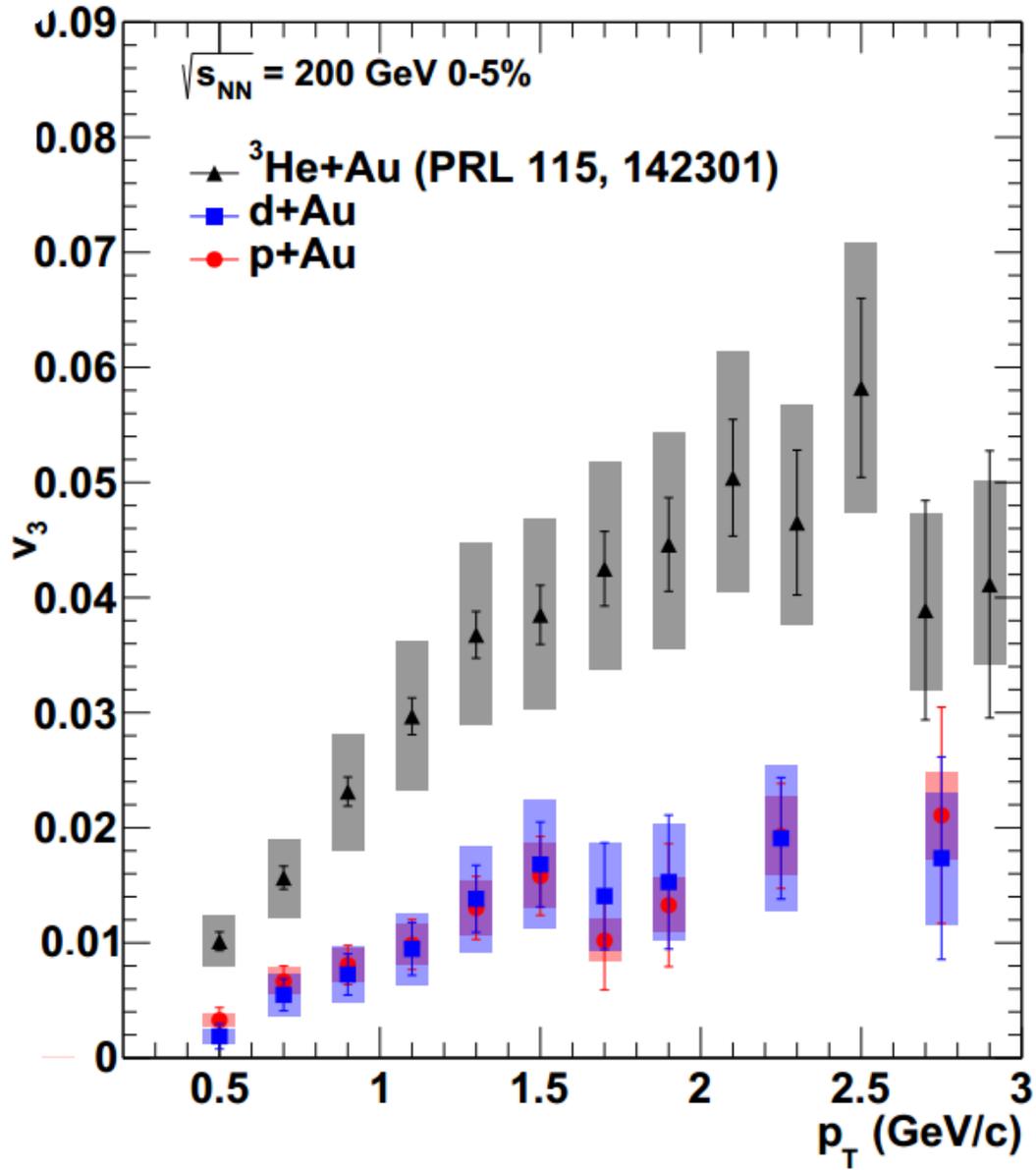
Figure 6.6: Direct comparison of $v_3(p_T)$ results for p/d/^{3}He+Au using event plane method.
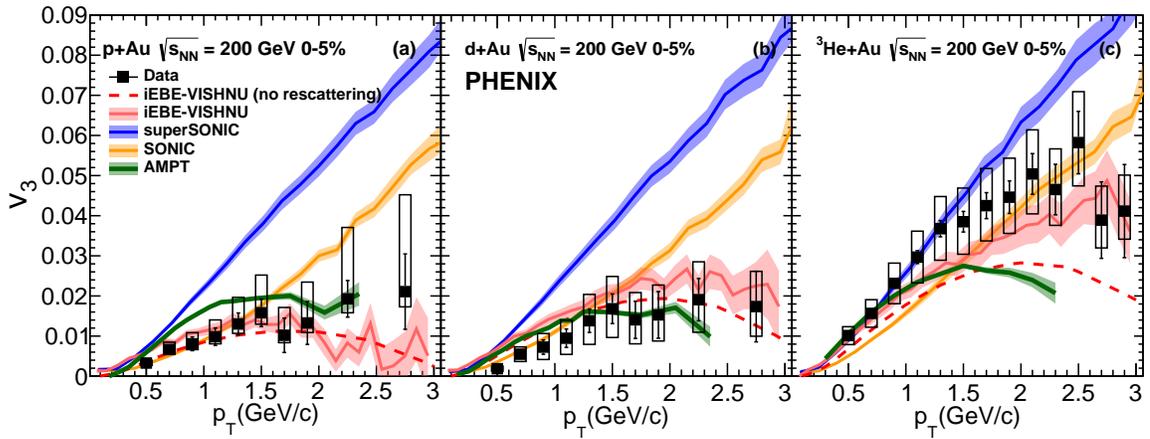
Figure 6.7: Third order azimuthal anisotropy in central (a) p+Au, (b) d+Au, and (c)
^{3}He+Au collisions at $\sqrt{s_{NN}} = 200$ GeV. Theoretical calculations from [(dashed) red curve]
IEBE-VISHNU (without scattering), [solid blue curve] SUPERSONIC, [solid orange curve]
SONIC, and [solid green curve] AMPT are shown in each panel.
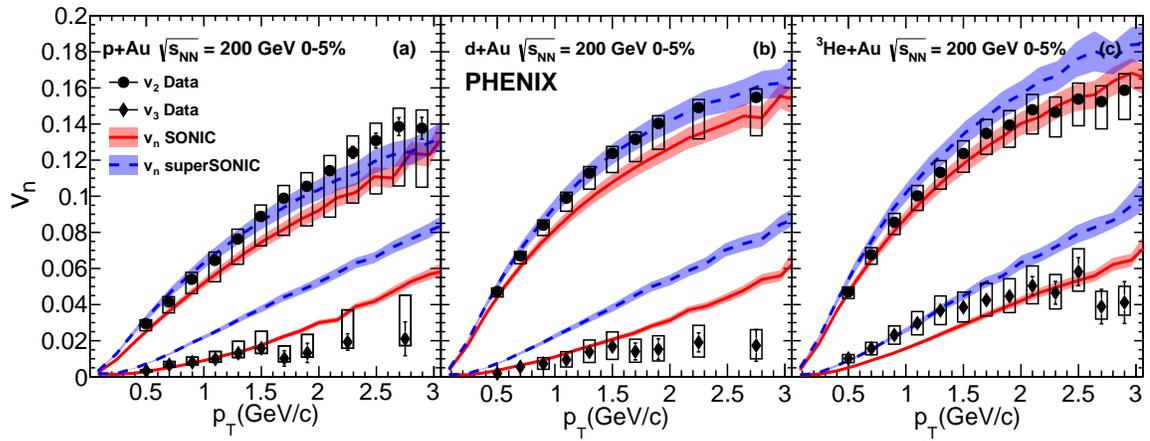
Figure 6.8: Comparison of p+Au v_2 (p_T) and v_3 (p_T) results with (SUPER)SONIC calculations.
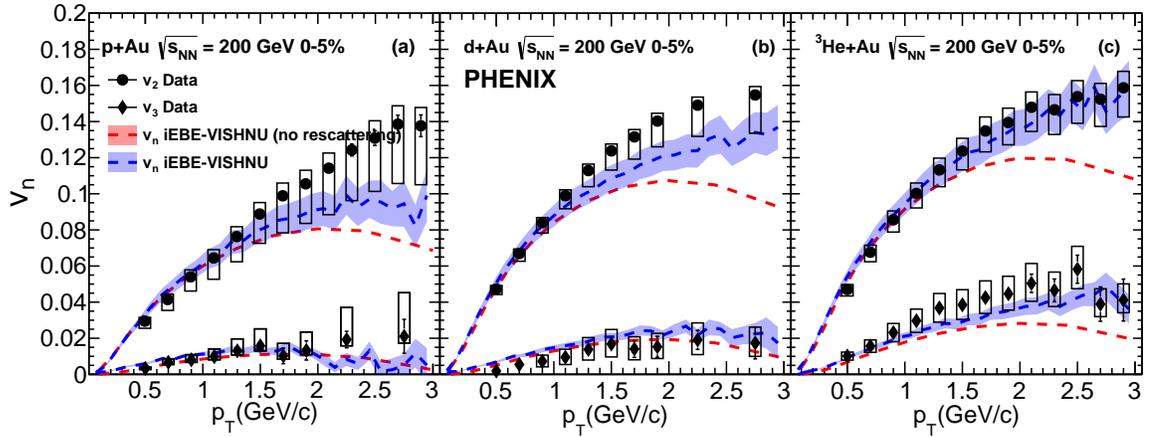
Figure 6.9: Comparison of p+Au $v_2(p_T)$ and $v_3(p_T)$ results with IEBE-VISHNU calculations (with and without hadronic rescattering).
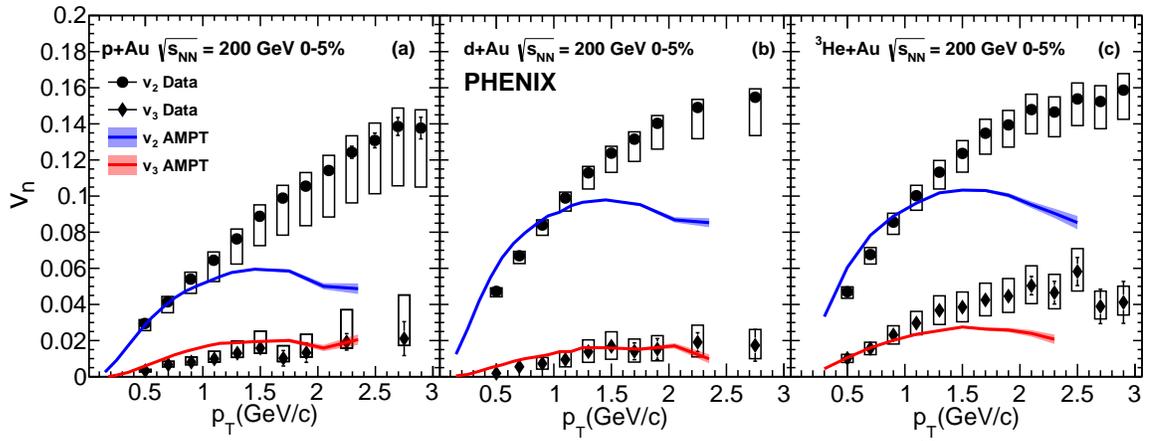
Figure 6.10: Comparison of p+Au $v_2(p_T)$ and v_3 results with AMPT (with hadronic rescattering) calculations.

collisions— see for example [70].

Recently, such mass ordering has been observed in d+Au collisions at RHIC [4] and in p+Pb collisions at the LHC [71, 72]. It is also important to note the AMPT model can also generate this mass ordering/splitting via later-stage hadronic rescattering, which is a totally different mechanism from hydrodynamics and was quite unexpected. In recent measurements at RHIC, the collective flow of identified hadrons in p+Au are seen. It is compared to other geometry measurement as well as different models. Those comparisons can reflect how the anisotropy is developed in each stage of the QGP formation.

In the d+Au and ^{3}He+Au systems, there is a clear separation between the pion and proton v_2, with the pion v_2 being larger than the proton v_2 for $p_T \lesssim 1.5$ GeV/c and this order being reversed at higher p_T. In the p+Au system, the pion and proton $v_2(p_T)$ values show smaller overall splitting. The splitting pattern and the reversal of the mass ordering above $p_T \gtrsim 1.5$ GeV/c is qualitatively the same as has been observed in larger Au+Au collisions at $\sqrt{s_{NN}} = 200$ GeV [70].

6.2.1 Measurement of v_2 of Identified Particles in p+Au Collisions Compared with the AMPT Model

The v_2 results for pions and protons are shown in Fig. 6.11. We also showed the AMPT result with and without re-scattering together with the data points. In the AMPT simulation, we set the parton scattering cross section to be 1.5 mb.

In order to get the true flow (according to the definition), we use the participate plane instead of the event plane. The v_2 in AMPT is calculate relative to the parton participant plane. That is, the event plane is calculated using the initial coordinates of the partons, as they emerge from string melting at early times. From the comparison of AMPT and data, we see that both in the data and AMPT with hadron rescattering the splitting of pions and protons in p+Au is smaller than that in d+Au and ^{3}He+Au. But in the AMPT results without hadron re-scattering, there is no splitting in pion and proton v_2 for $p_T < 1$ GeV. Figure 6.11

117
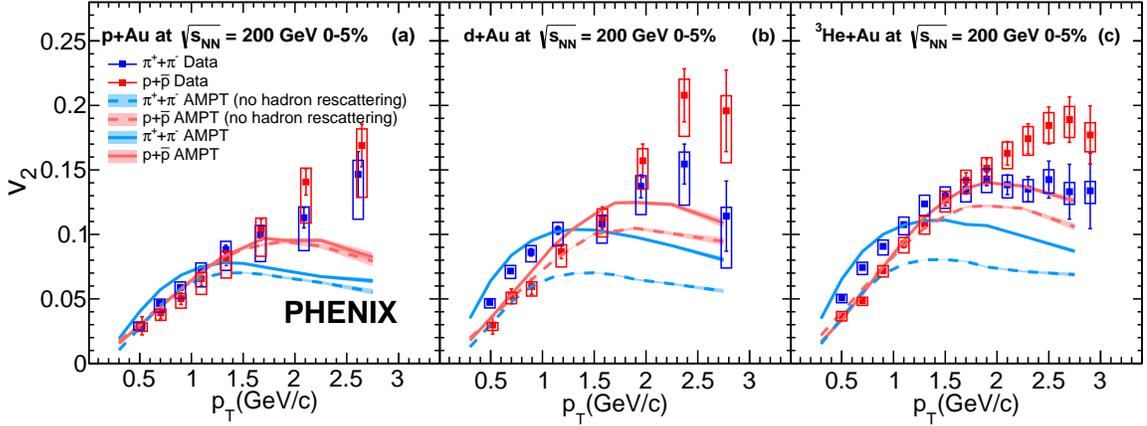
Figure 6.11: Identified particle v_2 (p_T) overlaid with AMPT predictions.

compares the experimental data to transport model calculations of $v_2(p_T)$ for each system using AMPT [73]. We observe that the full AMPT describes the mass-dependent splitting in d+Au and ^{3}He+Au for $p_T < 1.5$ GeV/c. In p+Au collisions, the model results in a smaller mass splitting, which is reversed at high p_T yet below the experimental data. As noted in [74], AMPT generates significant v_2, and in particular the appropriate mass splitting behavior, which was previously thought to be a feature only of hydrodynamics, in the hadronic rescattering stage. As also shown in Figure 6.11, the results without rescattering have significantly lower v_2 values and almost no mass splitting for $p_T < 1$ GeV/c. At higher p_T, the feature of v_2 for protons being greater than pions remains even without hadronic rescattering. This feature is related to the spatial coalescence implementation for hadronization.

6.2.2 Measurement of v_2 of Identified Particles in p+Au Collisions Compared with Hydrodynamics Predictions

Figure 6.12 shows $v_2(p_T)$ for identified pions and protons in 0%-5% central p+Au, d+Au [4], and ^{3}He+Au collisions. For both pions and protons the $v_2(p_T)$ values are higher in d+Au and ^{3}He+Au collisions than in p+Au collisions, as previously observed for in-

clusive charged hadrons [26]. These values follow the ordering of the initial geometric eccentricity $\varepsilon_2(p+\text{Au}) < \varepsilon_2(^3\text{He}+\text{Au}) \approx \varepsilon_2(d+\text{Au})$.

The figure compares the measured $v_2(p_T)$ for each system with hydrodynamic calculations using the SUPERSONIC model and SONIC model. These model comprise standard Monte Carlo Glauber initial conditions followed by a viscous hydrodynamic expansion stage with viscosity over entropy density ratio $\eta/s = 0.08$, hadronization temperature at $T = 170$ MeV, and a subsequent hadronic cascade. The SUPERSONIC additionally incorporates pre-equilibrium dynamics. These hydrodynamic calculations are matched to the measured charged particle density(multiplicity) at midrapidity in the 0-5% centrality class for $d+\text{Au}$ and $^3\text{He}+\text{Au}$ for direct comparison(i.e., $dN_{ch}/d\eta = 20.0$ and 27.0, respectively. Since $dN_{ch}/d\eta$ has not yet been measured in $p+\text{Au}$ collisions, a value of $dN_{ch}/d\eta = 10.0$ was extrapolated for this system.)

We observe that the hydrodynamic calculations agree with the data within uncertainties at low p_T, but fail to describe the reversal of the pion and proton v_2 ordering for $p_T > 1.5$ GeV/c. For $p_T < 1.5$ GeV/c, the mass splitting increases in going from $p+\text{Au}$ to $d+\text{Au}$ and $^3\text{He}+\text{Au}$ as also seen in the data.

At high p_T, viscous hydrodynamics effects and the incorporation of late stage hadronic rescattering have the effect of lowering the v_2 values, suppessing pions more than protons. This can be seen in the SUPERSONIC calculations, comparing v_2 with and without rescattering effect. It is noticeable that the predicted high p_T splitting in $p+\text{Au}$ is much smaller than that seen in the $d+\text{Au}$ and $^3\text{He}+\text{Au}$ data. In this high p_T region, it is proposed that hadronization via recombination [75] can be an explaination of the v_2 splitting in small systems as we see in larger systems in [76, 77].

Figure 6.13 shows results from another viscous hydrodynamic calculation, iEBE-VISHNU [40]. The calculation includes event-by-event fluctuating initial conditions via Monte Carlo Glauber simulation and then viscous hydrodynamics starting at $\tau_0 = 0.6$ fm/c. The hydrodynamic evolution utilizes an $\eta/s = 0.08$ for RHIC energies and with critical temperature at $T_c =$
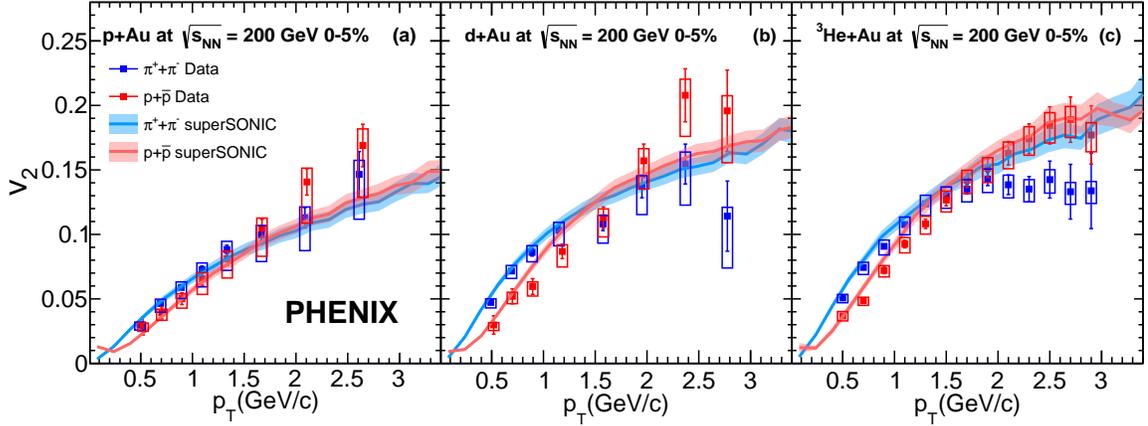
Figure 6.12: Identified particle v_2 (p_T) overlaid with SUPERSONIC predictions.

155 MeV. After that point, hadronization occurs and hadronic rescattering is implemented using URQMD 3.4 [38, 78]. The calculations with viscous hydrodynamics followed by hadronic rescattering show good agreement with the experimental data for all three small systems. Also shown are results with no hadronic rescattering that reveal almost no change in the v_2 for pions and protons for $p_T < 1.5$ GeV/c. The authors [40] conclude that hadronic rescattering plays a modest but important role in the system development and particle species dependence of v_2 in these small systems.
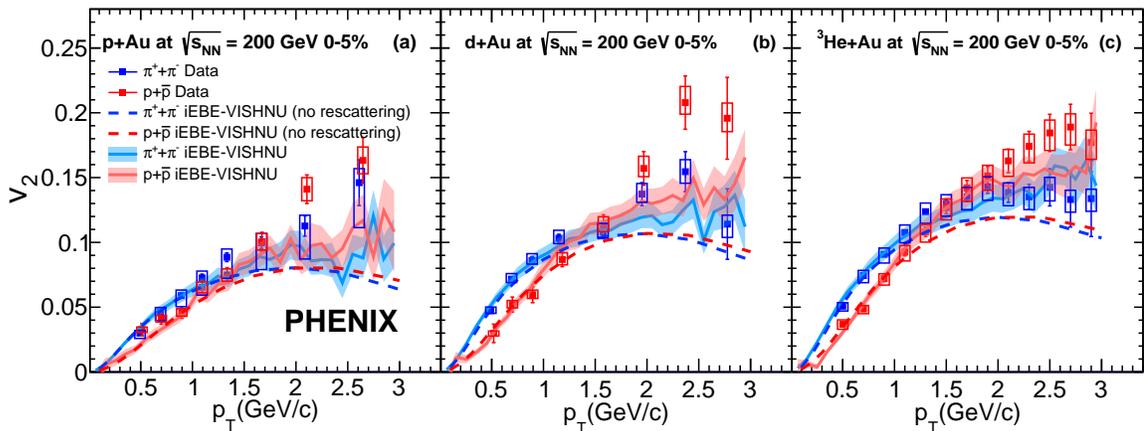
Figure 6.13: Identified particle v_2 (p_T) overlaid with iEBE-VISHNU predictions.

6.2.3 Measurement of the Ratio of v_2 for Different Particle Species

We also showed the ratio of v_2 for pions and protons, the result is shown in Fig.6.14. In the ratio plot, many systematic uncertainties cancel because they are from the same source and independent of particle species. Thus one sees more precisely that the data exhibit a similar trend in all collisions systems where the pion v_2 is larger than the proton v_2 for $p_T < 1.5$ GeV/c, with the order reversed at higher p_T. Linear fits on these ratios ranged from 0.5 GeV/c to 3.0 GeV/c , which include both the statistical and the systematic uncertainties, yield slope values of -0.22 ± 0.07 in p+Au collisions, -0.40 ± 0.07 in d+Au collisions, and -0.34 ± 0.03 in ^{3}He+Au collisions. In this ratio, one can clearly see that SUPERSONIC, iEBE-VISHNU, and the full AMPT modeling describe the mass splitting in d+Au and ^{3}He+Au for $p_T < 1.5$ GeV/c. In the p+Au case, it appears that the calculations over-predict the more modest splitting at the lowest measured $p_T = 0.5$ GeV/c. The results from AMPT without hadronic rescattering have very little mass splitting at low p_T in disagreement with the experimental data, particularly for d+Au and ^{3}He+Au collisions. Above the crossing point, SUPERSONIC, and iEBE-VISHNU predict nearly flat ratios, while AMPT describes the ratio of the v_2 values, but not their individual magnitudes. These differences may be attributed to the different hadronization mechanisms (e.g. - if recombination is included) in the models.

6.2.4 Constituent Quark Scaling

We also showed the v_2/n_q with constituent quarks as a function of transverse kinetic energy per quark $KE_T/n_q = (\sqrt{p_T^2 + m^2} - m)/n_q$, where m is the mass of the hadron and n_q represents the number of constituent quarks in the hadron as in Fig. 6.15. The scaling was previously observed in A+A collisions [79]. In all three small systems, the v_2/n_q for pions and protons as a function of KE_T/n_q follow an approximate quark-number scaling as seen in larger systems. At intermediate p_T $(1.5 - 4$ GeV/$c)$, the enhancement of baryons over
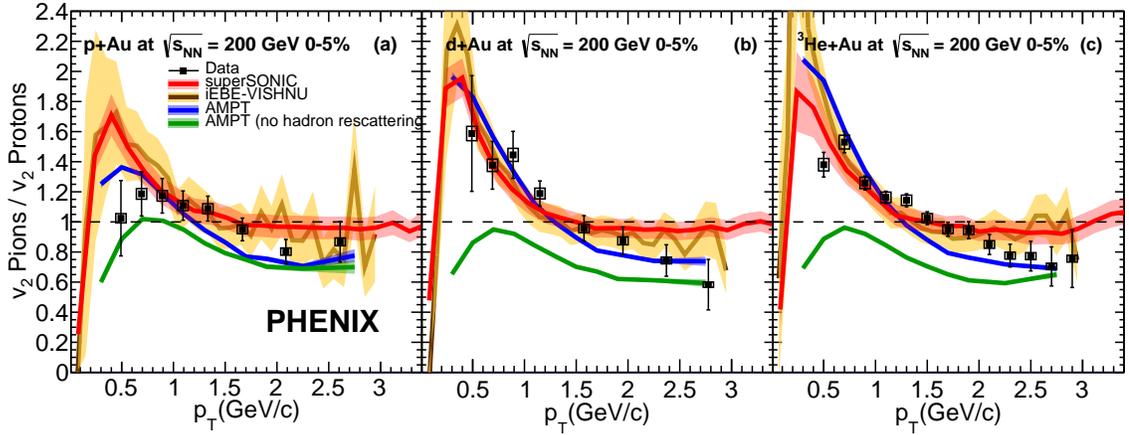
Figure 6.14: Ratio of pion v_2 (p_T) and proton v_2 (p_T), together with various theoretical curves.

mesons and the reversed mass ordering of v_2 have been interpreted in terms of hadroniza-tion via recombination. At even higher p_T, the scaling breaks down as in non-central A+A collisions [80]. We could see that in the ^{3}He+Au and d+Au systems the scaling is better, which means they behave more like the large systems but in p+Au scaling does not follow the general trend so well.
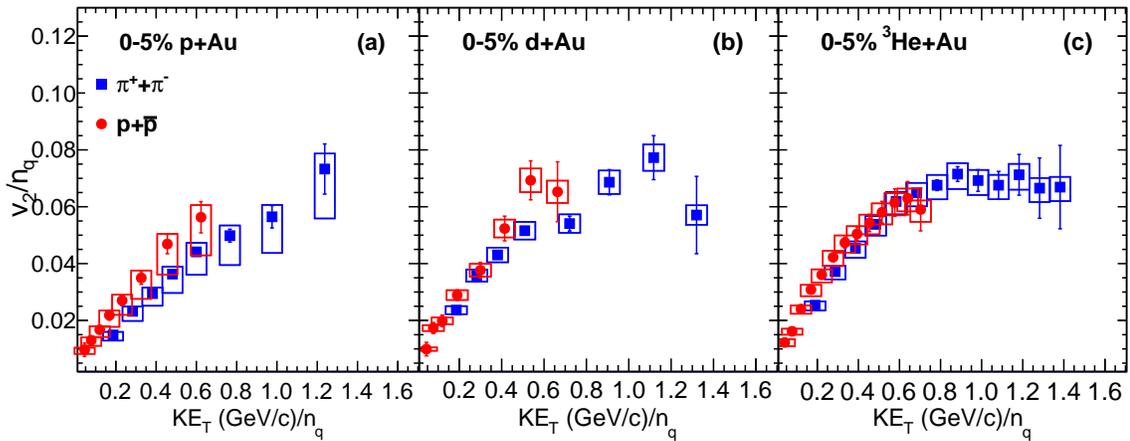
Figure 6.15: Number of constitute quark scaling in three small systems.

6.3   Future Perspective

It is important to notice that additional degrees of freedom for the geometry of p+Au collisions arise from fluctuations of the shape of the proton, as described in Ref. [81]. The contribution of this effect to the measured elliptic flow may be constrained by $p+p$ data, and also possibly studied by varying the target in other p+A systems.

PHENIX has experimental data available for additional analyses in small collision systems such as p+Al(Aluminum) to even smaller-volume $p+p$ collisions. I believe in the future, the measurement of these system will put more constraint on how the initial geometry works.

PHENIX already has a beam energy scan in d+Au collisions down to $\sqrt{s_{NN}} = 20$ GeV. Reducing the collision energy allows us to vary the initial energy density without a substantial change in the initial geometry, and therefore, it enables the study of small systems in an environment where if QGP is formed, it is very short-lived. This will help us understand the boundary conditions for QGP to form and how to distinguish among different models.

Chapter 7

CONCLUSIONS

In this thesis, we present the measurement of second and third order azimuthal anisotropy v_2 and v_3 of charged hadron, as well as v_2 of identified pions, kaons, and protons in p+Au collisions with PHENIX at RHIC. These measurements complete the geometry scan experiments at RHIC together with the d+Au and ^{3}He+Au collisions. The results demonstrate that the initial geometric conditions play a vital role in the development of final-state momentum anisotropies. We also measured v_2 as a function of p_T for identified particles and found mass-dependent v_2 (p_T). The results are compared to various theoretical predictions a and the role of different stages in the evolution of the system is discussed. In the hydrodynamic models the mass dependence arises early in the system evolution during the quark-gluon plasma stage as a result of the common velocity field of the fluid. We found the AMPT can also produce the mass splitting in the v_2 (p_T) via late-stage hadronic rescattering. This process should be similar in other hybrid (e.g. hydro+hadron cascade) models, but seems to be most prominent in the AMPT implementation. Further theoretical studies are needed to clarify the role of the hadronic stage. We found that the experimental results of v_2 (p_T) for different particles exhibit approximate quark-number scaling, as seen in larger systems. The complete set of measurements presented in this thesis is best described by hydrodynamics models that include the formation of a nearly inviscid quark-gluon plasma.

BIBLIOGRAPHY

[1] Wikipedia contributors. Standard model — wikipedia, the free encyclopedia,, 2018. [Online; accessed 15-February-2018].

[2] The Frontiers of Nuclear Science, A Long Range Plan. 2008.

[3] Vardan Khachatryan et al. Evidence for Collective Multiparticle Correlations in p-Pb Collisions. *Phys. Rev. Lett.*, 115(1):012301, 2015.

[4] A. Adare et al. Measurement of long-range angular correlation and quadrupole anisotropy of pions and (anti)protons in central d+Au collisions at $\sqrt{s_{NN}}$=200 GeV. *Phys. Rev. Lett.*, 114:192301, 2015.

[5] A. Adare et al. Measurements of elliptic and triangular flow in high-multiplicity ^{3}He+Au collisions at $\sqrt{s_{NN}} = 200$ GeV. *Phys. Rev. Lett.*, 115(14):142301, 2015.

[6] Peter Christiansen. Identified particle production in p+Pb collisions measured with the ALICE detector. *Nucl. Phys.*, A926:264–269, 2014.

[7] J. L. Nagle, A. Adare, S. Beckman, T. Koblesky, J. O. Koop, D. McGlinchey, P. Romatschke, J. Carlson, J. E. Lynn, and M. McCumber. "Exploiting intrinsic triangular geometry in relativistic 3He+Au collisions to disentangle medium properties". *Phys. Rev. Lett.*, 113:112301, Sep 2014.

[8] Brookhaven National Laboratory Collider-Accelerator Division. @ONLINE-http://www.rhichome.bnl.gov/rhic/runs/, January 2018.

[9] Edward V. Shuryak. Quark-Gluon Plasma and Hadronic Production of Leptons, Photons and Psions. *Phys. Lett.*, 78B:150, 1978. [Yad. Fiz.28,796(1978)].

[10] A. Bazavov et al. Freeze-out Conditions in Heavy Ion Collisions from QCD Thermo-dynamics. *Phys. Rev. Lett.*, 109:192302, 2012.

[11] K. Adcox et al. Formation of dense partonic matter in relativistic nucleus-nucleus collisions at RHIC: Experimental evaluation by the PHENIX collaboration. *Nucl. Phys.*, A757:184–283, 2005.

[12] C. Y. Wong. *Introduction to high-energy heavy ion collisions*. 1995.

[13] John Adams et al. Experimental and theoretical challenges in the search for the quark gluon plasma: The STAR Collaboration's critical assessment of the evidence from RHIC collisions. *Nucl. Phys.*, A757:102–183, 2005.

[14] B. B. Back et al. The PHOBOS perspective on discoveries at RHIC. *Nucl. Phys.*, A757:28–101, 2005.

[15] I. Arsene et al. Quark gluon plasma and color glass condensate at RHIC? The Per-spective from the BRAHMS experiment. *Nucl. Phys.*, A757:1–27, 2005.

[16] S. Afanasiev et al. Systematic Studies of Elliptic Flow Measurements in Au+Au Collisions at $\sqrt{s_{NN}} = 200$ GeV. *Phys. Rev.*, C80:024909, 2009.

[17] B. Abelev et al. (ALICE Collaboration). "Long-range angular correlations on the near and away side in pPb collisions at". *Physics Letters B*, 719(1?):29 – 41, 2013.

[18] G. Aad et al. (ATLAS Collaboration). "Observation of associated near-side and away-side long-range correlations in $\sqrt{s_{NN}}$=5.02 TeV proton-lead collisions with the atlas detector". *Phys. Rev. Lett.*, 110:182302, May 2013.

[19] S. Chatrchyan et al. (CMS Collaboration). "Observation of long-range, near-side angular correlations in pPb collisions at the LHC". *Physics Letters B*, 718(3):795 – 814, 2013.

[20] Vardan Khachatryan et al. Measurement of long-range near-side two-particle angular correlations in pp collisions at $\sqrt{s}$ = 13 TeV. 2015.

[21] Georges Aad et al. Observation of long-range elliptic anisotropies in $\sqrt{s}$ =13 and 2.76 TeV *pp* collisions with the ATLAS detector. 2015.

[22] A. Adare et al. (PHENIX Collaboration). "Quadrupole anisotropy in dihadron azimuthal correlations in central d+Au collisions at $\sqrt{s_{NN}}$=200 GeV". *Phys. Rev. Lett.*, 111:212301, Nov 2013.

[23] B. Alver and G. Roland. Collision geometry fluctuations and triangular flow in heavy-ion collisions. *Phys. Rev.*, C81:054905, 2010. [Erratum: Phys. Rev.C82,039903(2010)].

[24] Vardan Khachatryan et al. Observation of Long-Range Near-Side Angular Correlations in Proton-Proton Collisions at the LHC. *JHEP*, 09:091, 2010.

[25] S. S. Adler et al. Transverse-energy distributions at midrapidity in p+p , d+Au , and Au+Au collisions at $\sqrt{s_{NN}}$ = 62.4?00 GeV and implications for particle-production models. *Phys. Rev.*, C89(4):044905, 2014.

[26] C. Aidala et al. Measurement of long-range angular correlations and azimuthal anisotropies in high-multiplicity p + Au collisions at $\sqrt{s_{NN}}$ = 200 gev. *Phys. Rev. C*, 95:034910, Mar 2017.

[27] Michael L. Miller, Klaus Reygers, Stephen J. Sanders, and Peter Steinberg. Glauber modeling in high energy nuclear collisions. *Ann. Rev. Nucl. Part. Sci.*, 57:205–243, 2007.

[28] Edmond Iancu and Raju Venugopalan. The Color glass condensate and high-energy scattering in QCD. In *In *Hwa, R.C. (ed.) et al.: Quark gluon plasma* 249-3363*. 2003.

[29] Bjoern Schenke, Prithwish Tribedy, and Raju Venugopalan. Fluctuating Glasma initial conditions and flow in heavy ion collisions. *Phys. Rev. Lett.*, 108:252301, 2012.

[30] Amir H. Rezaeian, Marat Siddikov, Merijn Van de Klundert, and Raju Venugopalan. IP-Sat: Impact-Parameter dependent Saturation model revised. *PoS*, DIS2013:060, 2013.

[31] Paul Romatschke and Ulrike Romatschke. Relativistic Fluid Dynamics In and Out of Equilibrium – Ten Years of Progress in Theory and Numerical Simulations of Nuclear Collisions. 2017.

[32] Amaresh Jaiswal and Victor Roy. Relativistic hydrodynamics in heavy-ion collisions: general aspects and recent developments. *Adv. High Energy Phys.*, 2016:9623034, 2016.

[33] Collective phenomena in non-central nuclear collisions. *arxiv*.

[34] Tetsufumi Hirano and Yasushi Nara. Hydrodynamic afterburner for the color glass condensate and the parton energy loss. *Nucl. Phys.*, A743:305–328, 2004.

[35] Paul Romatschke and J. Drew Hogg. Pre-Equilibrium Radial Flow from Central Shock-Wave Collisions in AdS5. *JHEP*, 04:048, 2013.

[36] M. Habich, J. L. Nagle, and P. Romatschke. Particle spectra and HBT radii for simulated central nuclear collisions of C + C, Al + Al, Cu + Cu, Au + Au, and Pb + Pb from $\sqrt{s} = 62.4$ - 2760 GeV. *Eur. Phys. J.*, C75(1):15, 2015.

[37] P. Romatschke. Light-heavy-ion collisions: a window into pre-equilibrium qcd dynamics? *The European Physical Journal C*, 75(7):305, Jul 2015.

[38] S. A. Bass et al. Microscopic models for ultrarelativistic heavy ion collisions. *Prog. Part. Nucl. Phys.*, 41:255–369, 1998. [Prog. Part. Nucl. Phys.41,225(1998)].

[39] M Bleicher, E Zabrodin, C Spieles, S A Bass, C Ernst, S Soff, L Bravina, M Belka-cem, H Weber, H Sticker, and W Greiner. Relativistic hadron-hadron collisions in the ultra-relativistic quantum molecular dynamics model. *Journal of Physics G: Nuclear and Particle Physics*, 25(9):1859, 1999.

[40] C. Shen, J. Paquet, G. S. Denicol, S. Jeon, and C. Gale. Collectivity and electromagnetic radiation in small systems. *Phys. Rev. C*, 95(1):014906, 2017.

[41] Xin-Nian Wang and Miklos Gyulassy. HIJING: A Monte Carlo model for multiple jet production in p p, p A and A A collisions. *Phys. Rev.*, D44:3501–3516, 1991.

[42] Zi-Wei Lin, Che Ming Ko, Bao-An Li, Bin Zhang, and Subrata Pal. A Multi-phase transport model for relativistic heavy ion collisions. *Phys. Rev.*, C72:064901, 2005.

[43] Bao-An Li and Che Ming Ko. Formation of superdense hadronic matter in high energy heavy-ion collisions. *Phys. Rev. C*, 52:2037–2063, Oct 1995.

[44] BAO-AN LI, A. T. SUSTICH, BIN ZHANG, and C. M. KO. Studies of superdense hadronic matter in a relativistic transport model. *International Journal of Modern Physics E*, 10(04n05):267–352, 2001.

[45] Brookhaven National Laboratory Collider-Accelerator Division. @ONLINE-https://www.bnl.gov/cad/accelerator/docs/pdf/rhicconfmanual.pdf, January 2018.

[46] K. Adcox et al. PHENIX detector overview. *Nucl. Instrum. Meth.*, A499:469–479, 2003.

[47] R. M. Yamamoto, J. M. Bowers, A. R. Harvey, R. M. Holmes, G. F. James, M. A. Libkind, R. W. Martin, L. E. Mullins, J. N. Thomas, W. J. Wong, S. H. Aronson, S. A. Kahn, P. J. Kroon, T. K. Shea, R. D. Schlueter, and W. E. Sondheim. The phenix detector magnet subsystem. *IEEE Transactions on Magnetics*, 32(4):2140–2143, Jul 1996.

[48] K. Adcox et al. Phenix central arm tracking detectors. *Nuclear Instruments and Methods in Physics Research Section A: Accelerators, Spectrometers, Detectors and Associated Equipment*, 499(2):489 – 507, 2003. The Relativistic Heavy Ion Collider Project: RHIC and its Detectors.

[49] H. Masui for the PHENIX TOF group. url: "https://www.phenix.bnl.gov/www/intro/detectors/focus/focus_tof.pdf".

[50] B. Love. Masters thesis, vanderbilt university (2009), url http://www.phenix.bnl.gov/www/talk/archive/theses/2009/love_brian-thesis_brianlove.pdf.

[51] A. Adare et al. Spectra and ratios of identified particles in Au+Au and d+Au collisions at $\sqrt{s_{NN}} = 200$ GeV. *Phys. Rev.*, C88(2):024906, 2013.

[52] C. Aidala et al. The phenix forward silicon vertex detector. *Nuclear Instruments and Methods in Physics Research Section A: Accelerators, Spectrometers, Detectors and Associated Equipment*, 755(Supplement C):44 – 61, 2014.

[53] Ulrich Heinz and Raimond Snellings. Collective flow and viscosity in relativistic heavy-ion collisions. *Annual Review of Nuclear and Particle Science*, 63(1):123–151, 2013.

[54] A. Adare et al. Centrality categorization for $R_{p(d)+Au}$ in high-energy collisions. *Phys. Rev.*, C90(3):034902, 2014.

[55] A. Trivedi et al. PISA: The PHENIX experiment simulation package. In *Proceedings, 9th International Conference on Computing in High-Energy Physics (CHEP 1997): Berlin, Germany, April 7-11, 1997*, 1997.

[56] A. Adare et al. Single electron yields from semileptonic charm and bottom hadron decays in Au+Au collisions at $\sqrt{s_{NN}} = 200$ GeV. *Phys. Rev. C*, 93(3):034904, 2016.

[57] A. M. Poskanzer and S. A. Voloshin. Methods for analyzing anisotropic flow in relativistic nuclear collisions. *Phys. Rev. C*, 58:1671–1678, 1998.

[58] Ulrich W. Heinz and Barbara V. Jacak. Two particle correlations in relativistic heavy ion collisions. *Ann. Rev. Nucl. Part. Sci.*, 49:529–579, 1999.

[59] Wilke van der Schee, Paul Romatschke, and Scott Pratt. Fully Dynamical Simulation of Central Nuclear Collisions. *Phys. Rev. Lett.*, 111(22):222302, 2013.

[60] Paul M. Chesler and Laurence G. Yaffe. Holography and off-center collisions of localized shock waves. *JHEP*, 10:070, 2015.

[61] Charles Gale, Sangyong Jeon, Bj?rn Schenke, Prithwish Tribedy, and Raju Venugopalan. Event-by-event anisotropic flow in heavy-ion collisions from combined Yang-Mills and viscous fluid dynamics. *Phys. Rev. Lett.*, 110(1):012302, 2013.

[62] A. Adare et al. Measurements of directed, elliptic, and triangular flow in Cu+Au collisions at $\sqrt{s_{NN}} = 200$ GeV. *Phys. Rev. C*, 94(5):054910, 2016.

[63] J. D. Orjuela Koop, A. Adare, D. McGlinchey, and J. L. Nagle. Azimuthal anisotropy relative to the participant plane from a multiphase transport model in central p + Au , d + Au , and ^{3}He + Au collisions at $\sqrt{s_{NN}} = 200$ GeV. *Phys. Rev.*, C92(5):054903, 2015.

[64] Guo-Liang Ma and Zi-Wei Lin. Predictions for $\sqrt{s_{NN}} = 5.02$ TeV Pb+Pb Collisions from a Multi-Phase Transport Model. *Phys. Rev.*, C93(5):054911, 2016.

[65] Guo-Liang Ma and Adam Bzdak. "Long-range azimuthal correlations in proton?proton and proton?nucleus collisions from the incoherent scattering of partons". *Physics Letters B*, 739(0):209 – 213, 2014.

[66] S. Eremin and S. Voloshin. Nucleon participants or quark participants? *Phys. Rev.*, C67:064905, 2003.

[67] A. Adare et al. Transverse energy production and charged-particle multiplicity at midrapidity in various systems from $\sqrt{s_{NN}} = 7.7$ to 200 GeV. *Phys. Rev.*, C93(2):024901, 2016.

[68] Kevin Welsh, Jordan Singer, and Ulrich W. Heinz. Initial state fluctuations in collisions between light and heavy ions. *Phys. Rev.*, C94(2):024919, 2016.

[69] Ulrich Heinz and Raimond Snellings. Collective flow and viscosity in relativistic heavy-ion collisions. *Ann. Rev. Nucl. Part. Sci.*, 63:123–151, 2013.

[70] S. S. Adler et al. Elliptic flow of identified hadrons in Au+Au collisions at s(NN)**(1/2) = 200-GeV. *Phys. Rev. Lett.*, 91:182301, 2003.

[71] B. B. Abelev et al. Long-range angular correlations of π, K and p in p-Pb collisions at $\sqrt{s_{\text{NN}}} = 5.02$ TeV. *Phys. Lett. B*, 726:164–177, 2013.

[72] V. Khachatryan et al. Long-range two-particle correlations of strange hadrons with charged particles in pPb and PbPb collisions at LHC energies. *Phys. Lett. B*, 742:200–224, 2015.

[73] Zi-Wei Lin, Che Ming Ko, Bao-An Li, Bin Zhang, and Subrata Pal. "Multiphase transport model for relativistic heavy ion collisions". *Phys. Rev. C*, 72(6):064901, December 2005.

[74] H. Li, L. He, Z. Lin, D. Molnar, F. Wang, and W. Xie. Origin of the mass splitting of elliptic anisotropy in a multiphase transport model. *Phys. Rev. C*, 93(5):051901, 2016.

[75] R. J. Fries, V. Greco, and P. Sorensen. Coalescence Models For Hadron Formation From Quark Gluon Plasma. *Ann. Rev. Nucl. Part. Sci.*, 58:177–205, 2008.

[76] S. S. Adler et al. Scaling properties of proton and anti-proton production in $\sqrt{s_{NN}} = 200$ GeV Au+Au collisions. *Phys. Rev. Lett.*, 91:172301, 2003.

[77] S. S. Adler et al. Identified charged particle spectra and yields in Au+Au collisions at $\sqrt{s_{NN}} = 200$ GeV. *Phys. Rev. C*, 69:034909, 2004.

[78] M. Bleicher et al. Relativistic hadron hadron collisions in the ultrarelativistic quantum molecular dynamics model. *J. Phys. G*, 25:1859–1896, 1999.

[79] A. Adare et al. Scaling properties of azimuthal anisotropy in Au+Au and Cu+Cu collisions at s(NN) = 200-GeV. *Phys. Rev. Lett.*, 98:162301, 2007.

[80] A. Adare et al. Deviation from quark-number scaling of the anisotropy parameter v_2 of pions, kaons, and protons in Au+Au collisions at $\sqrt{s_{NN}} = 200$ GeV. *Phys. Rev. C*, 85:064914, 2012.

[81] Soeren Schlichting and Bjoern Schenke. The shape of the proton at high energies. *Phys. Lett.*, B739:313–319, 2014.